Remotely Sensing Aqueous Alteration on Mars: Innovative Statistical and Analytical Methods for Large Spectral Datasets

Thesis by

Nancy H. Thomas

In Partial Fulfillment of the Requirements for

the degree of

Doctor of Philosophy

CALIFORNIA INSTITUTE OF TECHNOLOGY

Pasadena, California

2019

(Defended May 28, 2019)

Nancy H. Thomas
ORCID: 0000-0003-1989-4860

In Loving Memory

Nancy Ann Meagher Hicks and James LeRoy Hicks

ACKNOWLEDGEMENTS

First, I would like to thank my advisor, Bethany Ehlmann. This thesis would not have been possible without her, and I am very thankful for all of her time and help. I appreciate how she has always challenged me to see the bigger picture. I have grown as a scientist thanks to her encouragement. I would like to thank my academic advisor Heather Knutson for being such a supportive mentor. In our conversations, Heather has provided inspiration and helpful perspective. I would also like to thank my committee members: George Rossman, John Grotzinger, and Woody Fischer. I have really appreciated all the Caltech faculty I've had the pleasure of meeting. My journey at Caltech would not have been possible without my UW mentors. I am so grateful for the endless support of my undergraduate advisor, Josh Bandfield. My solid research foundation came from hours and hours of his one-on-one teaching. I am so happy Elena Amador followed me to Caltech. She has always believed in me and her encouragement has helped me to succeed.

The work presented in this thesis would not have been possible without the amazing MSL Science Team. I have really enjoyed interacting with the team at meetings and learning from them during operations. I am grateful for the input of the ChemCam team, particularly Roger Wiens, a great advocate of my work. I would like to thank my other collaborators, particularly Abby Fraeman and William Rapin. The entire Ehlmann lab group provided so many valuable suggestions that improved my work.

I am grateful for the non-scientific opportunities I have had at Caltech. I would like to thank the Caltech Alumni Association, Caltech Y, Grad Office, and Graduate Student Council. Don McCarthy initially inspired me to study astronomy – I am so thankful for his continued encouragement and the opportunity he has provided me to teach at Astronomy Camp. Additionally, I would like to thank the amazing support staff who have been so helpful – particularly Ulrika Terrones, Margaret Carlos, Irma Black, Loreta Young, Scott Dungan, Julie Lee, and Cruz Martinez.

When I arrived at Caltech, I was immediately welcomed into the planetary science graduate student community. Grad school was fun, thanks to friends lighting up my days: thanks to

Peter Gao, Mike Wong, Henry Ngo, Laura Ngo, Danielle Piskorz, Lulu Pan, Joe O'Rourke, Pushkar Kopparla, Patrick Fischer, Erin Fischer, Elizabeth Bailey, Siteng Fan, Cam Buzard, Nicole Wallack, Cecilia Sanders, Eva Scheller, Shreyas Vissapragada, Aida Behmard, Yayaati Chachan, and many others!

I would not have made it through grad school without the constant support of my close friends and family. I would like to thank Dana Anderson for being the other half of my brain and my second set of eyes reading over so many emails, papers, and applications. Dana's friendship and encouragement has always pushed me in the right direction. I would like to thank Nathan Stein for seeing so much in me and for making my days so happy, fun, and bright. I would also like to thank my friends who have stayed so close and provided so much love from afar, particularly Lauren Wolfs and Margaret Landis. Finally, most of all, I would like to thank my parents Ann Hicks-Thomas and Arthur Thomas. They have helped me in so many big and little ways – from many visits to sending food – all of their love support has meant so much to me.

ABSTRACT

Liquid water once flowed on Mars and altered the crust. Aqueous minerals and salts record a rich history of aqueous processes and environmental changes. In this dissertation, I developed and applied innovative analytical and statistical methods to large spectral datasets to better characterize aqueous alteration on Mars. The Mars Science Laboratory (MSL) Curiosity rover is investigating the sedimentary sequence at Gale crater recording a potentially global transition from clay-enriched to sulfate-enriched rocks. Volatile elements like H and Cl are important for investigating aqueous processes, but are difficult to quantify in the large ChemCam laser-induced breakdown spectroscopy (LIBS) dataset. In the first part of this dissertation, I measured aqueously altered samples with LIBS in the laboratory under Mars-relevant conditions to develop analytical methods for application to ChemCam. The Murray formation, the lowest exposed strata of the sedimentary sequence, contains 2.6 ± 2.1 wt. % H_2O. Carriers of H enrichment including clays, opal, Mg-sulfates, Ca-sulfates, hydrous Mn-oxides, akageneite, and jarosite are identified. Variability in the H content of the Murray formation records multiple aqueous alteration events as well as potential increases in salinity in the Gale crater lake. In the fourth chapter, I measured chlorine in Gale crater using multiple MSL instruments. Cl-enrichments correlated with increased Na_2O are detected in the bedrock, in nodular textures, and at vein margins, indicating halite. The scattered, isolated occurrences of chlorides are consistent with late groundwater reworking and remobilization. Halite is concentrated in particular members of the Murray formation; the chlorides may have been emplaced as primary deposits in these members, consistent with varying salinity in the past lakewaters. In the second part of this dissertation, I adapted and applied semi-automated statistical methods called factor analysis and target transformation to the Compact Reconnaissance Imaging Spectrometer for Mars (CRISM) dataset to systematically search for hematite in stratified, candidate sedimentary outcrops. Few outcrops containing hematite are found and no obvious analogs to terrestrial iron formations are identified. Future studies will search for hematite in other geologic settings as well as other Fe-bearing phases such as Fe-phyllosilicates and Fe-sulfates to better characterize aqueous processes on Mars.

PUBLISHED CONTENT AND CONTRIBUTIONS

Thomas, N. H., et al. (2018). Characterization of hydrogen in basaltic materials with laser-induced breakdown spectroscopy (LIBS) for application to MSL ChemCam data. *Journal of Geophysical Research: Planets, 123*, 1996–2021. https://doi.org/ 10.1029/2017JE005467

N. H. T. participated in the conception of the project, collected laboratory measurements, developed spectral processing algorithms, prepared the figures, and participated in the writing of the manuscript.

Adapted for the contents of Chapter 2.

Thomas, N. H., et al. (2019). Mars Science Laboratory Observations of Chloride Salts in Gale Crater, Mars. *Geophysical Research Letters.* Under review.

N. H. T. participated in the conception of the project, analyzed all the ChemCam spectral data, prepared the figures, and participated in the writing of the manuscript.

Adapted for the contents of Chapter 4.

TABLE OF CONTENTS

LIST OF ILLUSTRATIONS

Number *Page*

LIST OF ILLUSTRATIONS CONT.

Number *Page*

LIST OF TABLES

Number *Page*

LIST OF ACRONYMS

APXS. Alpha Particle X-ray Spectrometer

CRISM. Compact Reconnaissance Imaging Spectrometer for Mars

CTX. Context Camera

DAN. Dynamic Albedo of Neutrons

EGA. Evolved Gas Analysis

FWHM. Full Width at Half Maximum

LANL. Los Alamos National Laboratory

LIBS. Laser-Induced Breakdown Spectroscopy

LOD. Limit of Detection

MAHLI. Mars Hand Lens Imager

MOLA. Mars Orbiter Laser Altimeter

MSL. Mars Science Laboratory

OMEGA. Observatoire pour la Minéralogie, l'Eau, les Glaces et l'Activité

PCA. Principal Components Analysis

RMI. Remote Micro Imager

RMSECV. Root Mean Squared Error Cross Validation

SAD. Spectral Angle Distance

SAM. Sample Analysis at Mars

TES. Thermal Emission Spectrometer

TGA. Thermogravimetric analysis

THEMIS. Thermal Emission Imaging System

TIR. Thermal Infrared

UV. Ultraviolet

VIS. Visible

WEH. Water Equivalent Hydrogen

VNIR. Visible and Near-Infrared

XRD. X-ray Diffraction

XRF. X-ray Fluorescence

Chapter 1

INTRODUCTION

1. Martian aqueous history

Liquid water once flowed on Mars. The discovery of "canals" on Mars by Percival Lowell (Lowell, 1906) first drew comparisons to our own watery world. While the "canals" were later refuted, Mariner 9 imagery in the 1970s raised evidence for water-carved surfaces. Although liquid water is unstable at the surface at present due to a thin (6 mbar) CO_2 atmosphere, morphological features suggest surface waters may have been stable and pervasive earlier in Mars' history. Outflow channels (e.g., Baker, 1974; Masursky et al., 1977), valley networks (e.g., Carr, 1995; Hynek et al., 2010), open and closed basin lakes (e.g., Fassett and Head, 2008; Goudge et al., 2012), and widespread sedimentary deposits (e.g., Malin and Edgett, 2000; Squyres and Knoll, 2005) have been discovered, providing geomorphic evidence of past aqueous activity primarily during the late Noachian to early Hesperian in age with the exception of the Hesperian outflow channels (Fassett and Head, 2011).

Thermal infrared (TIR) and visible near-infrared (VNIR) orbital spectroscopic studies have informed our understanding of the composition of Mars and provided complementary evidence for pervasive waters. The martian crust is primarily basaltic (e.g., Christensen et al., 2000) and igneous minerals such as olivine and pyroxenes have been mapped globally (e.g., Koeppen and Hamilton, 2008; Mustard et al., 2005). Exposures of the ancient Noachian crust contain clay minerals such as Fe/Mg phyllosilicates (e.g., Poulet et al., 2005; Mustard et al., 2008), indicating pervasive aqueous alteration processes at neutral to alkaline pH. Chloride, carbonate, and sulfate salts have been mapped globally, and detailed, localized studies have provided evidence for late Noachian – early Hesperian paleolakes (e.g., Murchie et al., 2009) and playas (e.g., Wray et al., 2010). Assemblages of iron and aluminum sulfates mostly in Hesperian terrains potentially suggest at least a local transition to more acidic

waters (e.g., Bibring et al., 2007). Amazonian terrains show little evidence for aqueous alteration (Ehlmann and Edwards, 2014), reflecting a transition to a drier climate on Mars.

2. A case study: Gale crater

Orbital observations of Gale crater identified a sequence of nontronite, hematite, and sulfate-bearing sedimentary rocks in the central 5-km mound called Mount Sharp (Milliken et al., 2010; Fraeman et al., 2013). Gale formed in the Hesperian (Thomson et al., 2011) and provides an excellent field site to study the globally observed transition from clay-rich to sulfate-rich sediments in stratigraphy (Grotzinger et al., 2012). The Mars Science Laboratory (MSL) *Curiosity* rover landed in Gale crater in 2012 and has mostly examined rocks formed in a fluvio-lacustrine environment, including both fluvial/alluvial deposits and laminated mudstones from subaqueous deposition (Grotzinger et al., 2015; Grotzinger et al., 2015). The rover's toolkit includes CheMin, a powder X-ray diffraction (XRD) instrument, and SAM (Sample Analysis at Mars), a gas chromatograph and mass spectrometer, for measuring drilled rock samples (Grotzinger et al., 2012). So far, before even reaching the sulfate unit observed from orbit, CheMin and SAM have measured both oxidized (sulfate, nitrate, oxychlorine) and reduced (sulfides, organics) phases along with mineralogies suggesting acidic (e.g., Fe-sulfate) and alkaline (e.g., phyllosilicates) conditions (e.g., Bish et al., 2013, Blake et al., 2013; Ming et al., 2014; Rampe et al., 2017). These observations imply the occurrence of multiple aqueous events with varying chemistry over time.

3. Identifying aqueous alteration using large spectral datasets

The sedimentary record preserved at Gale crater provides an opportunity to examine variations in the chemistry of martian waters, and thereby past environments. In order to use the sedimentary rocks at Gale to inform our understanding of the past climate, we need to be able to differentiate between primary depositional and later post-depositional phases. In particular, salts like chlorides and sulfates can provide key constraints on fluid chemistry, but can be the product of primary processes (e.g., precipitation from saline fluids at a lake margin) or diagenesis (e.g., groundwater upwelling, aquifer processes). CheMin and SAM

can aid our understanding by measuring mineralogy and chemistry, but are limited to a relatively small number of drill targets that are somewhat sporadically sampled due to operational challenges. Geochemical changes can happen over spatial scales of micrometers: recognizing and carefully recording these differences is important for understanding the prevalence of aqueous alteration at Gale.

ChemCam is a remote sensing survey instrument onboard *Curiosity* which provides a large (>19,000 measurements to date) spectral dataset for measuring elemental chemistry. Laser-induced breakdown spectroscopy (LIBS) provides a new fine-scale (350-550 micron diameter) perspective, removes dust contribution, and allows remote geochemical analysis. This is the first use of LIBS for a planetary mission and analytical methods must be developed to fully utilize this dataset, particularly to quantify minor elements. Volatile elements like H, C, Cl, and S have few, weak but measurable LIBS emission lines and require laboratory characterization under Mars-relevant conditions because LIBS is very sensitive to environmental conditions. In this thesis, I developed analytical tools for measuring volatile elements in the large ChemCam dataset. I investigated the capabilities of ChemCam for probing signatures of aqueous alteration at Gale. How capable is ChemCam at accurately measuring volatile element abundance? Is ChemCam sensitive to variations in aqueous alteration? Furthermore, by detecting H and key elements found in salts (Cl, C, S), we can use ChemCam to measure what primary and secondary aqueous minerals are present in Gale crater. What can we learn about the chemistry of past water(s)? What paleoenvironments were present in Gale?

The Compact Reconnaissance Imaging Spectrometer for Mars (CRISM) instrument provides another large (>35,000 full resolution images) spectral dataset valuable for identifying aqueous alteration, but at a global scale. Phyllosilicates, sulfates, and other minerals have been mapped using VNIR spectroscopy. The (relatively) high resolution of CRISM (~18 m/pixel) enables characterization of the geologic context as well. The infrared wavelength dataset of CRISM has been studied extensively, but the visible wavelength dataset is underutilized in comparison and may provide new information on Fe mineralogy. The

challenge is systematically searching for specific mineral endmembers in the large and often noisy (due to imperfect calibration and atmospheric correction) dataset. The global-scale acidification that may have occurred during the Hesperian is poorly understood but one proposed mechanism is increasing acidity associated with the formation of iron oxides (Bibring et al., 2006; Hurowitz et al., 2010). The martian crust is basaltic and Fe-rich; if past waters were capable of dissolving and transporting iron, what phases were favored? Did iron oxides form in sedimentary deposits analogous to terrestrial iron formations? Or were other Fe-bearing phases such as Fe-phyllosilicates or Fe-sulfates favored? Characterizing iron-bearing sedimentary deposits on Mars may provide new insight into environmental conditions preserved in the martian rock record and potentially help understand proposed global-scale acidification.

4. Thesis contents

In this thesis, I addressed the challenges put forth above by developing and applying new statistical and analytical methods for interpreting large spectral datasets. In the first part, Chapters 2-4, I developed new analytical methods for the MSL ChemCam instrument and applied them to detect aqueous alteration and salts. In the second part, Chapter 5, I adapted and applied a statistical method called factor analysis and target transformation to the CRISM visible data to search for hematite in candidate sedimentary, stratified outcrops.

Here, I summarize the key points of each chapter:

In Chapter 2, I analyzed laboratory LIBS measurements of powderized pellets of mixtures of basalts and hydrated minerals as well as natural altered samples under martian (6 mbar CO_2) conditions. I also obtained a complementary thermogravimetric analysis dataset for independently measuring H content. I evaluated multiple calibration and normalization methods to determine H content form the hydrogen-alpha LIBS emission line. O 778 and C 248 nm normalizations have the lowest scatter for the lab set, best correct for varying distance to target, and successfully determine H for martian rocks. The observed non-linear

calibrations for high H samples and physical matrix effects which change the H peak for natural vs. pelletized samples warrant further study.

In Chapter 3, I applied the analytical methods developed for H in Chapter 2 to the martian ChemCam dataset. The Murray formation contains on average 2.6 ± 2.1 wt. % H_2O, consistent with measurements using the SAM and DAN instruments. The LIBS measured H content varies in specific members of the Murray, Hartmann's Valley, Pettegrove Point, and Jura, and H shows a dependence on grain size. The presence of high-H phases including hydrated silica, hydrated Mg-sulfates, hydrous Mn-oxides, and akageneite are inferred, and provide further evidence for extensive water-rock interaction in the Murray formation as well as saline fluids, either primary or diagenetic.

In Chapter 4, I applied analytical LIBS methods to systematically measure Cl in the ChemCam dataset. ChemCam, APXS, CheMin, and SAM data are used to make the case for scattered, isolated deposits of chloride salts in the Murray formation. The isolated Cl enrichments occur in bedrock, in nodular textures, and at calcium sulfate vein margins, and are correlated with enriched Na, indicating halite. The scattered, isolated occurrences of chlorides are consistent with late groundwater reworking and remobilization of original deposits. Because chlorides are found in particular members of the Murray formation, the chlorides may have been emplaced as small-scale primary deposits in these members, consistent with varying salinity in the waters in which the Murray formation was deposited.

In Chapter 5, I adapted and applied a semi-automated statistical technique called factor analysis and target transformation to the CRISM visible data to search for hematite in candidate sedimentary, stratified outcrops with the goal of testing the hypothesis that iron formation analogs formed on early Mars. The survey methods work well, but hematite is only detected in 3% of the images surveyed, suggesting hematite is rare in this geologic setting on Mars. We confirm previous detections of hematite in Mawrth Vallis, Iani Chaos, and Meridiani Planum and first identify hematite in Nili Fossae. The deposits discovered do not seem analogous to terrestrial iron formations. Other Fe-bearing phases may have been

favored, and future studies using our methods can search for other Fe-phyllosilicates and Fe-sulfates in addition to searching for hematite in other geologic settings.

Finally, in Chapter 6, I summarized my results, discussed their implications, and commented on some outstanding questions and challenges raised by this thesis.

References

Baker, V. R., & Milton, D. J. (1974). Erosion by catastrophic floods on Mars and Earth. *Icarus*, *23*(1), 27–41. https://doi.org/10.1016/0019-1035(74)90101-8

Bibring, J.-P., Arvidson, R. E., Gendrin, A., Gondet, B., Langevin, Y., Le Mouelic, S., … Sotin, C. (2007). Coupled Ferric Oxides and Sulfates on the Martian Surface. *Science*, *317*(5842), 1206–1210. https://doi.org/10.1126/science.1144174

Bibring, J.-P., Langevin, Y., Mustard, J. F., Poulet, F., Arvidson, R., Gendrin, A., … Neukum, G. (2006). Global Mineralogical and Aqueous Mars History Derived from OMEGA/Mars Express Data. *Science*, *312*(5772), 400–404. https://doi.org/10.1126/science.1122659

Bish, D. L., Blake, D. F., Vaniman, D. T., Chipera, S. J., Morris, R. V., Ming, D. W., … Mier, M.-P. Z. (2013). X-ray Diffraction Results from Mars Science Laboratory: Mineralogy of Rocknest at Gale Crater. *Science*, *341*(6153), 1238932–1238932. https://doi.org/10.1126/science.1238932

Blake, D. F., Morris, R. V, Kocurek, G., Morrison, S. M., Downs, R. T., Bish, D., … Zorzano Mier, M.-P. (2013). Curiosity at Gale Crater, Mars: Characterization and Analysis of the Rocknest Sand Shadow. *Science*, *341*(6153), 1239505–1239505. https://doi.org/10.1126/science.1239505

Carr, M. H. (1995). The Martian drainage system and the origin of valley networks and fretted channels. *Journal of Geophysical Research*, *100*(E4), 7479. https://doi.org/10.1029/95JE00260

Christensen, P. R., Bandfield, J. L., Clark, R. N., Edgett, K. S., Hamilton, V. E., Hoefen, T., … Smith, M. D. (2000). Detection of crystalline hematite mineralization on Mars by the Thermal Emission Spectrometer: Evidence for near-surface water. *Journal of Geophysical Research: Planets*, *105*(E4), 9623–9642. https://doi.org/10.1029/1999JE001093

Ehlmann, B. L., & Edwards, C. S. (2014). Mineralogy of the Martian Surface. *Annual Review of Earth and Planetary Sciences*, *42*(1), 291–315. https://doi.org/10.1146/annurev-earth-060313-055024

Fassett, C. I., & Head, J. W. (2008). Valley network-fed, open-basin lakes on Mars: Distribution and implications for Noachian surface and subsurface hydrology. *Icarus*, *198*(1), 37–56. https://doi.org/10.1016/j.icarus.2008.06.016

Fassett, C. I., & Head, J. W. (2011). Sequence and timing of conditions on early Mars. *Icarus*, *211*(2), 1204–1214. https://doi.org/10.1016/j.icarus.2010.11.014

Fraeman, A. A., Arvidson, R. E., Catalano, J. G., Grotzinger, J. P., Morris, R. V., Murchie, S. L., … Viviano, C. E. (2013). A hematite-bearing layer in gale crater, mars: Mapping and implications for past aqueous conditions. *Geology*, *41*(10), 1103–1106. https://doi.org/10.1130/G34613.1

Goudge, T. A., Mustard, J. F., Head, J. W., & Fassett, C. I. (2012). Constraints on the history of open-basin lakes on Mars from the composition and timing of volcanic resurfacing. *Journal of Geophysical Research E: Planets*, *117*(12), 1–24. https://doi.org/10.1029/2012JE004115

Grotzinger, J. P., Crisp, J., Vasavada, A. R., Anderson, R. C., Baker, C. J., … Meyer, M. (2012). Mars Science Laboratory Mission and Science Investigation. *Space Sci Rev* (2012) 170: 5. https://doi.org/10.1007/s11214-012-9892-2

Grotzinger, J. P., Sumner, D. Y., Kah, L. C., Stack, K., Gupta, S., … Yingst, A. (2014). A Habitable Fluvio-Lacustrine Environment at Yellowknife Bay, Gale Crater, Mars. *Science, 343*(6169). https://doi.org/10.1126/science.1242777

Grotzinger, J. P., Gupta, S., Malin, M. C., Rubin, D. M., Schieber, J., Siebach, K., … Mcbride, M. J. (2015). Deposition, exhumation, and paleoclimate of an ancient lake deposit, Gale crater, Mars. *Science, 350*(6257). https://doi.org/10.1126/science.aac7575

Hurowitz, J. A., Fischer, W. W., Tosca, N. J., & Milliken, R. E. (2010). Origin of acidic surface waters and the evolution of atmospheric chemistry on early Mars. *Nature Geoscience*, *3*(5), 323–326. https://doi.org/10.1038/ngeo831

Hynek, B. M., Beach, M., & Hoke, M. R. T. (2010). Updated global map of Martian valley networks and implications for climate and hydrologic processes. *Journal of Geophysical Research: Planets*, *115*(E9), 1–14. https://doi.org/10.1029/2009JE003548

Koeppen, W. C., & Hamilton, V. E. (2008). Global distribution, composition, and abundance of olivine on the surface of Mars from thermal infrared data. *Journal of Geophysical Research*, *113*(E5), E05001. https://doi.org/10.1029/2007JE002984

Lowell, P. (1906), Mars and its Canals, The Macmillan Company; London: Macmillan & co., ltd

Malin, M. C. (2000). Sedimentary Rocks of Early Mars. *Science*, *290*(5498), 1927–1937. https://doi.org/10.1126/science.290.5498.1927

Masursky, H., Boyce, J. M., Dial, A. L., Schaber, G. G., & Strobell, M. E. (1977). Classification and time of formation of Martian channels based on Viking data. *Journal of Geophysical Research, 82*(28), 4016–4038. https://doi.org/10.1029/JS082i028p04016

Milliken, R. E., Grotzinger, J. P., & Thomson, B. J. (2010). Paleoclimate of Mars as captured by the stratigraphic record in Gale Crater. *Geophysical Research Letters, 37*(4), 1–6. https://doi.org/10.1029/2009GL041870

Ming, D. W., Archer, P. D., Glavin, D. P., Eigenbrode, J. L., Franz, H. B., Sutter, B., … Moores, J. E. (2014). Volatile and Organic Compositions of Sedimentary Rocks in Yellowknife Bay, Gale Crater, Mars. *Science*, *343*(6169), 1245267–1245267. https://doi.org/10.1126/science.1245267

Ming, D. W., Archer, P. D., Glavin, D. P., Eigenbrode, J. L., Franz, H. B., Sutter, B., … Moores, J. E. (2014). Volatile and Organic Compositions of Sedimentary Rocks in Yellowknife Bay, Gale Crater, Mars. *Science*, *343*(6169), 1245267–1245267. https://doi.org/10.1126/science.1245267

Murchie, S., Roach, L., Seelos, F., Milliken, R., Mustard, J., Arvidson, R., … Morris, R. (2009). Evidence for the origin of layered deposits in Candor Chasma, Mars, from mineral composition and hydrologic modeling. *Journal of Geophysical Research, 114*(E12). https://doi.org/10.1029/2009JE003343.

Mustard, J. F. (2005). Olivine and Pyroxene Diversity in the Crust of Mars. *Science, 307*(5715), 1594–1597. https://doi.org/10.1126/science.1109098

Mustard, J. F., Murchie, S. L., Pelkey, S. M., Ehlmann, B. L., Milliken, R. E., Grant, J. A., … Wolff, M. (2008). Hydrated silicate minerals on Mars observed by the Mars Reconnaissance Orbiter CRISM instrument. *Nature*, *454*(7202), 305–309. https://doi.org/10.1038/nature07097

Poulet, F., Bibring, J.-P., Mustard, J. F., Gendrin, A., Mangold, N., Langevin, Y., … Gomez, C. (2005). Phyllosilicates on Mars and implications for early martian climate. *Nature*, *438*(7068), 623–627. https://doi.org/10.1038/nature04274

Rampe, E. B., Ming, D. W., Blake, D. F., Bristow, T. F., Chipera, S. J., Grotzinger, J. P., … Thompson, L. M. (2017). Mineralogy of an ancient lacustrine mudstone succession from the Murray formation, Gale crater, Mars. *Earth and Planetary Science Letters*, *471*, 172–185. https://doi.org/10.1016/j.epsl.2017.04.021

Squyres, S., and Knoll, A. H. (2005). Sedimentary rocks at Meridiani Planum: Origin, diagenesis, and implications for life on Mars. Earth and Planetary Science Letters, 240, 1-10. https://doi.org/10.1016/j.epsl.2005.09.038

Thomson, B. J., Bridges, N. T., Milliken, R., Baldridge, A., Hook, S. J., Crowley, J. K., … Weitz, C. M. (2011). Constraints on the origin and evolution of the layered mound in Gale Crater, Mars using Mars Reconnaissance Orbiter data. *Icarus*, *214*(2), 413–432. https://doi.org/10.1016/j.icarus.2011.05.002

Wray, J., Squyres, S. W., Roach, L. H., Bishop, J. L., Mustard, J. F., and Noe Dobrea, E. Z. (2010). Identification of the Ca-sulfate bassanite in Mawrth Vallis, Mars. Icarus, 209(2), 416-421. https://doi.org/10.1016/j.icarus.2010.06.001

Chapter 2

CHARACTERIZATION OF HYDROGEN IN BASALTIC MATERIALS WITH LASER-INDUCED BREAKDOWN SPECTROSCOPY (LIBS) FOR APPLICATION TO MSL CHEMCAM DATA

N. H. Thomas[1], B. L. Ehlmann[1,2], D. E. Anderson[1], S. M. Clegg[3], O. Forni[4], S. Schröder[4,5], W. Rapin[1], P.-Y. Meslin[4], J. Lasue[4], D. M. Delapp[3], M. D. Dyar[6], O. Gasnault[4], R. C. Wiens[3], and S. Maurice[4]

[1]Division of Geological and Planetary Sciences, California Institute of Technology, Pasadena, California, USA.
[2]Jet Propulsion Laboratory, California Institute of Technology, Pasadena, California, USA.
[3]Los Alamos National Laboratory, Los Alamos, New Mexico, USA.
[4]Institut de Recherche en Astrophysique et Planétologie, Université de Toulouse, CNRS, UPS, CNES, Toulouse, France.
[5]German Aerospace Center (DLR), Berlin, Germany.
[6]Mt. Holyoke College, South Hadley, Massachusetts, USA.

Corresponding author: Nancy H. Thomas (nhthomas@caltech.edu)

Key Points:

- Multiple calibration and normalization methods to determine hydrogen content from the hydrogen-alpha LIBS emission line were evaluated
- O 778 and C 248 nm norms have the lowest scatter for the lab set, best correct for distance and successfully determine H for martian rocks
- Non-linear calibrations for high H samples and differences in H between rocks, when natural vs. pelletized, warrant further study

Thomas, N. H., et al. (2018). Characterization of hydrogen in basaltic materials with laser-induced breakdown spectroscopy (LIBS) for application to MSL ChemCam data. Journal of Geophysical Research: Planets, 123, 1996–2021. https://doi.org/ 10.1029/2017JE005467

Abstract

The Mars Science Laboratory rover, Curiosity, is equipped with ChemCam, a laser-induced breakdown spectroscopy (LIBS) instrument, to determine the elemental composition of nearby targets quickly and remotely. We use a laboratory sample set including prepared mixtures of basalt with systematic variation in hydrated mineral content and compositionally well-characterized, altered basaltic volcanic rocks to measure hydrogen by characterizing the H-alpha emission line in LIBS spectra under Martian environmental conditions. The H contents of all samples were independently measured using thermogravimetric analysis. We found that H peak area increases with weight percent H for our laboratory mixtures with basaltic matrices. The increase is linear with weight percent H in the mixtures with structurally bound H up to about 1.25 wt.% H and then steepens for higher H-content samples, a nonlinear trend not previously reported but potentially important for characterizing high water content materials. To compensate for instrument, environmental, and target matrix-related effects on quantification of H content from the LIBS signal, we examined multiple normalization methods. The best performing methods utilize O 778- and C 248-nm emission lines. The methods return comparable results when applied to ChemCam data of H-bearing materials on Mars. The calibration and normalization methods tested here will aid in investigations of H by LIBS on Mars with ChemCam and SuperCam. Further laboratory work will aid quantification across different physical matrices and heterogeneous textures because of differences we observed in H in pelletized and natural rock samples of the same composition.

1. Introduction

Laser-induced breakdown spectroscopy (LIBS) provides chemical information by collecting light emitted by excited atoms, ions, and simple molecules in the plasma generated by laser vaporization of a sample. The ChemCam instrument on the Curiosity rover uses LIBS to determine geochemical composition and can detect the presence of light elements including hydrogen. ChemCam fires a pulsed laser beam at a rock or soil target and ablates a 350- to 550-μm diameter area (Maurice et al., 2012; Wiens et al., 2012). The emission spectrum from

the plasma is recorded by the ChemCam spectrometers over the 240- to 840-nm wavelength range and used to derive elemental compositions (Wiens et al., 2013).

The Curiosity rover is investigating sedimentary rocks that are part of Aeolus Mons, informally known as Mount Sharp, an interior 5-km tall mound within 154-km diameter Gale crater. Hydrogen is a crucial element for Curiosity's characterization of past aqueous environments with liquid water and assessment of habitability. On Mars, water and OH can occur adsorbed on surfaces or in hydrated or hydroxylated minerals, including amorphous phases (Ehlmann & Edwards, 2014). Curiosity employs the Dynamic Albedo of Neutrons (DAN) instrument to assess hydrogen content in the near subsurface (decimeter scale) over a few meter-scale footprint beneath the rover (Mitrofanov et al., 2012). The Sample Analysis at Mars (SAM) instrument can detect H_2O and H_2 released from solid samples upon heating, using the combination of a quadrupole mass spectrometer, a tunable laser spectrometer, and a gas chromatograph to obtain chemical and isotopic compositions of volatiles released (Mahaffy et al., 2012). The Alpha Particle X-ray spectrometer can determine when light "missing" elements are present but cannot determine hydrogen content directly (Campbell et al., 2012). The CheMin instrument can identify crystalline minerals that host hydrogen in their structure (Blake et al., 2012). ChemCam is the only instrument that is both sensitive to hydrogen content and can simultaneously characterize the sample geochemistry at a submillimeter scale. In addition, ChemCam is a remote sensing instrument, so reconnaissance data are acquired daily and the immediate results can serve to motivate follow-up detailed analyses with the rover payload.

Determining the degree and style of aqueous alteration of rock units, including the presence of specific hydrated salts and hydrated silicates, is an important geochemical task for Curiosity and can be aided by analysis of hydrogen with ChemCam data. For example, the water or OH content of basaltic sedimentary materials is a key indicator of the extent to which they interacted with liquid water. ChemCam has demonstrated the ability to recognize hydrated mineral phases and use them for determining environmental conditions. Analysis of calcium sulfate veins in Yellowknife Bay sedimentary deposits with ChemCam identified

H emission supporting hydrated forms of the salt (Nachon et al., 2014; Schröder et al., 2015) that later were determined to be bassanite (Rapin et al., 2016). In addition, H has been detected and characterized in dust and soils (Meslin et al., 2013; Schröder et al., 2014). Schröder et al. (2015) extended this work to drill tailings and rocks, making the first steps toward relative quantification of hydrogen with ChemCam while showing the dependence of the analysis on target type with higher intensities in the tailings than the rocks.

The abundances of major elements and some trace elements in ChemCam data are being quantified by univariate and multivariate modeling of database reference samples and calibration targets on board the rover (Maurice et al., 2016, and references therein). The detection of hydrogen by the 656.5 nm (wavelengths in vacuum will be used throughout this paper) LIBS emission line (H-alpha) is straightforward. Hydrogen has been detected in most of the targets observed by ChemCam (Schröder et al., 2015). Lab work has shown quantifying hydrogen content from this single line is a challenge (Sobron et al., 2012). A second H emission line at 486.13 nm is located at the edge of the ChemCam visible and near-infrared (VNIR) detector where sensitivity is too low for quantitative analysis (Schröder et al., 2015). Recent results from Rapin et al. (2016) have characterized the LIBS H emission for calcium sulfates, while Rapin et al. (2017a) studied H emission for a set of pelletized basalts, fluorhydroxyapatites, hydroxyapatites, opals, and sulfates using a ChemCam model LIBS instrument but did not measure any natural rock samples. A first absolute quantification was then proposed by Rapin et al. (2017a) that only considered a linear calibration curve.

The goal of this project is to qualitatively and quantitatively examine how hydrogen emission varies with composition and to develop calibration curves based on laboratory data, acquired under simulated Martian conditions, which may later be modified and employed to analyze ChemCam and SuperCam (Wiens et al., 2017) LIBS data from Mars. We utilize prepared mixtures of basalt with varying quantities of Mars-relevant hydrated minerals as well as compositionally well-characterized natural, altered basaltic rocks. Some of our samples contain structural H_2O or structural OH, and their H_2O contents and release temperatures were independently determined using thermogravimetric analysis (TGA). Our work builds

on previous studies by Rapin et al. (2017a) and others by introducing new measurements to study the quantification of hydrogen within a basaltic matrix for a larger set of Mars-relevant hydrated materials, important for characterizing chemical matrix effects. We test a variety of normalization techniques for LIBS H to develop a calibration based on our sample set. Our study examines whether the calibration curves remain linear at high weight percent H. We also present LIBS results for a set of natural rocks, which have not been studied in previous laboratory studies, to begin characterization of physical matrix effects related to grain size, sample roughness, and cohesion. We test our methods by applying to ChemCam data to identify the range of hydration of sulfate veins and estimate the hydration of the Martian bedrock at Gale crater.

2. Samples and Methods

2.1 Samples

To characterize LIBS H emission, we created a sample set including both prepared mixtures of basalt with Mars-relevant minerals in varied proportions and compositionally well-characterized altered volcanics (Table 1).

2.1.1 Mixtures

The wide variety of materials we have chosen for our mixtures are Mars-relevant phases, either previously detected on the Martian surface or plausibly present, based on what is known about Martian geochemical environments. In contrast to most terrestrial sediments, Mars sediments contain a significant fraction of primary igneous minerals (e.g., Morris et al., 2016; Rampe et al., 2017; Vaniman et al., 2013), so mixtures of hydrous and igneous minerals are clearly relevant for Mars.

Production of synthetic mixtures has a number of advantages. First, it allows us to systematically increase the proportion of hydrated material to investigate H peak increase in basaltic material, controlling precisely the relative change from sample to sample. Second, chemical matrix effects in LIBS data mean that line emission strength is sensitive not only

Table 1. List of all samples and mixtures.

Sample	Chemical Formula	Number of samples or mixtures	Sample Origin	Sample Source	Years measured (20XX)	Mixture Number[1]
K1919	Basalt	1	Near USGS BHVO-1 locality in Kilauea, Hawaii	Caltech collection	13, 14, 15	
GBW07105 (GBW)	Basalt	1	NRCCRM, China	Brammer	14, 17	
Iceland basalts	rock compositions in Ehlmann et al., 2012	6 samples	Hvalfjordur and Berfjordur, Iceland	Ehlmann et al., 2012	13, 15	
San Carlos basanites	rock compositions in Hadnott et al., 2017	7 samples	San Carlos, AZ	Hadnott et al., 2017	13, 15	
Ca Chloride	$CaCl_2$	6 – K1919	Synthetic, reagent grade	J.T. Baker	13	5
Na Chloride	NaCl	6 – K1919 and GBW	Synthetic, reagent grade	Macron Chemicals	13, 14, 17	1, 14
Calcite (Ca Carbonate)	$CaCO_3$	6 – K1919	Minas, Nuevo Leon, Mexico	Ward's	13	2
Magnesite (Mg Carbonate)	$MgCO_3$	7– K1919	unknown	Ward's	14, 17	7
Gypsum	$CaSO_4 \cdot 2H_2O$	6 – K1919 and GBW	Fremont County, Colorado	Ward's	13, 14, 17	3, 13

Fe (III) Sulfate	$Fe_2(SO_4)_3$	7– K1919	Synthetic, reagent grade	Carolina Chemical	14, 17	10
Mg Sulfate	$MgSO_4$	7– K1919	Synthetic, reagent grade	Macron Chemicals	14, 17	8
Na Sulfate	Na_2SO_4	7– K1919	Synthetic, reagent grade	Carolina Chemical	14, 17	11
Quartz	SiO_2	6 – K1919	NW end of Saline Valley, CA	Caltech mineral collection	13	4
Opal	$SiO_2 \cdot nH_2O$	7– K1919	Colton, San Bernadino Co., CA	Caltech mineral collection	14, 17	12
Hematite	Fe_2O_3	6– K1919	Joan Monlevade, Minas Gerias, Brazil	Caltech mineral collection	13	6
NAu-1	$(Ca,Na,K)_{1.05}(Si_{6.98}Al_{1.02})(Al_{0.29}Fe_{3.68}Mg_{0.04})O_{20}(OH)_4$	7– K1919	South Australia	Keeling et al., 2000	15	15
NAu-2	$(Ca,Na,K)_{0.72}(Si_{7.55}Al_{0.45})(Fe_{3.83}Mg_{0.05})O_{20}(OH)_4$	7– K1919	South Australia	Keeling et al., 2000	15	16
Alunite (with clay mineral impurities)	$KAl_3(SO_4)_2(OH)_6$	7– K1919	Utah	Ward's	14, 17	9
Brucite	$Mg(OH)_2$	7– K1919	Gabbs, NV	Caltech mineral collection	15	17
Epidote	$Ca_2Fe_{2.25}Al_{0.75}(SiO_4)_3(OH)$	7– K1919	Rockbridge CO., VA	Caltech mineral collection	15	20

Muscovite	$KAl_2(AlSi_3O_{10})(F,OH)_2$	7– K1919	Upson County, GA	Caltech mineral collection	15	18
Serpentine	$((Mg,Fe)_3Si_2O_5(OH)_4$	7– K1919	Hoboken, NJ	Caltech mineral collection	15	19

[1]Labeling key for our supplementary dataset available online and for the LANL calibration dataset used for the ChemCam data available on the PDS.

to H content but can also vary due to the total elemental composition of the sample (e.g., Clegg et al., 2009), especially for H (Schröder et al., 2015, and references therein). At the same time, the limited set of chemical matrices and measurement conditions that ChemCam could encounter on Mars may help to reduce the complexity of their effects. Characterization of the H peak within basaltic matrices is thus most relevant for measurements of the Martian surface, which is mostly basaltic.

Mixture samples were produced from reagent grade chemicals or natural mineral samples that were already well characterized by chemical and mineralogical measurements (Table 1). All endmembers were mixed with K1919, a moderate-alkali (2.27 ± 0.01 wt.% Na_2O and 0.52 ± 0.01 wt.% K_2O) Hawaiian basalt chosen for its low hydration. In addition, for a subset of endmembers, mixtures were produced with GBW07105, a higher-alkali basalt (3.32 ± 0.01 wt.% Na_2O and 2.24 ± 0.01 wt.% K_2O) from the Brammer Standard Company. The other minerals chosen included a variety of salts, oxides, and phyllosilicates detected on Mars, some of which are hydrated or hydroxylated. The hydrated and hydroxylated minerals are expected to cause an increase in H line intensity with increasing concentration. The hydroxylated samples (e.g., brucite and epidote) are also important because their hydration is stable in spite of depressurization down to Martian pressures in a chamber. The nominally anhydrous materials (e.g., quartz and calcite) provide a check that H line intensity decreases with increasing concentration of anhydrous minerals in the mixture, thus allowing us to clearly define the limit of detection of the instrument.

The natural samples were first ground using a jaw crusher to produce submillimeter particles. All samples, both the reagent grade chemicals and the natural samples, were then run through a shatterbox for a few minutes to produce powders with grain sizes of <250 μm for 85–90% of the particles (Anderson et al., 2017). This, importantly, is less than the spot size of the laser (≥350 μm). While some grain clumps or individual grains larger than the spot size of the laser existed within powders, we found no sporadic behavior in the shot-to-shot trends with depth that would indicate the laser sampling individual grains rather than a well-mixed powder. After preparation of the powders, we mixed the mineral samples at concentrations of 5, 10, 30, 50, and 70 wt.% with a basalt powder. Based on the shot-to-shot and spot-to-spot LIBS data collected from the mixtures, the powders were well mixed. Table 1 lists the set of mixtures we prepared. For some mixtures, we additionally prepared a mixture at 0.5 wt.% (where seven mixtures are listed in Table 1). Mixed samples were then pressed into pellets at 25 tons of pressure at room temperature.

2.1.2 Rock Samples

In addition to laboratory mixtures, we also measured a set of natural samples including previously characterized altered basalts from Iceland (Ehlmann et al., 2012) and altered basanites from San Carlos, AZ (Hadnott et al., 2017). LIBS measurements were taken of both powdered materials, which were pressed into pellets (prepared using the same methods as described in section 2.1.1) and small rock chips. The Iceland samples were formed in near-neutral pH, by surface and groundwater alteration of basalt lava flows (Ehlmann et al., 2012). The samples show a range of alteration, including filled veins and fractures. Samples from Hvalfjordur include hvalfj011 and hvalfj017, which sample friable rock at the contact between two lava flows; hvalfj025, which samples basaltic rock with celadonite- and silica-filled vesicles; hvalfj054, which samples zeolitized basaltic rock with filled vesicles; and icel009, which samples a massive basaltic outcrop. Both hvalfj011 and hvalfj054 have high-H zeolite inclusions that may have been included in the pelletized samples. The suite of alkaline basalts from San Carlos, AZ, exhibit different extents of alteration and represent weathering of alkaline basaltic rocks in an oxidative, semiarid environment (Hadnott et al.,

2017). The samples vary from SanC-J, the least altered basalt with bright green olivine xenoliths, to SanC-A, a highly altered red-brown basalt with reddish olivine xenoliths. SanC-K is a relatively pristine basalt, SanC-F is a relatively pristine basalt with a gypsum coating, SanC-B is intermediately altered, SanC-C is intermediately altered with red-brown xenoliths, and SanC-I is a highly altered red-brown basalt.

2.2 LIBS Measurements

LIBS spectra were collected using the Los Alamos National Laboratory (LANL) ChemCam-analog instrument described in detail by Clegg et al. (2017). The engineering model (EM) mast unit contains the laser, telescope, and remote micro imager (RMI). It is in an enclosure cooled to 4 °C and is connected by a fiber to the optical demultiplexer, spectrometers, and data processing unit in the body unit outside of the enclosure. The samples are placed into a vacuum chamber, which in less than 1 hr is evacuated and then filled with 7 ± 0.2-mbar CO_2 to simulate Mars-like conditions at room temperature. Samples collected in 2013, 2015, and 2017 were measured at a laser-to-sample distance of 1.6 m while samples measured in 2014 were measured at 3.0 m. The distance difference was a result of the setup of the measurement system at the time and was not an intended experimental variable. Distance corrections were applied during data processing to account for the change in viewing geometry (Clegg et al., 2017; Wiens et al., 2013). The laser operates at 3 Hz with an energy of 14 mJ per pulse. The samples were measured with 50 consecutive laser pulses at each of five different locations across the surface to collect a total of 250 spectra per sample. Emission collected by the instrument's telescope was measured using three detectors across the following wavelength ranges: ultraviolet (UV; 240–340 nm), visible (VIS; 380–470 nm), and VNIR (490–850 nm).

We applied standard ChemCam ground data-processing techniques (Clegg et al., 2017; Wiens et al., 2013) to all LIBS spectra collected at LANL. This processing produces so-called clean, calibrated spectra files and includes the following correction steps: (1) subtraction of the background (measured spectrum with no laser pulse), (2) denoising, (3) continuum removal, (4) wavelength calibration, and (5) application of the instrument response function. The first five laser shots are excluded from analysis due to potential

surface effects, the same standard number removed from ChemCam data from Mars. For analysis of H in the lab, removal of the first shots is especially important because the first shot has high H intensity due to a water surface layer (Kurniawan et al., 2014; Meslin et al., 2013). To minimize the influence of random single shot outlier variation, the median spectrum rather than the average spectrum was computed from the remaining 45 shots from each of the five spots, that is, utilizing 225 spectra.

2.3 Peak Fitting and Normalization of Spectra

The H peak height is not an accurate direct measure of the H emission because of interference from the adjacent C peak at 658 nm and broadening of the H emission line. For this reason, we fit the local 652- to 662-nm spectral region to measure the H emission using peak area. Figure 1 shows an example laboratory spectrum (both before and after continuum removal) including the local H region along with other spectral regions used for normalization. We use a Levenberg-Marquardt least squares minimization algorithm to fit two pseudo-Voigt peaks and a linear continuum. The approximate Voigt function, a fractional combination of a Gaussian profile (expected from pure Doppler broadening) and a Lorentzian profile (expected from collisional broadening), better fits the shape of the peaks than the Lorentzian function typically used. There are a total of nine free parameters in this peak fitting routine (linear continuum slope and intercept, peak height [2], full width at half maximum [FWHM; 2], center location [2], and the fraction Gaussian versus Lorentzian, which is assumed to be the same for both peaks), which is approximately 5 times less than the number of data points in the local H peak spectral region being fit. Additionally, Fe peaks are present in this region at 654.8 and 659.4 nm (Rapin et al., 2017a). We only fit these peaks with six additional parameters when necessary for the highest Fe-containing mixtures: the Fe sulfate and Fe oxide. We estimate the error in calculation of peak area by using the standard deviation of the peak area computed from the five separate spot measurements on a given sample.

We tested six methods for normalizing the hydrogen peak area to compensate for variability in the instrument (such as the laser energy and focus), experimental conditions (such as distance to the target and atmospheric pressure), and target properties (such as the physical

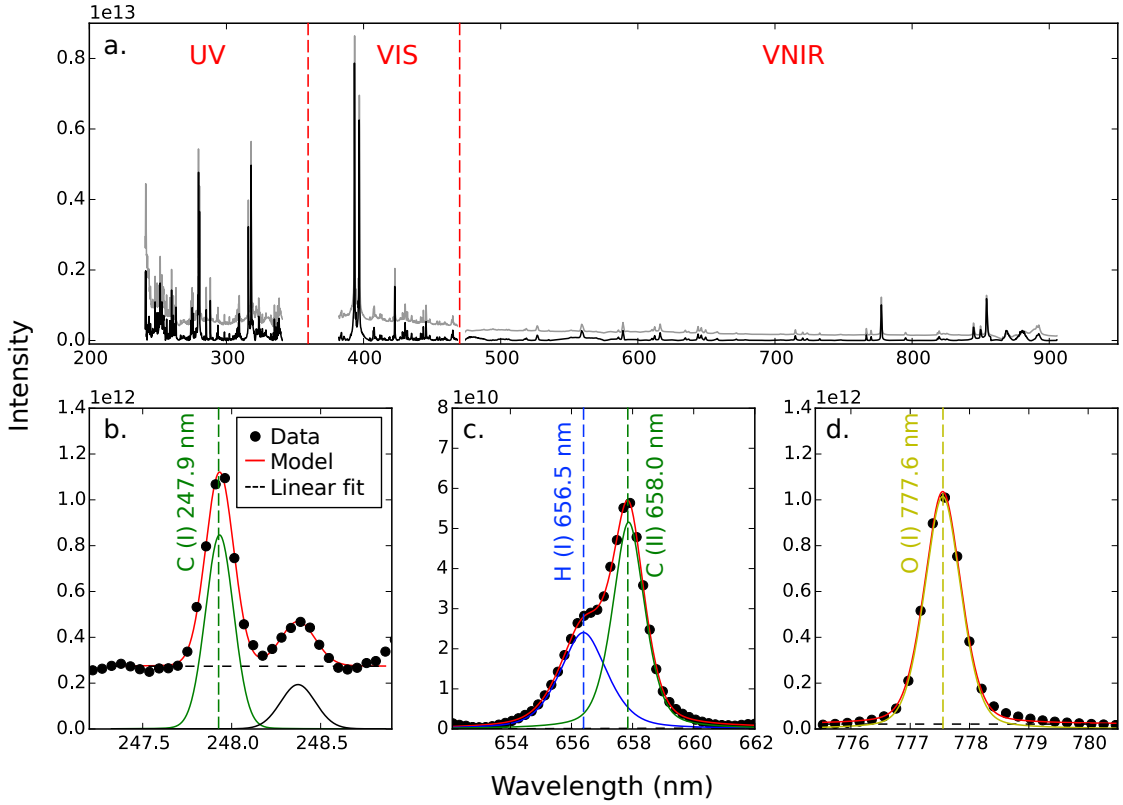

Figure 1. Spectrum of K1919 basalt and gypsum mixture at 50 wt.%. (a) Entire spectrum before (gray) and after (black) continuum removal across the three detectors (UV, VIS, and VNIR). (b) Example model fit to the data for the C (I) peak at 247.9 nm. The final model (shown in red) is a combination of a local linear continuum (black dashed line) and 2 Voigt peaks (green and black solid lines). (c) Spectrum of H-alpha (I) peak at 656.5 nm and C (II) peak at 658.0 nm. (d) Spectrum of O (I) peak at 777.6 nm. UV = ultraviolet; VIS = visible; VNIR = visible and near-infrared.

and chemical matrix). By normalizing we mean dividing the hydrogen peak area by a proxy measured on the same spectrum, for instance the area of another peak. The first three normalization methods rely on using the peak areas of other elements assuming that they will reflect changes in the experimental parameters. The first method normalizes to the area of the C 658-nm peak (actually a mixture of two peaks—C II at 658.0 nm and C II at 658.5 nm

forming a single peak in ChemCam spectra as described by Schröder et al., 2018) from Martian atmospheric CO_2. This peak is fit simultaneously with the H peak at 656.5 nm, which is a neutral peak, in the initial analysis and could behave differently than the ionic C 658-nm peaks (Schröder et al., 2015). We also test normalization to the C I peak at 248 nm, fit separately from the H peak (also using a Voigt function), which is one of the normalization methods preferred by Rapin et al. (2016) and Rapin et al. (2017a). A potential complication of this method is that the C 248-nm peak is measured on a different detector than the H peak and detector behavior variability would not be corrected for. The third method normalizes to the oxygen peak at 778 nm, a triplet of neutral atomic emission peaks, which results from oxygen in atmospheric species and the target (Gasnault et al., 2012). The O peak area is also fit with a Voigt function. Another method tested is that previously used by Schröder et al. (2015), normalization to the continuum emission in the spectral region near the H peak, which results from Bremsstrahlung radiation and the broad tails of strong emission lines from other elements. This technique requires independent data processing, following all the processing steps normally required to generate the clean, calibrated spectra processed files except for continuum removal. Then, the continuum emission is estimated using the value of a nearby peak-free spectral region, here taken to be 660.0 nm. We also tested two standard ChemCam normalization methods called Norm 1 and Norm 3. Norm 1 normalizes the spectrum by the total spectral intensity across all detectors, and Norm 3 normalizes the spectrum by the spectral intensity of the VNIR detector only, which is the detector for the H-alpha line, both after continuum subtraction. These two techniques depend on the emission lines and, therefore, elements present in the sample, so can be impacted by variations in composition.

2.4 Independent Characterization

Additional powders of the same sample endmembers and a subset of the mixtures (10 and 50 wt.% samples) were independently characterized by Activation Laboratories Ltd. (Actlabs) using flux-fusion inductively coupled plasma optical emission spectroscopy for the

major oxides, instrumental neutron activation analysis for Cl, and infrared spectroscopy for C and S to verify the endmember composition and the accurate production of the mixtures.

The H (or H_2O) content of a given mineral must be measured and cannot be determined from stoichiometry because samples can contain adsorbed and structural H_2O or OH such that even nominally anhydrous minerals often contain measurable amounts of hydrogen. The amount of H_2O incorporated depends on both pressure and temperature, which makes determining hydration challenging, particularly under different environmental conditions. TGA was used to independently characterize the hydrogen content of all samples by measuring the weight percent H_2O released upon heating. The release temperature of water serves as a proxy for how easy or difficult samples are to dehydrate upon exposure to low pressures, as in the Mars chamber used for LIBS measurements. TGA measurements were performed using a Perkin-Elmer STA 6000 instrument. Samples were heated in air to 900 °C at a rate of 10 °C/min while monitoring weight change. Samples were then held at 900 °C for 1 hr to ensure all H_2O was removed, again, while monitoring weight change.

We estimated the total weight percent H_2O for each of our samples by calculating the weight percent lost over the temperatures where water is removed as described by Földvári (2011). First, adsorbed and nonstructural H_2O are removed at temperatures typically below 150 °C as evidenced by the weight percent loss of our samples below 150 °C (first column of Table 2), a temperature chosen as a reference similar to previous studies (e.g., Földvári, 2011; Vaniman & Chipera, 2006). At higher temperatures, generally near 500 °C, structural H_2O is lost. Besides the exceptions listed next, we calculated the total H_2O content of our samples using the sample's total weight lost over the entire TGA temperature range plus the additional 1 hr of heating at 900 °C. The exceptions to this are (1) SO_4 is released from the Fe sulfate, Na sulfate, and alunite samples at temperatures above 600 °C, so weight percent H_2O for these minerals was calculated using temperatures below 600 °C. (2) Weight percent H_2O for NaCl was calculated from the weight lost below 150 °C because halite does not hydrate under nonzero humidity and should only have small amounts of adsorbed water present. Any

Table 2. Thermogravimetric analysis (TGA) results. Cumulative weight percent lost in the <150˚C, <400˚C, and <900˚C temperature ranges. Error in TGA measurements is ± 0.015 wt. %. See text (Section 2.4) for details of the computation of H_2O wt. % for each phase. H wt. % is computed from stoichiometry from H_2O wt. %.

Sample	**Loss below 150˚C (wt. %)**	**Loss below 400˚C (wt. %)**	**Loss below 900˚C (wt. %)**	H_2O **(wt. %)**	**H (wt. %)**
Ca Chloride	4.82	29.76	30.75	30.75	3.44
Na Chloride	0	0	4.08	0	0
Ca Carbonate	0.02	0.08	43.48	0.08	0.01
Mg Carbonate	0.59	0.89	53.29	0.89	0.10
Alunite	1.24	2.74	9.67	7.94	0.89
Gypsum	2.97	20.71	20.9	20.9	2.34
Fe Sulfate	8.09	27.17	69.64	27.46	3.07
Mg Sulfate	2.19	15.65	16.58	16.79	1.88
Na Sulfate	0	0	0.09	0	0
NAu-1	6.26	9.92	14.86	14.86	1.66
NAu-2	6.98	9.46	13.55	13.55	1.52
Quartz	0	0	0	0	0
Opal 1	0.98	2.33	3.83	3.83	0.43
Opal 2	0.7	2.04	3.6	3.6	0.40
Opal avg.	0.84	2.18	3.72	3.72	0.42
Brucite	0.33	3.49	30.88	30.88	3.46
Epidote	0.11	0.36	0.61	0.76	0.09

Hematite	0.08	0.51	0.6	0.6	0.07
Muscovite	0.44	1.2	4.14	5.26	0.59
Serpentine	1.27	2.58	10.28	10.28	1.15
hvalfj011 1	1.72	2.75	3.41	3.48	0.39
hvalfj011 2	1.52	2.54	3.18	3.28	0.37
hvalfj011 avg.	1.62	2.64	3.3	3.38	0.38
hvalfj017	4.89	7.67	9.55	9.55	1.07
hvalfj025 1	0.41	0.56	0.46	0.71	0.08
hvalfj025 2	0.57	1.01	0.83	1.22	0.14
hvalfj025 avg.	0.49	0.78	0.64	0.97	0.11
hvalfj054 1	2.57	5.93	7.22	7.23	0.81
hvalfj054 2	1.87	5.2	6.14	6.14	0.69
hvalfj054 avg.	2.22	5.57	6.68	6.69	0.75
icel009 1	0.54	0.75	0.86	1.01	0.11
icel009 2	1.52	2.52	2.89	2.96	0.33
icel009 avg.	1.03	1.64	1.88	1.98	0.22
K1919 1	0.03	0.11	0.12	0.12	0.01
K1919 2	0.02	0.11	0.12	0.12	0.01
K1919 avg.	0.02	0.11	0.12	0.12	0.01
GBW07105 1	0.83	2.94	3.3	3.5	0.39
GBW07105 2	0.82	2.94	3.29	3.49	0.39

GBW07105 3	0.84	2.98	3.32	3.53	0.40
GBW07105 4	0.7	2.84	3.19	3.4	0.38
GBW07105 avg.	0.8	2.93	3.27	3.48	0.39

weight percent change above 150 °C is due to melting (at 800 °C) and evaporation of the sample. On the other hand, our Ca chloride sample is nominally anhydrous but readily hydrates under nonzero humidity, so the entire temperature range is used. (3) For the nominally anhydrous carbonate minerals, the high temperature weight loss is due to CO_2 being burned from the sample, so weight percent H_2O was calculated using loss below 400 °C. (4) For some of the basalt samples, the minimum weight often did not occur at the highest temperature reached (900 °C). Instead, the basalt samples sometimes reached a weight percent minimum at slightly lower temperatures. This difference (<0.5 wt.%) is likely a minor calibration issue with the instrument at highest temperatures rather than a real weight percent gain at high temperatures. Therefore, we calculated the weight percent H_2O for the basalt samples using the minimum value of the TGA curve.

We estimated the precision of the TGA measurements by repeat measurements of a few endmembers (the K1919, GBW07105, hvalfj011, hvalfj054, and icel009 basalts and the opal sample). While most of the samples are very consistent across runs with repeat measurements having standard deviations of 0.05–0.26 wt.%, two of the natural basalt samples (icel009 and hvalfj054) showed variation of ~1 wt.%, perhaps indicating aliquot variation for these samples. Ultimately, the accuracy of the TGA measurements for use in determining H content is limited by potential water loss during pump down to vacuum (see section 3.2).

2.5 ChemCam Data

ChemCam spectra are collected by Curiosity using a very similar LIBS instrument to the LANL analog instrument used for our study. Typical ChemCam observations on a given point collect 30 shots at 3 Hz. When we average laser pulse spectra obtained at a single

observation point, the first five shots are ignored due to potential contributions from surface materials like dust or thin coatings. We fit the ChemCam spectra using the same procedures as the laboratory data with an additional constraint on the FWHM of 0.9 nm, a physically reasonable upper limit determined based on the largest H FWHM observed in the laboratory data. We also apply the Earth-to-Mars correction as described by Clegg et al. (2017) to account for differences in sensitivity between the LANL laboratory and ChemCam instruments. Targets are generally 2.2 to 7 m from the instrument with most at about 3 m (Maurice et al., 2016). ChemCam collects images of the targets in complement to the LIBS spectra using the RMI. We have visually classified individual ChemCam points using the RMI images up to sol 1815 in order to identify where veins have been targeted for comparison with the results of Rapin et al. (2016; 69 points) and where ChemCam has shot smooth bedrock (2,098 points) for calculation of its H content.

3. Results

3.1 Thermogravimetric Analysis

TGA analysis shows our samples contain between 0 and 31 wt.% H_2O or 0 and 3.5 wt.% H (Figure 2; Table 2). The minerals with structural H in metal-OH bonds lost H_2O at high temperatures (≥400 °C). Other minerals lost weight at stepped temperatures. CaCl2 tends to be hygroscopic and shows dehydration at 200 °C. In contrast, NaCl lost weight only through melting and evaporation of Cl (Figure 2a). The carbonate minerals (Figure 2b) we measured lost CO_2 at high temperature (>700 °C) in the general reaction $XCO_3 \rightarrow XO + CO_2$. Additionally, a small amount of adsorbed or loosely bound water was released at low temperatures (<200 °C) from the Mg carbonate (Figure 2b). While nominally anhydrous, the Mg and Fe sulfates hydrate readily under nonzero humidity. For these and for gypsum, dehydration occurs at temperatures well below 400 °C while SO_3 is released above 650 °C (Figure 2c). Figure 2d shows TGA results for a variety of Mars-relevant silicates and oxides, some of which are hydrated. For the nontronite samples, NAu-1 and NAu-2, endothermic dehydration occurs between 100 and 200 °C and dehydroxylation occurs between 400 and 500 °C (Ding & Frost, 2002; Földvári, 2011). Opal was measured twice using TGA, and the

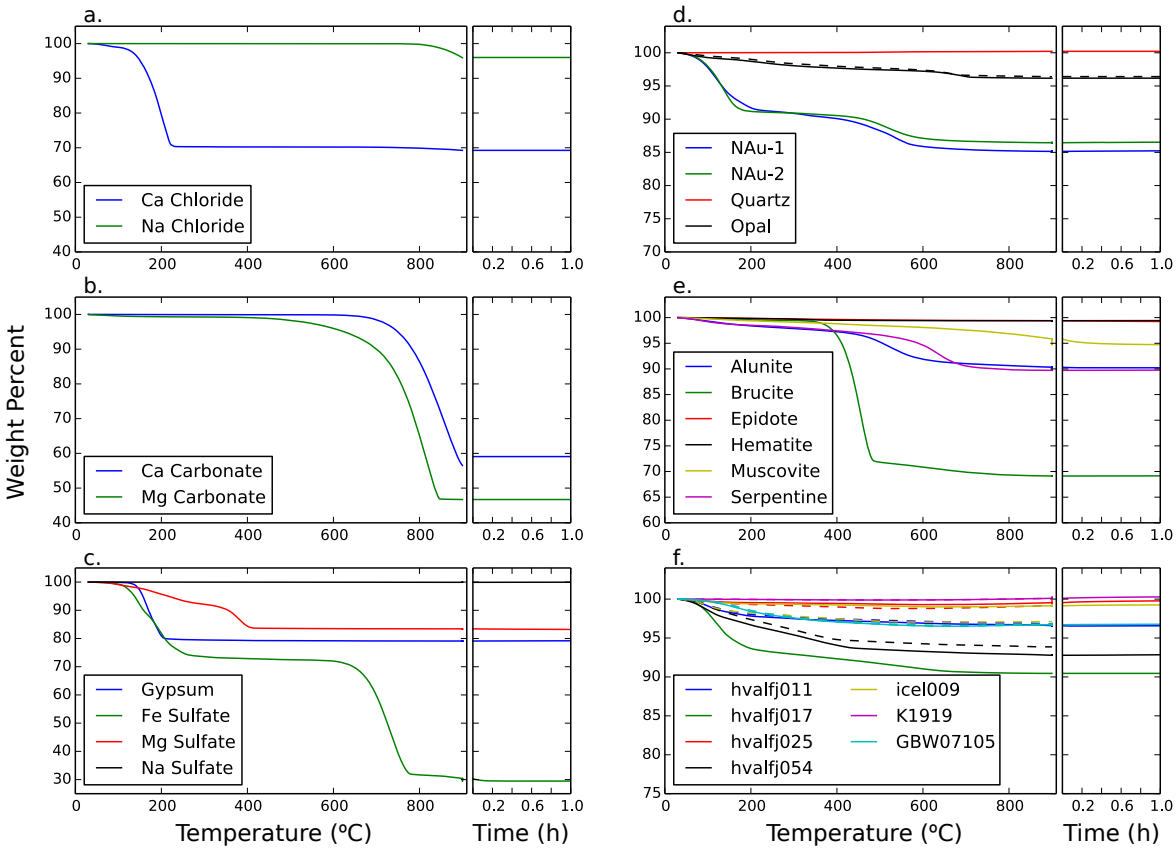

Figure 2. Thermogravimetric analysis for (a) chlorides; (b) carbonates; (c) sulfates; (d) silica, hydrated silica, and nontronite standards; (e) hematite and minerals, which, based on stoichiometry, are only hydroxylated; and (f) basalts and rock samples.

weight percent loss trends are very similar between samples. Opal dehydrates by losing H_2O from its structure continuously up to approximately 700 °C. As expected, the quartz sample is not hydrated and does not lose any appreciable weight in the 100–900 °C range. Most hydroxylated materials did not dehydrate until 400 °C, although alunite and serpentine show evidence for continual slow dehydration over the temperature range, suggesting some H_2O or impurities (Figure 2e). Hematite, as expected, had no loss. Finally, the basaltic endmembers used in this experiment (K1919, 0.1 wt.% H_2O; GBW07105, 3.5 wt.% H_2O) and natural samples from Iceland measured with TGA show loss over a wider range of temperatures (from the start of heating to 700 °C; Figure 2f). The most altered and smectite

rich sample (79 wt.% smectite), hvalfj017, has the highest weight percent loss. Loss for the Iceland natural samples was assumed to be in the form of H_2O as other volatile-bearing minerals were not detected in X-ray diffraction (Ehlmann et al., 2012).

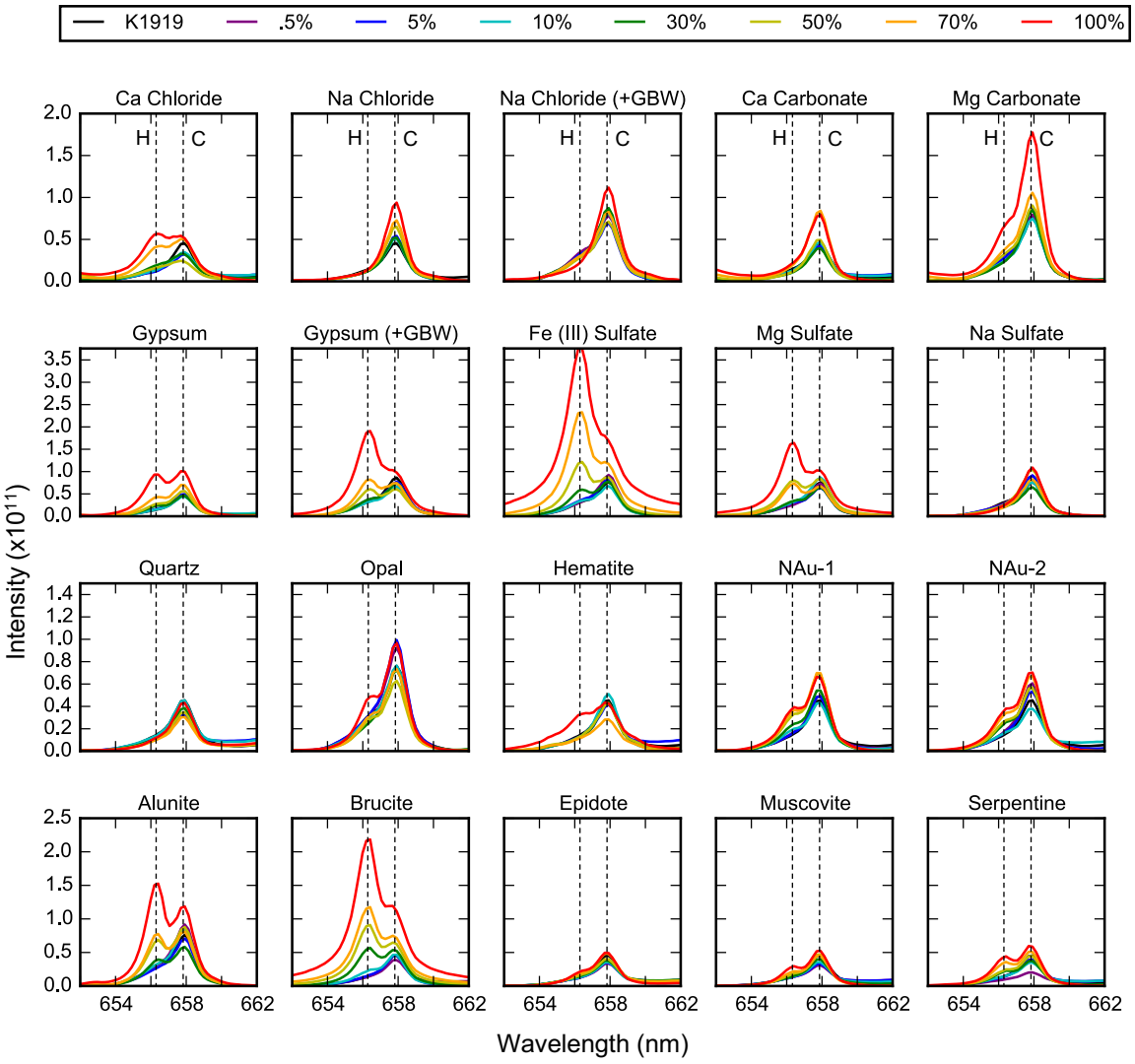

Figure 3. Laser-induced breakdown spectroscopy spectra of all laboratory mixtures showing the local H peak region from 652 to 662 nm including the H (I) peak at 656.5 nm and the C (II) peak at 658 nm. Colors indicate weight percent of listed endmember from 0% for pure basalt (black) to 100% pure mineral endmember (red).

3.2 LIBS H Peak Versus H Content

The C peak at 658 nm due to the CO_2 atmosphere in the sample chamber is clearly visible in all mixtures near the H peak (Figure 3). The laboratory mixtures that show an increasing H peak with weight percent endmember are gypsum (mixed with both K1919 and GBW07105 basalts), Ca chloride, Mg sulfate, alunite, Fe (III) sulfate, opal, NAu-1, NAu-2, brucite, muscovite, serpentine, Mg carbonate, and epidote. No appreciable change is observed for Na chloride, Ca carbonate, quartz, hematite, and Na sulfate. In some cases, decreasing H was observed with increasing weight percent endmember in question. For example, the NaCl with GBW07105 mixture shows decreasing H because the basalt is more hydrated than halite. Adjacent to the H peak in the 100 wt. % hematite sample, there is a strong emission line at ~655 nm. This Fe emission line is only observed in the highest FeO weight percent samples of the basalt-hematite and basalt-Fe-sulfate mixtures. This peak is fit for the hematite and Fe sulfate mixtures but may not be fully accounted for in the case of Fe sulfate (Figure 4).

We used the methods described in section 2.2 to peak-fit all the mixtures that showed increasing H emission with weight percent endmember. Then, we compared peak area H with weight percent H determined using TGA. H peak area (or signal) increases with H weight percent for all the mixtures, though the curve shape and slope differ by mixture (Figure 4). We fit three different trend lines to the observed signal by minimizing the modified χ^2 calculated using the equation: $\boldsymbol{\chi^2} = \frac{(y-M)^2}{\sigma_y^2+\sigma_x^2(\frac{dy}{dx})^2}$; where M is the model value and σ_x and σ_y are the errors on x (weight percent H) and y (LIBS H signal), respectively. The modified χ^2 allows us to take into account error both in our fit LIBS signal (described in section 2.3) as well as error in our TGA measured weight percent H values. The error in weight percent H due to the precision of our TGA measurements is relatively small as we discuss in section 2.4, but the error due to accuracy is larger. One effect that may influence the trends shown in Figure 4 and cause scatter in the data is loss of water after placement in the chamber

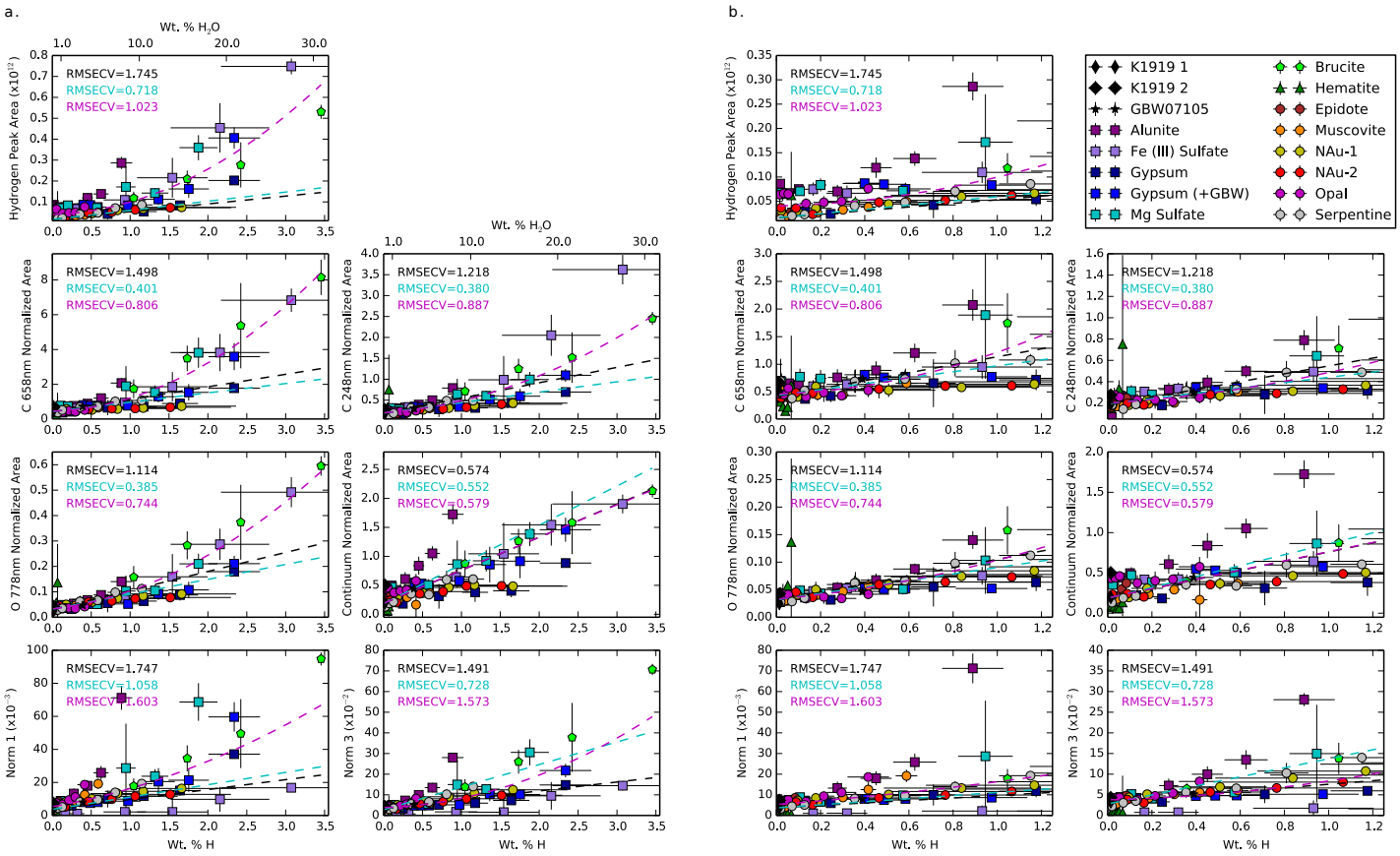

Figure 4. Hydrogen emission peak area versus weight percent hydrogen for full temperature range for all samples, as reported in Table 2, for the (a) full weight percent range and (b) the low weight percent range. The black dashed line is a linear fit to all the samples; the turquoise line is a linear fit to samples with H wt. % < 1.25%; and the magenta is a second-order polynomial fit to all samples. RMSECV values (calculation described in section 3.2) are included for comparison between normalizations. Error bars are computed using methods described in section 2.2. For the continuum normalization, the best linear fit (black) and polynomial fit (magenta) trend lines overlap. Trend line coefficients are included in Table A1. RMSECV = root-mean-square error cross-validation.

for measurement. Because our samples are pumped down to vacuum and then set to 7-mbar CO_2, our samples almost certainly lost H_2O before LIBS measurement during pump down. We take the weight percent loss below 150 °C as a proxy for the potential amount of adsorbed or loosely bound water lost in the vacuum chamber during the LIBS measurement process (Milliken & Mustard, 2005; Vaniman & Chipera, 2006). We use this quantity, column 2 of Table 2, as σ_x, the accuracy in our TGA measurements.

H peak area increases versus weight percent for all six normalizations (Figure 4). Examination of the best linear fit to all mixtures and basalt samples (black dashed line; Figure 4) shows that above 1.25 wt.% H, the increase in LIBS H signal is not clearly linear, particularly for the C 658- and O 778-nm normalizations. We also fit a second-order polynomial function ($ax^2 + bx + c$) to the data (shown in magenta) to describe this increase. Mixtures containing less than ~1.25 wt.% H mostly follow a linear relationship, so we also show a separate linear fit to all measurements below 1.25 wt.% H (shown in turquoise). The coefficients for all the fit trend lines are included in Table A1. Alunite has a clearly distinctive trend, diverging from the linear fits even at low weight percent H. The sulfates like Fe and Mg sulfate tend to fall above the fit trend line even for some lower weight percent H mixtures. For Fe sulfate the higher H peak area than expected from the TGA results is likely due to interference from the Fe peaks adjacent to the fitted H peak, as evidenced by a small shift in the H peak center location. Observed differences between sample suites in the normalized area versus weight percent H are similar across normalizations.

To test the goodness of fit to the three models (linear, low weight percent linear, and second-order polynomial), we calculated the root-mean-square error (RMSE) of cross-validation (RMSECV), which leaves out one data point to estimate how well the model built on the rest of the data set performs for unknown cases. We used the equation

$$\boldsymbol{RMSECV} = \sqrt{\frac{\sum_{i=1}^{n}(\boldsymbol{y_i} - \widehat{\boldsymbol{y}}_i)^2}{\boldsymbol{n}}}$$

where y is the measured values of LIBS H signal, by is the LIBS H signal estimated by cross-validation (where the value for each object i is estimated using a model that was built using a set of objects that does not include object i), and n is the total number of data points. RMSECV values were normalized by the median value of the data set because the LIBS H values differ by orders of magnitude across the different normalizations. Normalization to O 778 nm, C 248 nm, and the continuum visually produce the least scatter in the data and produce the lowest RMSECV values for the full-range linear model (Figure 4). Nonetheless, the fits clearly show that the relationship between peak area and weight percent H_2O is not linear for the full sample suite over the 0–3.5 wt.% H range examined. The polynomial model performs better for the higher weight percent H samples and produces low RMSECV values for norm1 and norm3. Calculation of the x axis as mole percent H instead of weight percent H does not affect this finding (Figure A2).

Scatter is introduced into our measurements due to loss of H_2O before LIBS measurement in the vacuum chamber. Consequently, we next consider only a subset of the mixtures that have structurally bound H (brucite, epidote, muscovite, nontronite, and serpentine; Figure 5). These samples also released some H at low temperatures in our TGA experiments, so we compare LIBS H peak area with the weight percent H calculated from weight loss above 150 °C because nonstructural H_2O should be lost by this temperature (Milliken & Mustard, 2005; Vaniman & Chipera, 2006), although we still consider our x axis error bars as the TGA weight percent lost below 150 °C. For all normalizations, LIBS H emission increases monotonically with weight percent H. Scatter from the linear trend lines for these fits (Table A1) is considerably lower than for the full sample set for all normalizations (Figures 4 and 5). However, the trend still significantly steepens for high H contents, wt.% H > 1.25 wt.%, in the brucite mixture.

We quantify the uncertainty in our ability to predict weight percent H from the LIBS H signal by measuring the scatter from our fit linear trends. The RMSE for the fit lines for the O 778 nm and C 248 nm normalizations for the Figure 5 samples are, respectively, ±0.42 and ±0.43

wt.% H for the full linear fit, ±0.24 and ±0.18 wt.% H for the linear fit of samples with <1.25 wt.% H, and ±0.31 and ±0.30 wt.% H for the polynomial fit.

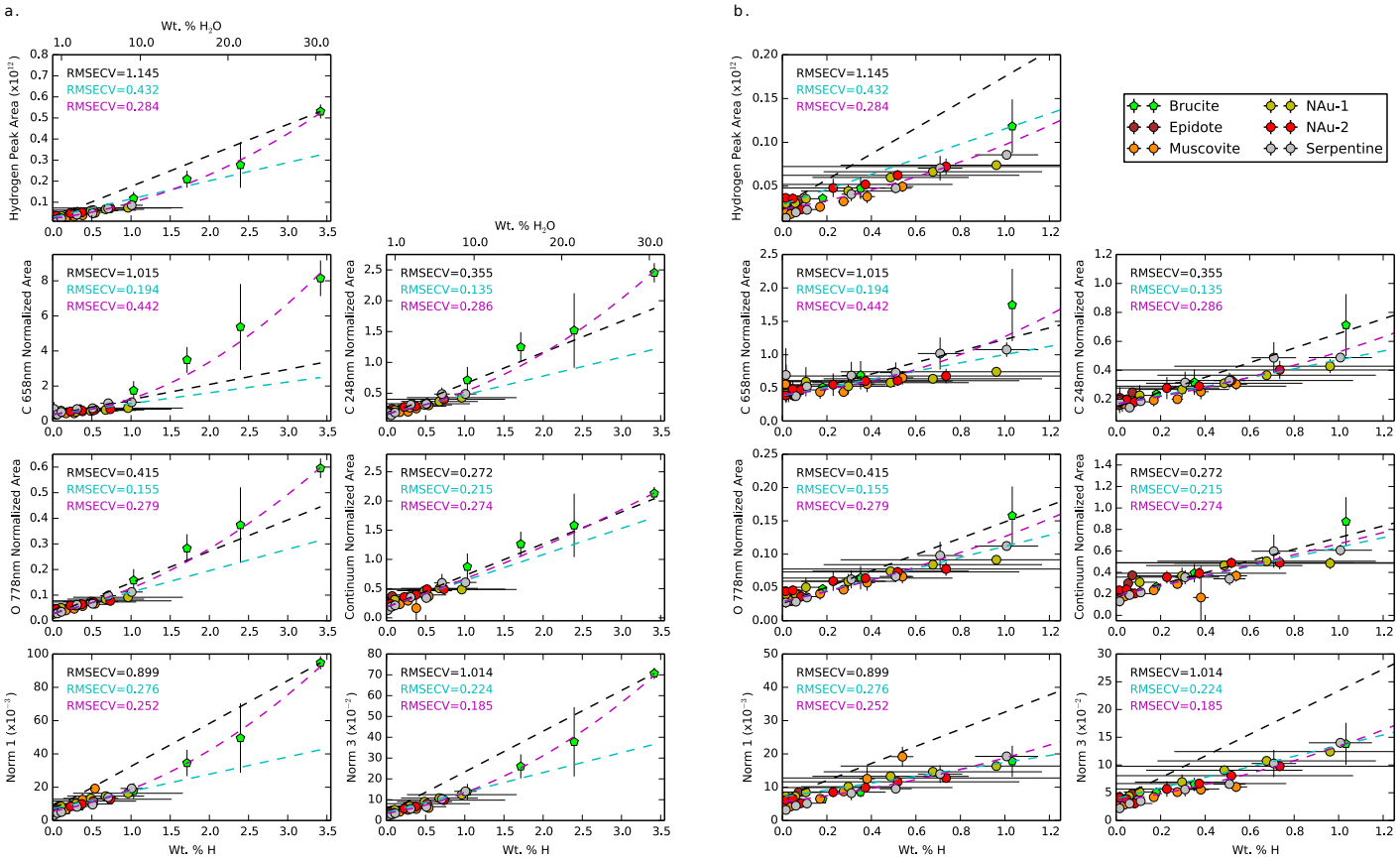

Figure 5. Hydrogen emission peak area versus weight percent hydrogen, for the full weight percent range (a) and low weight percent range (b), when calculated only from water temperatures >150 °C, for a subset of the sample data from Figure 4, including only those samples that have bound OH. The black dashed line is a linear fit to all the samples; the turquoise line is a linear fit to samples with H wt.% < 1.25%; and the magenta is a second-order polynomial fit to all samples. Trend line coefficients are included in Table A1. RMSECV = root-mean-square error cross-validation.

Our ability to detect the LIBS H signal is limited by interference due to the adjacent C peak and Fe peak. We can use our lowest weight percent H samples where H emission is observed to estimate the detection limit as done by Rapin et al. (2017a). Samples with weight percent H over ~0.9 wt.% H_2O visually exhibit an inflection at 656.5 nm such as the Mg carbonate and epidote endmembers (Figure A1). In some instances, an asymmetry of the C 658-nm peak is observed, which may be indicative of H at even lower abundances, for example, Ca carbonate. Samples with approximately 0 wt.% H_2O like Na chloride exhibit the smallest amount of asymmetry in the C 658-nm peak. We can also calculate the detection limit using the standard equation LOD = 2sm, where s is the standard deviation of the measurements for our lowest concentration samples and m is the slope of the fit trend line. Using our low concentration calibration curves in Figure 5, we find a detection limit of 0.10 wt.% H for the C 248-nm normalization and 0.04 wt.% H for the O 778-nm normalization. This equates to 0.4–0.9 wt.% H_2O, which is similar to value where the peak visually becomes apparent as described above.

3.3 Shot-to-Shot Behavior

The peak intensity of H typically decreases with increasing laser shots (Figure 6; as also seen by Rapin et al., 2017a). After the first shot with high H, there is a systematic, slow decrease in intensity with shot number. The 50, 70, and 100 wt.% brucite mixtures are exceptions and show relatively constant, high H intensity across all shot numbers (Figure 6b).

We expect the lab chamber to remain at constant pCO_2, but because laser-target coupling can vary with target texture and composition, C and O emission may not necessarily remain constant. Empirically, we have found that emission of the C peak at 658 nm, the C peak at 248 nm, and the O peak at 778 nm all decrease steadily with shot number like H (Figure 6; Figure A3). In contrast, the continuum level adjacent to the H peak increases with shot number across all sample locations. Nevertheless, division by any of these still results in monotonic H peak area increase with weight percent H (Figures 4 and 5).

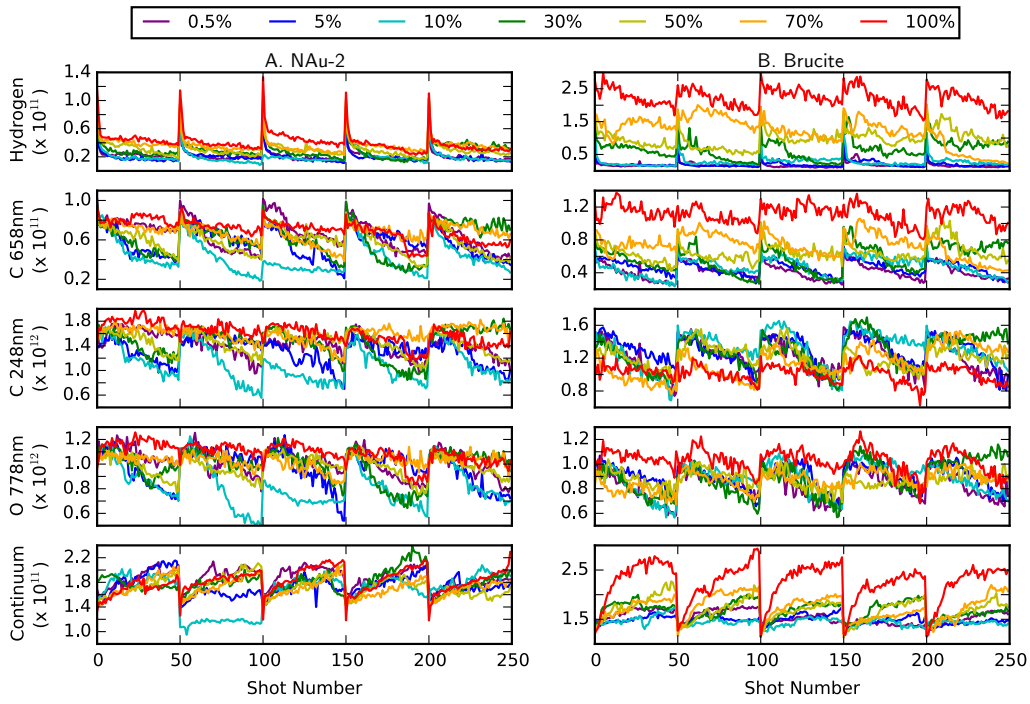

Figure 6. Variation in H, C (II) 658-nm, C (I) 656-nm, and O (I) 778-nm peak areas and continuum emission nearby H (660 nm) with shot number for a low-moderate weight percent H mixture (NAu-2) and a high weight percent H mixture (brucite). Each 50 shots is a different location on the sample and colors indicate increasing weight percent NAu-2 or brucite.

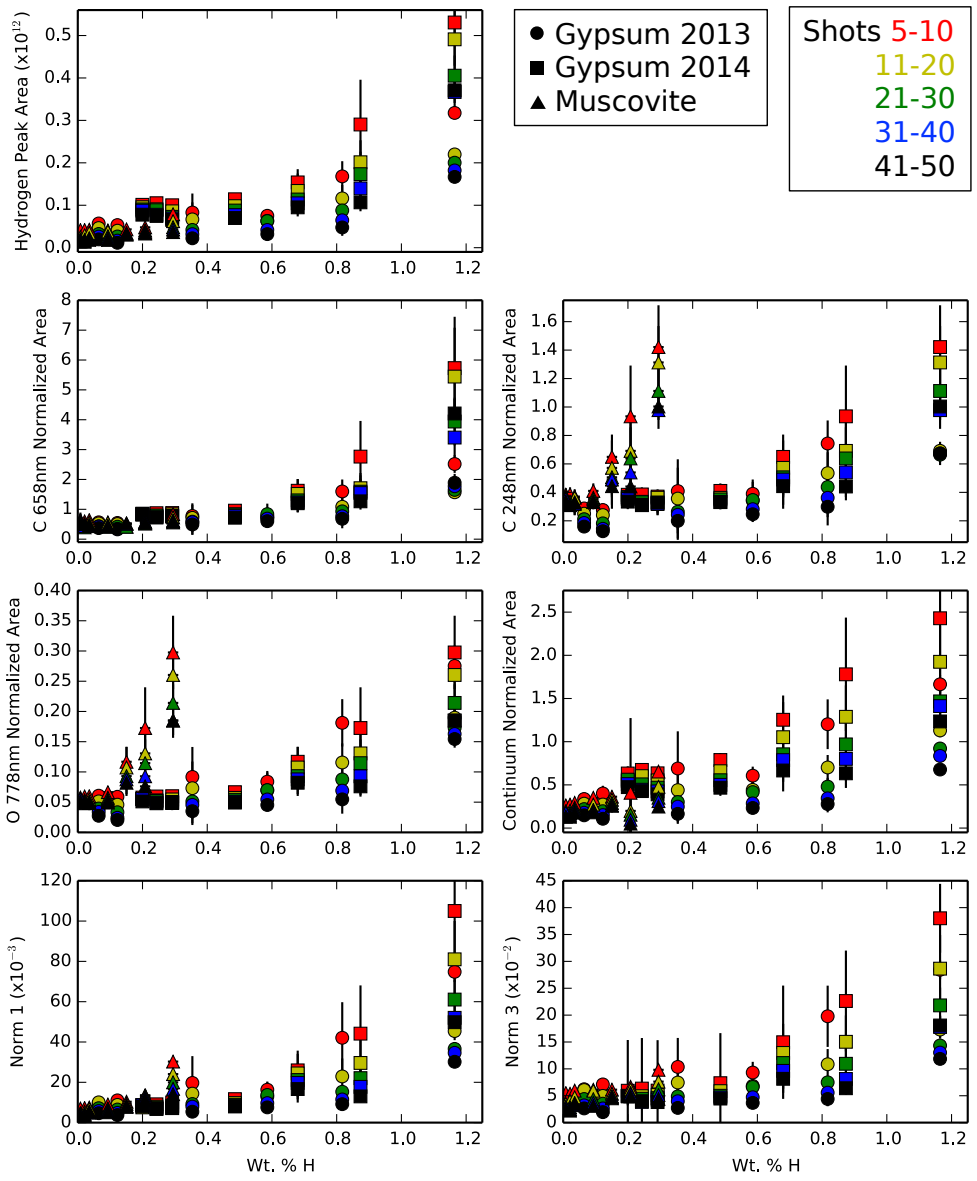

Figure 7. Variation in the increase in laser-induced breakdown spectroscopy H signal versus weight percent H for different ranges in shot number: 5–10 (red), 11–20 (yellow), 21–30 (green), 31–40 (blue), and 41–50 (black). Under all normalizations, the H signal decreases with increasing shot number.

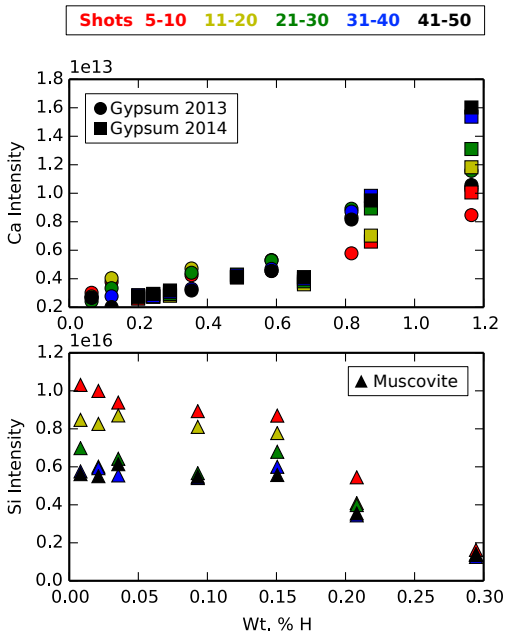

Figure 8. Top: Ca emission line (318.025 nm) variation with shot number in gypsum mixture. Bottom: Si emission line (188.242 nm) trends with depth for muscovite mixture. Ca increases and Si decreases with increasing shot number: 5–10 (red), 11–20 (yellow), 21–30 (green), 31–40 (blue), and 41–50 (black).

The range of shot numbers used to calculate the LIBS H signal impacts the calibration curves across all normalizations (Figure 7). The signal decreases with increasing shot number leading to lower slopes with shot number for the mixture sets shown: gypsum and muscovite. Similarly, most major element lines like Si show decreasing intensity with shot number although Ca lines in the gypsum mixture increase in intensity with shot number (Figure 8).

3.4 LIBS H Line in Natural Samples

H peaks are not prominent for the powdered and pelletized San Carlos and Iceland samples but, generally, asymmetry of the C emission line indicates a hydrogen contribution from aqueous alteration that is highest for the most-altered samples (Figure 9). Among the San Carlos samples, the least altered (SanC-J) shows only a broad shoulder to the C peak at 658 nm indicative of low H whereas even minimally altered samples like SanC-B (<10% clay

mineral) show an H peak (Figure 9a). The sedimentary sample, SanC-S, has the highest H peak. In the Iceland samples (Figure 9b), the existence of the H peak suggests hydration/hydroxylation of the basaltic rock. The samples hvalfj054 and hvalfj017 have the highest H peak, consistent with their having the highest hydrous mineral content (Ehlmann et al., 2012), though the difference with other samples is small.

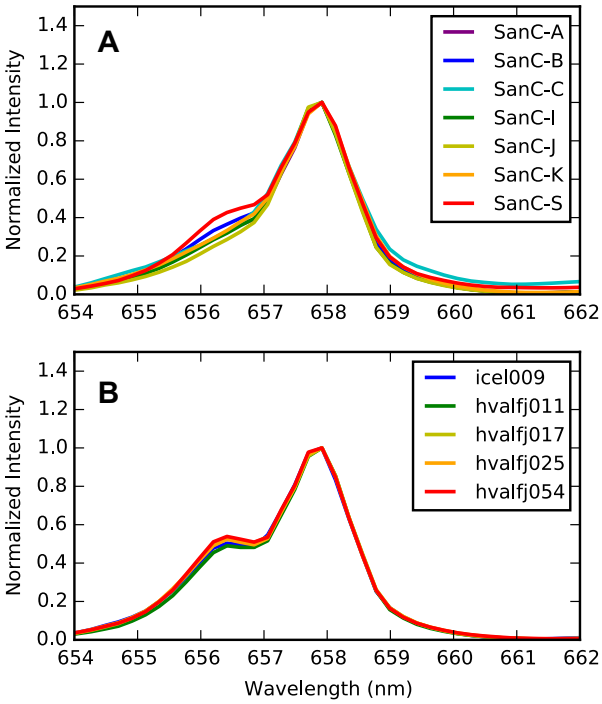

Figure 9. Laser-induced breakdown spectroscopy spectra normalized to the height of the C peak at 658 nm of all pressed pellet natural rock samples measured from San Carlos (a) and Iceland (b).

Interestingly, all the corresponding rock chips from the Iceland natural samples show a change in H peak shape relative to the powdered pellets, and the H emission peak is typically higher for the rock chip spectra than for the powdered pellet spectrum. As expected, some rock chips show more variation in H peak area across the different spots on the target, for

example, hvalfj054, which has zeolite-filled vesicles (larger than the spot size of the laser spot size; Figure 10).

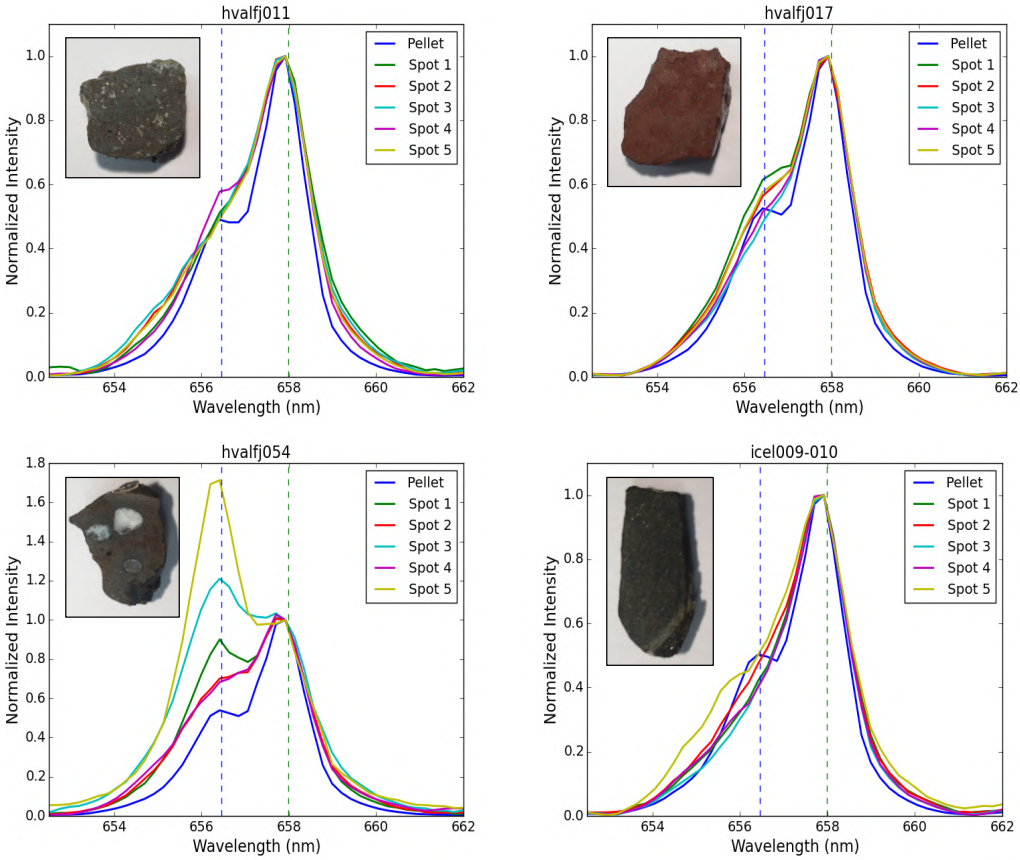

Figure 10. Physical matrix comparison. Laser-induced breakdown spectroscopy spectra normalized to the height of the C peak at 658 nm of pelletized (all five spots on the pellet were averaged) and rock chip samples from Iceland.

Normalized H line area versus weight percent H (lost above 150 °C) was also calculated for the natural rock chips and powders and compared to the linear fit from Figure 5 (Figure 11). Because these natural samples contain smectite clays, mixtures of the nontronite samples (NAu-1 and NAu-2) and basalt are also shown for comparison. The rock chip samples do not fall on a linear trend and show large scatter, but the pelletized samples generally follow the nontronite samples in the normalized data. Both basalts measured in the second batch of

samples, GBW07105 and K1919, do not fall near the linear fit (see section 4.1 for discussion). The O 778-nm, C 248-nm, and continuum normalizations provide the best match between the natural samples and H linear fit calibration lines.

3.5 Use of Calibrations to Determine H in ChemCam Spectra from Mars

We examine the sensitivity of interpretations of ChemCam LIBS spectra to the different calibration approaches. One example important to interpreting Mars data is measurement of the hydration state of various salts, which have been reported based on orbital data and found in situ by rover missions. We use the Figure 5 calibration lines (Table A1) for each of the normalizations from our work to predict the H peak values for bassanite ($CaSO_4 \cdot 0.5\ H_2O$) and gypsum ($CaSO_4 \cdot 2\ H_2O$) on Mars and then compare these to the H signal observed for veins up to sol 1248 (same sample set examined by Rapin et al., 2016). Under all normalizations, the distribution of the ChemCam LIBS data normalized is closer to bassanite and would more likely be predicted to be this mineral using all of the normalizations. In particular, normalization to C 248 nm, O 778 nm, and Norm 3 all agree well on bassanite composition. The normalized H signal predicted for gyp- sum falls outside of the observed ChemCam vein distribution for all calibration approaches except C 658 nm and Norm 1, and for these calibrations the mean of the measured distribution falls between bassanite and gypsum.

We also use our data to examine the water content of Martian rocks, specifically the Murray formation, a fine- grained, thinly laminated mudstone facies, which is the lowermost strata of the Mount Sharp group. We analyzed the RMI images by eye to exclude rough targets, those where ChemCam shot loose sediment (sand and dust), and diagenetic features that may have a different H signal. We also exclude points with bad focus and low major-element totals (<87%). In total, we included 229 ChemCam targets in our analysis from sols 766–1815. Using the C 248-nm normalization, the range in H content for the middle 50% of the data is 2.0– 4.1 wt.% H_2O with a median of 3.0 wt.% H_2O. The O 778-nm normalization predicts a median value of 2.3 wt.% H_2O with the middle 50% ranging from 1.3 to 3.3 wt.% H_2O. These values are consistent with the total oxide percentages derived from ChemCam,

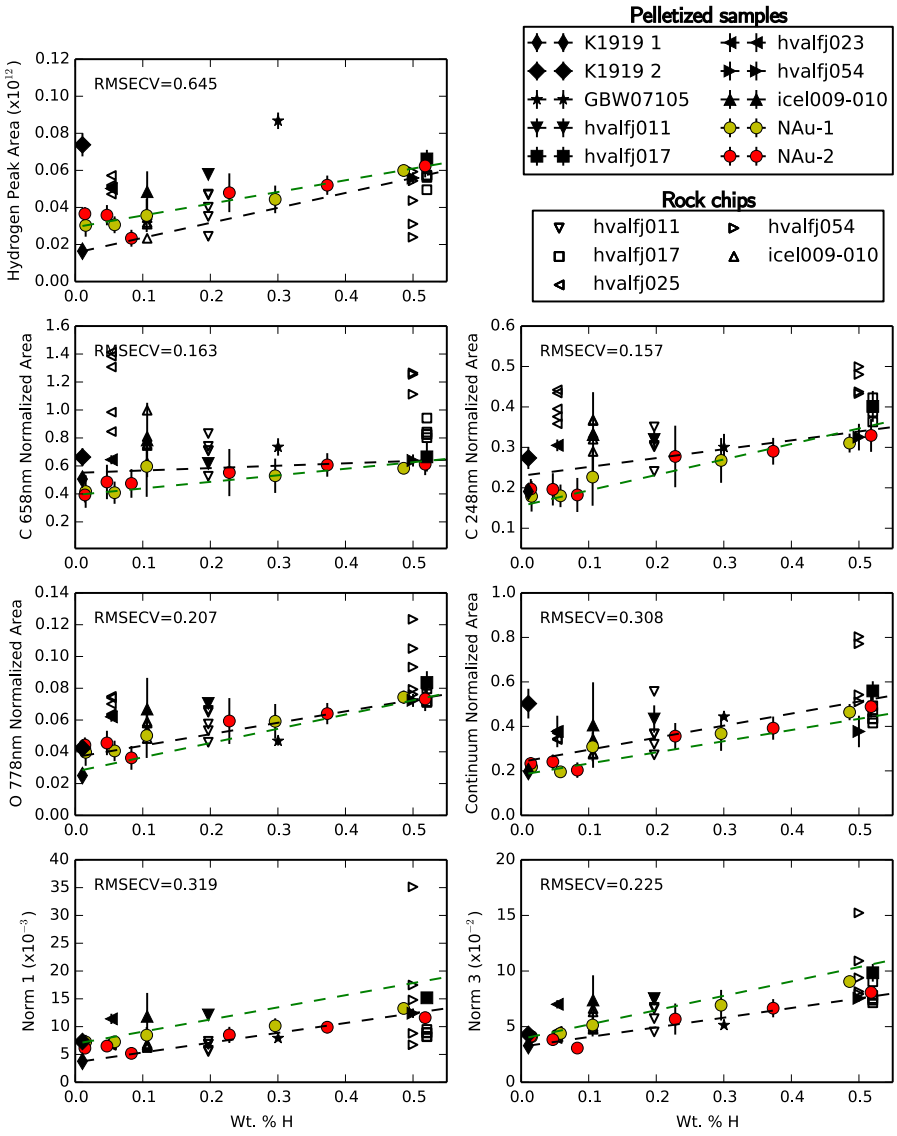

Figure 11. Hydrogen emission peak area versus weight percent hydrogen (calculated from temperatures >150 °C) for the basalt samples and the nontronite mixtures. Rock chip measurements are shown with open symbols, and pelletized samples are shown with solid symbols. A linear fit to the solid points (pelletized samples and nontronite mixtures) is shown here in black with RMSECV. The green dashed line is the best linear fit to all the samples in Figure 5 for comparison. The x axis error bars are >0.2 wt.% H and were removed for clarity. Trend line coefficients are included in Table A1. RMSECV = root-mean-square error cross-validation.

which have a median of 97.0 wt.% for the bedrock points we considered. When we take the weight percent H_2O calculated from our calibrations and add it to the ChemCam derived total oxide percentage, we get a median total of 99.6 wt.% for the O 778-nm calibration and 100.2 wt.% for the C 248-nm calibration. Some low water content samples (8 with the C 248-nm normalization and 17 with the O 778-nm normalization) plot with less than 0 wt.% H_2O because our laboratory calibration did not require the y intercept to be 0. A small number of high outliers include individual points predicting up to 25% H_2O, which may target high H compositions.

4. Discussion

4.1 Normalized H Peak Area Calibration Curves

The use of H calibration standards that do not lose water under vacuum was key in our study (see Figure 4 versus Figure 5). By using our TGA measurements to correct the weight percent H to account for the loss of nonstructural H_2O in the vacuum chamber before LIBS measurement, we correct for some of the scatter due to uncertainty in sample water retention. This highlights the importance of stability of H for future investigators of H emission line calibration. Future studies might consider producing glasses of controlled OH contents or including a balance within the vacuum chamber to monitor the sample directly.

All normalizations show similar behavior—a monotonic increase of H peak area with increasing sample H weight percent—and perform better than nonnormalized H peak area, evaluated by computed RMSECV (Figure 5). The continuum, C 248-nm, and O 778-nm normalizations produce the lowest RMSECV values for the three fit trends (Figures 5), similar to the results of Rapin et al. (2017a) who preferred C 248 nm. C 658 nm also has scatter that is nearly as low but is likely complicated by the interference from the H peak of interest, while whole spectra Norm 1 and Norm 3 may be affected by variation in sample composition causing variation in line area unrelated to anything affecting or proportional to the H signal.

We favor normalization to C 248 nm and O 778 nm due to the shot profile behavior of these peaks. As discussed in section 3.3, these individual peaks decrease in intensity with shot number like the H peak. The continuum intensity and single or total detector intensity (Anderson et al., 2017) increase with shot number or are simply variable, which can increase variation of the hydrogen signal after normalization (as also shown by Rapin et al., 2017a). While the O 778-nm peak is caused both by breakdown of atmospheric CO_2 and the sample bulk O content, O 778-nm normalization is not greatly biased by changes in the sample O content because the majority of variation in the O 778-nm peak is due to variations in the measurement conditions such the atmospheric constituents and pressure (Gasnault et al., 2012). In addition, O 778 nm is another neutral emission line with similar excitation energy to H (H Ek = 10.2 eV; O Ek = 10.7 eV). The similar excitation energies could make this normalization less sensitive to matrix effects (Lazic & De Ninno, 2017). For this reason and from the experimental results in Figure 12 with samples acquired under different experimental conditions, the O 778-nm normalization may be the simplest to produce quality results.

Normalization to C 248 nm was slightly favored in the results of Rapin et al. (2017a). One reason for the slight difference from this study may result from the three different instruments located on Mars, in Toulouse, and at LANL. The latter instrument was used for this study, and it consists of an EM mast unit with a newly built body unit. Rapin et al. (2016) and Rapin et al. (2017a) used the Toulouse instrument for their laboratory studies, and it consists of an engineering qualification model (EQM) mast unit and an EM body unit. A change to the mast unit that was made between the EM and the EQM affects the quality of the lower portion of the UV spectral range, where the C 248-nm line resides. Specifically, the LANL EM mast unit contains a laser dichroic mirror that is of inferior quality to that used in the EQM and flight model, resulting in instrument sensitivity at 248 nm that is a factor of 60% worse. This dichroic, positioned at the center of the primary mirror of the Schmidt-Cassegrain telescope, is responsible for reflecting the laser light to project it to the rest of the tele- scope and out to the target and also for transmitting the returned plasma light to the optical fiber and spectrometers (Maurice et al., 2012). This degraded UV sensitivity in the LANL instrument

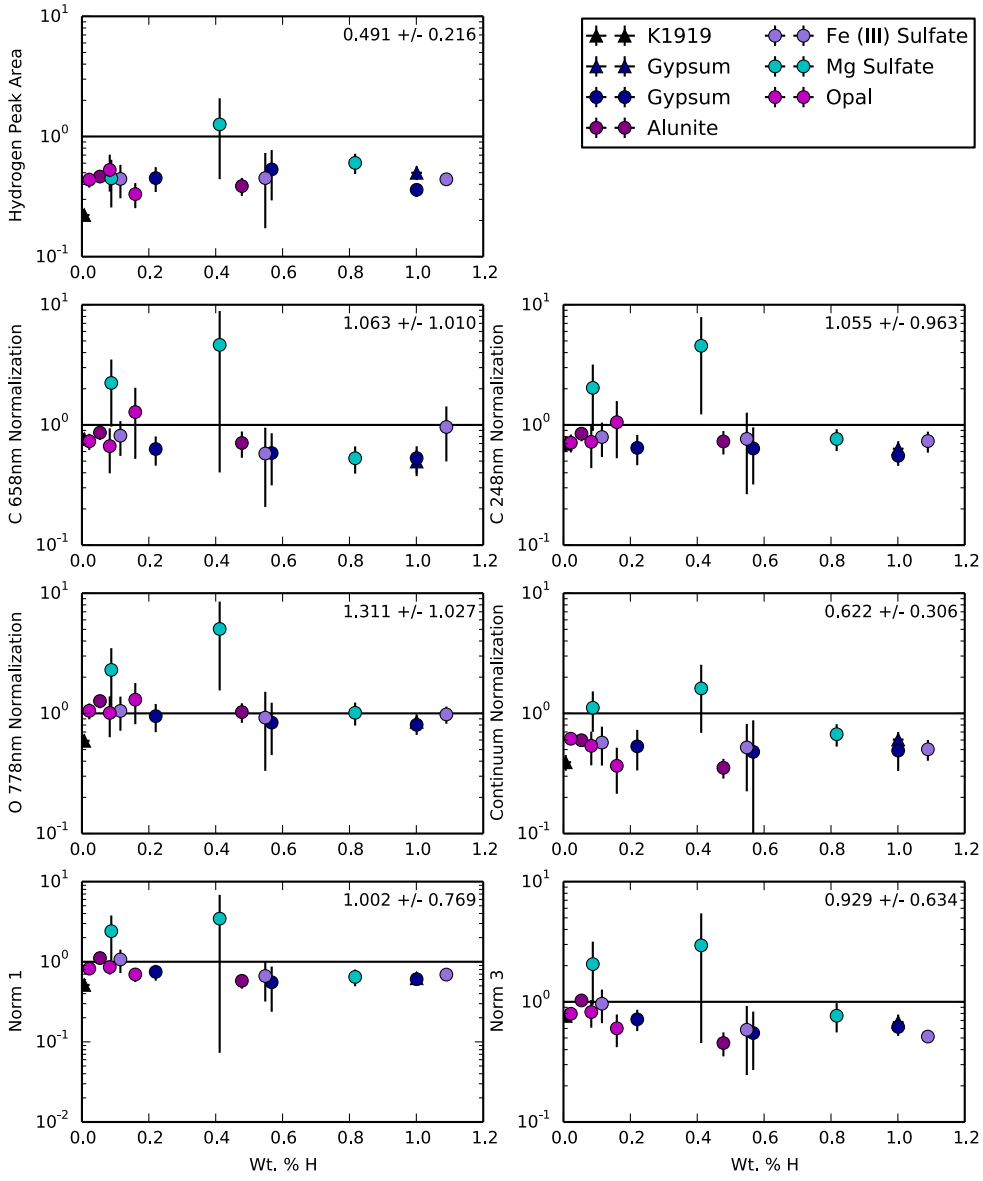

Figure 12. Ratios of peak areas taken from the same sample at different times as a function of weight percent H to show the effect of normalization on changes in experimental conditions. The triangles are the ratio of batch 1 (September 2013) laser-induced breakdown spectroscopy measurements to batch 2 (September 2014) measurements. The circles are the ratio of batch 4 (January 2017) measurements to batch 2 (September 2014) measurements. The average and standard deviation of the hydrogen values are shown in the upper right corner.

is significant enough to affect the signal-to-noise ratio at 248 nm and could explain the slight preference in our work for the 778-nm O line over the 248-nm C line for normalization.

While all normalizations provide similar results for the relatively low hydration data examined here, our work also shows that the increase in normalized LIBS H signal with weight percent H may not be linear at high weight percent H. This effect was not observed in the smaller sample set considered by Rapin et al. (2017a) which covered a similar range (0–50 wt.% H_2O) but is apparent in our data (Figure 5). A linear relationship was not an a priori assumption of our study. Emission line intensity is expected to increase proportional to the number of emitting atoms, that is, their mole fraction. We also tested whether the measured H signal increases linearly for mole fraction H by calculating based on stoichiometry the mole fraction H for three of our mixtures: brucite and K1919, gypsum and K1919, and gypsum and GBW07105, using the independent lab-derived chemistry of the basaltic endmembers (Figure A2). The gypsum points are complicated by probable water loss during chamber pump down (see section 3.2), but the brucite, even considered alone, markedly departs from linearity as a function of mole fraction H too. Some of the other nonlinear trends seen in Figure 4, like those for Fe sulfate, could be accounted for by the influence of the adjacent Fe peak, which may not fully be accounted for in peak fitting. On the other hand, alunite and Mg sulfate (and Fe sulfate) also show a nonlinear increase with weight percent, in a way that would only be accentuated if our estimates for their H content are overestimates (due to loss during chamber pump down). Our hypothesis is that the nonlinearities at high H contents are due to chemical matrix effects because the addition of the hydrated material at high levels changes the average makeup of the sample. Nonlinearity could affect our ability to predict weight percent H for very hydrated ChemCam (or SuperCam) targets on Mars. This is an important regime that requires further study, including more high H samples to extend and improve the calibration at >~1.25 wt.% H or >~11 wt.% H_2O. Multivariate methods may be required.

Finally, our study highlights two additional factors that affect H peak calibration curves but are not yet completely understood. First, the range of shot numbers used will very clearly

affect the calibration curve (Figure 7). The higher the shot number, the shallower the calibration curve. This may be due to dehydration of the sample by the laser or due to simple cavity effects (Rapin et al., 2017b). Regardless, the implication for Martian data is clear: Calibration curves should only be used for the same shot number range they were initially determined with. Second, the distance to the target impacts the observed H signal. Normalizations to O 778 nm and C 248 nm best correct for distance and other differences in experimental conditions as seen in Figure 4 where the 100% gypsum samples plot closest together and in Figure 12, which shows the ratio of the LIBS H values for the same samples measured at different distances and in different batches. But there is scatter in all normalizations for distance that indicate the effect of distance to target too could benefit from further laboratory analysis.

4.2 Physical Matrix Effects and Pellets Versus Natural Rocks

Rapin et al. (2017a) considered pressed pellets of lab mixtures, and here we also include natural samples, including rock chips to observe some of the complicating physical matrix effects and the challenges associated with measuring changes in LIBS H emission. Changes in grain size, cohesion, and sample rough- ness impact the shape of the H peak and the strength of H emission (Rauschenbach et al., 2008). Schröder et al. (2015) and Meslin et al. (2013) describe ChemCam measurements showing generally higher H emission from unconsolidated soil targets than from rock targets, which can be interpreted as a result of physical matrix effects. Figure 10 shows our comparison of rock chip and pressed pellet spectra for four of the Iceland samples. Both samples are fine grained, hard, coherent. Some variation in H peak height can be explained by obvious contributions from individual hydrated grains, such as the zeolite inclusions targeted in the hvalfj054 sample. However, peak shape also changes for pressed pellet versus natural rock for all samples, including the relatively homogeneous samples like icel009 and hvalfj017 (Figure 10). The pressed pellet spectra have H peaks with smaller FWHM than the rock chip spectra. The other peaks like the C peak at 658 nm do not change shape with pellet versus rock. It is difficult to understand the cause of the larger FWHM for the rock chip samples as they have both more cohesion

and larger sample roughness than the pressed pellets. The differences in FWHM are possibly caused by the documented Stark Effect for H (Kandel, 2009), which causes broadening of spectral lines.

The H calibration we have developed using the subset of pressed pellet mixtures (Figure 5, shown in green in Figure 11) mostly works for the natural pressed pellet samples and natural rock sample chips after normalization. The normalizations that performed well for the pelletized mixtures, normalization to C 248 nm, O 778 nm, and the continuum, also perform well for the pelletized natural samples. These normalizations bring the signal levels for the pelletized natural samples to levels comparable to the pelletized nontronite-basalt mixtures of similar water content. In these cases, the pelletized natural samples (shown with solid symbols) fall very close to the previous calibration trends shown in green, and the trend fit to the samples shown in Figure 11 is very similar. The rock chips (shown with open symbols) have higher variance in the measured LIBS H peak area because the targets are no longer homogenous at the LIBS spot scale of ~350 μm. Generally, we see an increasing trend in H peak area with weight percent H measured by TGA for all the rock chip samples for all normalizations (Figure 11). The normalizations that produce the most similar linear trends to the mixture pressed pellets again are the C 248-nm, O 778-nm, and the continuum normalizations. However, the C 658-nm normalization technique gives a normalized LIBS H signal that is the same within error for all four rock chip samples measured, suggesting that this normalization is not good for these rock chips. Collectively, the data suggest that the H content can be derived from LIBS measurements of natural samples for materials with similar matrices and physical textures. In the case of more chemically and physically homogeneous samples, like hvalfj017 and icel009-010, we expected the pellet trends to match the rock chip data more closely as we do see for the O 778-nm and C 248-nm normalizations within the uncertainties described in section 3.2. The shape differences in the H emission line and differences in derived H peak for pellet versus natural rock for the more heterogeneous natural samples suggest future work on rocks is needed to fully characterize texture or physical matrix effects.

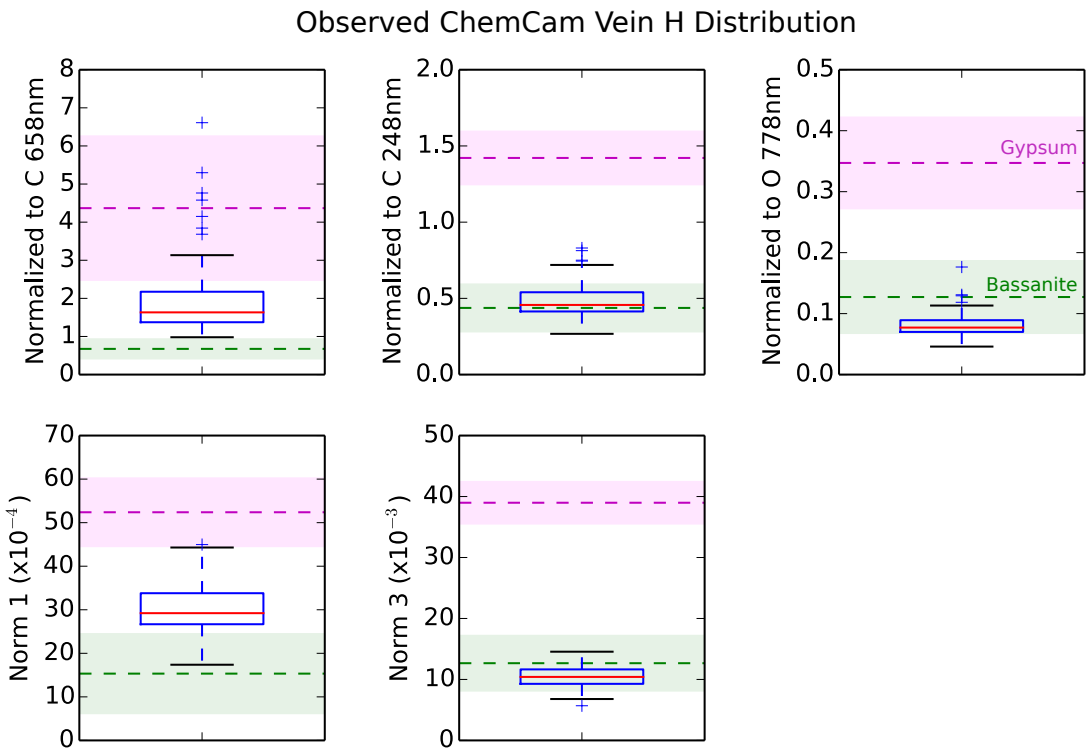

Figure 13. Boxplot of normalized H signal observed for ChemCam Ca sulfate vein points up to sol 1248. For comparison, we show the Figure 5 low range linear model predicted normalized H values for bassanite (6.2 wt.% H_2O, green) and polynomial model predicted values for gypsum (20.9 wt.% H_2O, magenta). The uncertainties, calculated using root-mean-square error as described in section 3.2, are represented as the shaded regions. The box extends from the lower to upper quartile values of the data, with a line at the median. The whiskers extend from the box to show the range of the data. Outlier points are defined as above or below 1.5 times the interquartile range from the median.

4.3 Application to ChemCam and Future Applications

The ultimate goal of this work is to enable better ChemCam measurements of H on the Martian surface. Outside of Rapin et al. (2017a), other previous works such as Schröder et al. (2015) only present the detection of H and qualitative assessments of the amount of H

present. Our application of the presented methods to ChemCam measurements of bedrock and Ca sulfate veins is only the second quantitative assessment of H using ChemCam and a first step showing the degree of uncertainty involved in applying this technique to identify specific mineral phases. As described in section 3.2, the amount of scatter in our laboratory data from the fit linear trend can be used to predict our level of certainty in ChemCam measurements.

Analysis of the sulfate veins in the Mars ChemCam data show that the choice of normalization does not change the phase we identify when distinguishing mineral hydration state when the phases are relatively pure in veins (Figure 13). The

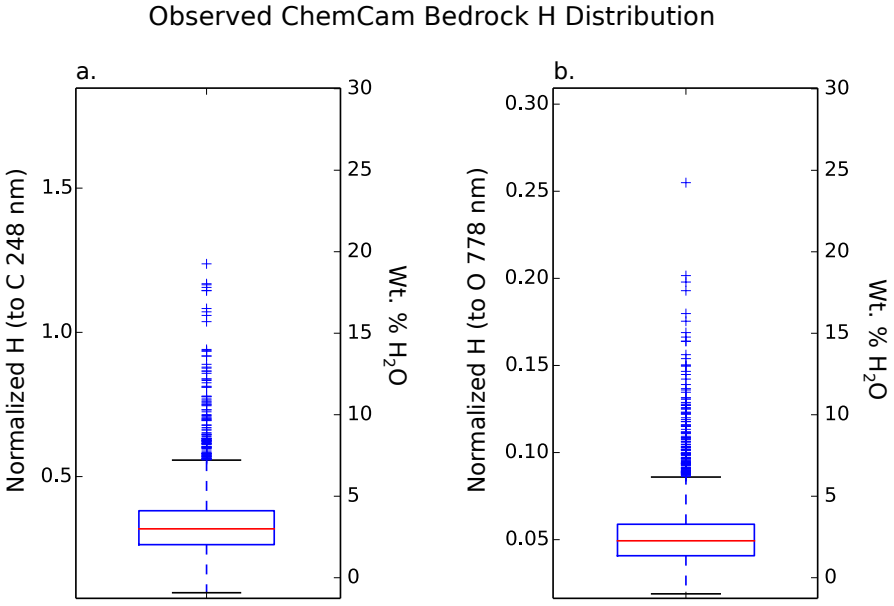

Figure 14. Boxplots of (a) C 248-nm and (b) O 778-nm normalized H signal observed for ChemCam Murray bedrock points (soils, veins, and clearly diagenetic textures removed) measured sols 766–1815. The box extends from the lower to upper quartile values of the data, with a line at the median. The whiskers extend from the box to show the range of the data. Outlier points are defined as above or below 1.5 times the interquartile range from the median.

interpretation of bassanite (versus gypsum) is robust in all normalizations. The few weight percent H_2O variability in the Martian data from different veins is comparable to the weight percent differences when applying different calibrations from the lab to Mars data. Direct comparison of sample hydration across targets with similar surface properties (cohesion, surface roughness, and grain size) is possible with normalization. For this reason, we compare the H values observed for homogeneous, smooth Murray bedrock targets and show most observation points have small amounts of water, <7.0 wt.% H_2O (Figure 14), comparable to the altered Icelandic basalts. The absolute water content of a rock is slightly affected by the choice of the normalization method (Figure 14), with the mean value for Murray bedrock ranging from 2.3 to 3.0 wt.% H_2O depending on the normalization method used. These ranges are similar to measurements by the SAM instrument of several drilled samples (0.9 ± 0.3 to 2.5 ± 1.6 wt.% H_2O; Sutter et al., 2017) and measurements of the drier top layer by the DAN instrument (0.5 to 2.0 wt.% WEH; Mitrofanov & Litvak, 2015). The high outlier points are isolated occurrences of high weight percent H_2O in visibly unaltered Murray bedrock, which could represent mixing with hydrated Ca sulfate or phyllosilicates phases. Overall, these data indicate that the water content of samples can be successfully estimated using normalized univariate analyses of H peak area in ChemCam data.

Ultimately, this laboratory study better informs both future ChemCam studies of hydration as well as future SuperCam studies. The SuperCam instrument, part of the Mars 2020 mission, will have improved spectral resolution in the VNIR range, which will aid in distinguishing the H and C 658-nm emission lines as well as the Fe 654.8-nm and 659.4-nm lines. SuperCam's temporally gated intensifier will also aid in distinguishing between peaks as well as boosting signal, and its infrared spectroscopy and Raman subsystem will also help to decipher the possible contributors to the LIBS H signal (Wiens et al., 2017).

5. Conclusions

This study builds upon previous work by Rapin et al. (2017a) and others by measuring a wider variety of H-bearing materials, important for characterizing chemical and physical matrix effects and evaluating different normalizations for H determination on Mars. We

prepared a sample set including both mixtures of minerals with known, systematic variation in hydrated mineral content and compositionally well- characterized altered volcanic rocks. TGA measurements allowed us to independently measure sample hydration. We find that:

- Loss of sample water during chamber pump down to low pressure is a significant experimental effect that must be accounted for in any study involving hydrated/hydroxylated materials under Mars temperatures and pressures. It was successfully mitigated here by considering only water lost at temperatures >150 °C and by emphasizing analyses of hydroxylated species, which are more stable, when constructing calibration curves with LIBS hydrogen peak area and weight percent H.

- Emission from H (I) 656.5 nm increases monotonically with both weight percent and mole fraction H for all the prepared mixtures except for opal and the natural altered basalts, where there is variance at low H weight percent.

- The H peak area increases linearly with weight percent H in the laboratory mixtures with structurally bound H for weight percent H up to about 1.25 wt.% H and then steepens for higher H-content samples, a potential nonlinear trend not noted by previous studies but important for correct characterization of high water content materials on Mars.

- The uncertainty in our ability to predict weight percent H from the LIBS H signal using the fit lines for the O 778-nm and C 248-nm normalizations ranged between ±0.18 and 0.43 wt.% H. We calculate and observe visually a limit of detection of 0.4–0.9 wt.% H_2O for the C 248-nm and O 778-nm normalizations.

- Normalization to C 248 nm and O 778 nm are favored because they have lowest RMSECV trends and best correct for distance and other experimental effects in the laboratory data. C (I) 248 nm was favored by Rapin et al. (2017a); we slightly prefer

normalization to O (I) 778 nm because it is a neutral emission line on the same (VNIR) detector as H. When applied to ChemCam data on Mars both perform similarly and predict and variation in results depending on normalization method used is typically <0.1 wt.% H.

- Comparison of sample hydration across different physical matrices is challenging because sample properties like surface roughness, cohesion, and grain size impact LIBS measurements of H. The natural samples we measured as both rock chips and pressed pellets document the effects of physical matrix on H emission, especially on the H peak shape even though these samples are all hard, coherent, and fine grained. While the pelletized samples have H emission comparable to the measured nontronite samples, the rock chips show considerable, nonsystematic scatter relative to the best linear fit from our mixtures that is not obviously solely due to compositional variation. Future work is needed to characterize these physical matrix effects for natural rocks.

These results are applicable to both MSL ChemCam and the Mars 2020 SuperCam instrument. While quantitative measurements of H in Martian samples are challenging due to matrix effects, qualitative comparison of H across targets with similar surface properties is possible and provides reasonable estimates of the weight percent H_2O in the Martian bedrock independently measured by the SAM and DAN instruments. This allows us to track changes in bedrock hydration throughout Curiosity's traverse.

Appendix

Additional information supporting the main text is provided here. Spectra of samples with low wt. % H showing the detection limit are included in Figure A1. The effect of using mol fraction H versus wt. % H on the linearity of normalized calibration curves is shown in Figure A2. Figure A3 shows the normalization quantities, or denominators, used in Figure 4. The fit coefficients for the linear and polynomial trend lines shown in Figures 4, 5, and 12 are included in Table A1.

		Linear (all)		Linear (<1.25 wt. % H)		Polynomial		
	Normalization	a	b	a	b	a	b	c
Fig. 4	Hydrogen Peak Area	3.73E+10	1.59E+10	4.37E+10	1.58E+10	4.89E+10	1.04E+10	4.02E+10
	C 658 nm Normalization	7.20E-01	4.15E-01	5.36E-01	4.35E-01	6.30E-01	1.26E-01	4.59E-01
	C 248 nm Normalization	3.68E-01	1.79E-01	2.49E-01	1.91E-01	1.56E-01	1.31E-01	1.99E-01
	O 778 nm Normalization	7.48E-02	3.03E-02	5.87E-02	3.15E-02	3.49E-02	3.58E-02	3.27E-02
	Norm 1	6.00E-04	3.69E-04	7.47E-04	3.67E-04	2.75E-04	8.25E-04	5.31E-04
	Norm 3	4.32E-03	3.23E-03	1.09E-02	2.80E-03	3.34E-03	1.20E-03	3.80E-03
	Continuum Normalization	5.70E-01	1.90E-01	6.77E-01	1.84E-01	-3.57E-03	5.78E-01	1.89E-01
Fig. 5	Hydrogen Peak Area	1.47E+11	2.80E+10	8.65E+10	2.90E+10	3.01E+10	4.35E+10	2.36E+10
	C 658 nm Normalization	8.62E-01	3.67E-01	6.14E-01	3.88E-01	6.16E-01	2.48E-01	4.08E-01
	C 248 nm Normalization	5.05E-01	1.49E-01	3.06E-01	1.65E-01	1.32E-01	2.25E-01	1.70E-01
	O 778 nm Normalization	1.23E-01	2.58E-02	8.36E-02	2.82E-02	2.85E-02	6.91E-02	2.88E-02
	Norm 1	2.57E-03	6.85E-04	1.04E-03	7.09E-04	5.06E-04	8.14E-04	5.59E-04
	Norm 3	1.96E-02	3.79E-03	9.56E-03	3.94E-03	3.91E-03	6.03E-03	3.45E-03
	Continuum Normalization	5.44E-01	1.80E-01	4.48E-01	1.86E-01	3.74E-02	4.43E-01	1.86E-01
Fig. 12	Hydrogen Peak Area	8.07E+10	1.55E+10					
	C 658 nm Normalization	1.71E-01	5.50E-01					
	C 248 nm Normalization	2.19E-01	2.30E-01					
	O 778 nm Normalization	7.20E-02	3.67E-02					
	Norm 1	1.77E-03	3.58E-04					
	Norm 3	8.70E-03	3.19E-03					
	Continuum Normalization	5.43E-01	2.40E-01					

Table A1. Coefficients for the Linear (ax + b) and Polynomial (ax^2 + bx + c) trend lines shown in Figures 4, 5, and 12.

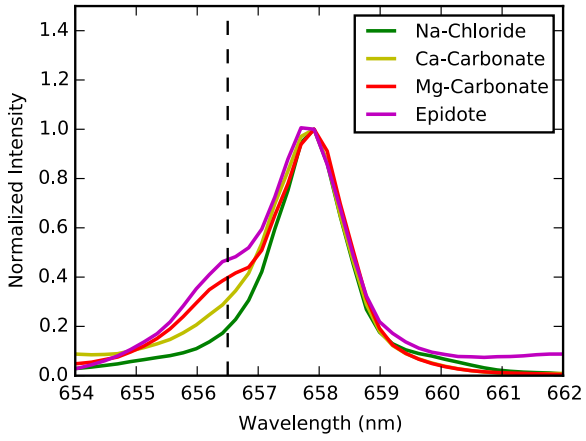

Figure A1. Comparison of samples with low measured weight percent H for determination of the H peak detection limit including Na chloride (0 wt.% H), Ca carbonate (0.01 wt.% H). Mg carbonate (0.1 wt.% H), and epidote (0.09 wt.% H).

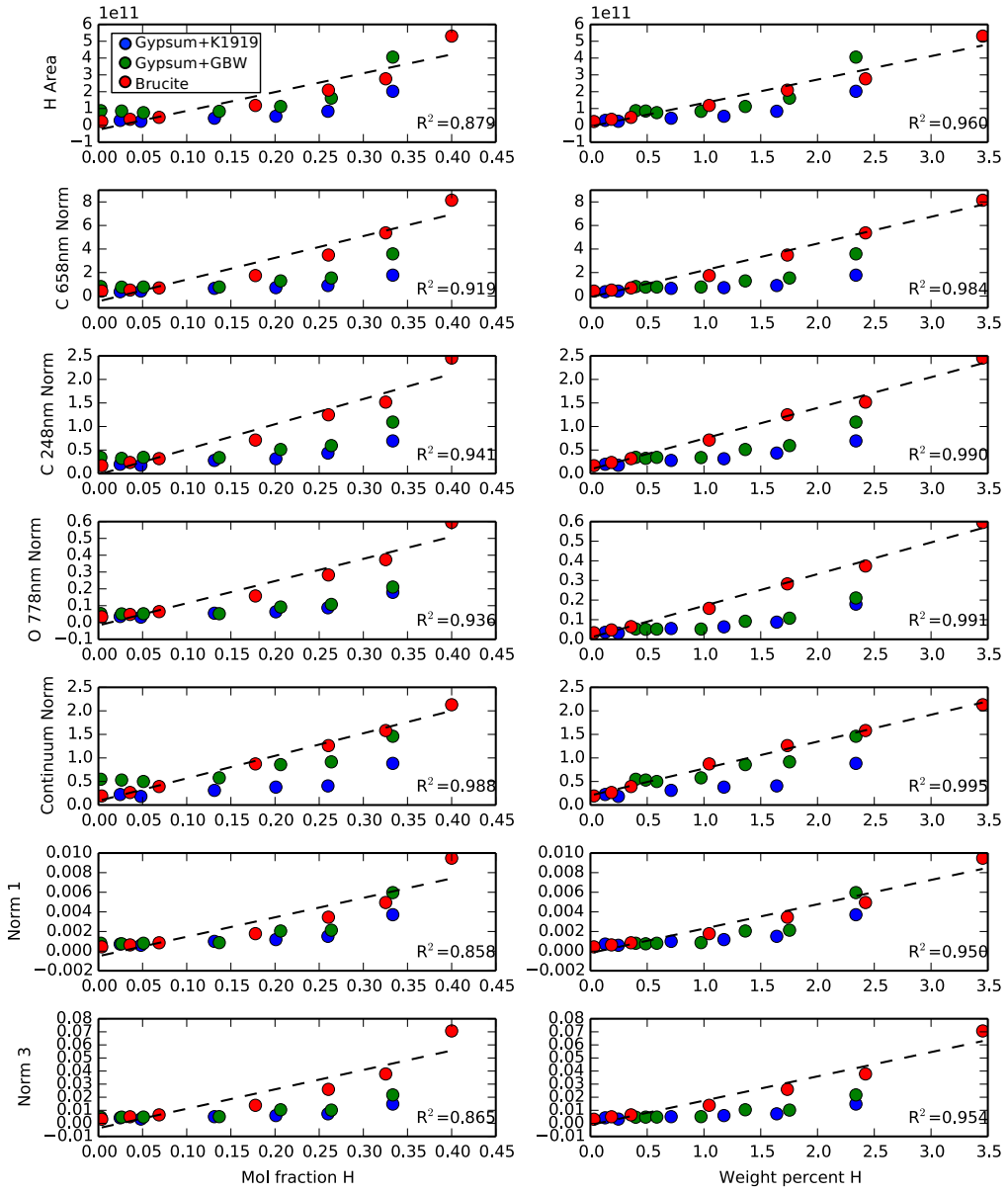

Figure A2. Calculated H peak area, unnormalized and for all normalization methods, shown as a function of (a) the theoretical mole fraction H (calculated from mineral stoichiometry) or (b) the actual measured weight percent H from thermogravimetric analysis. The best linear fit to the brucite mixture is shown with a black dashed line along with the R^2 value.

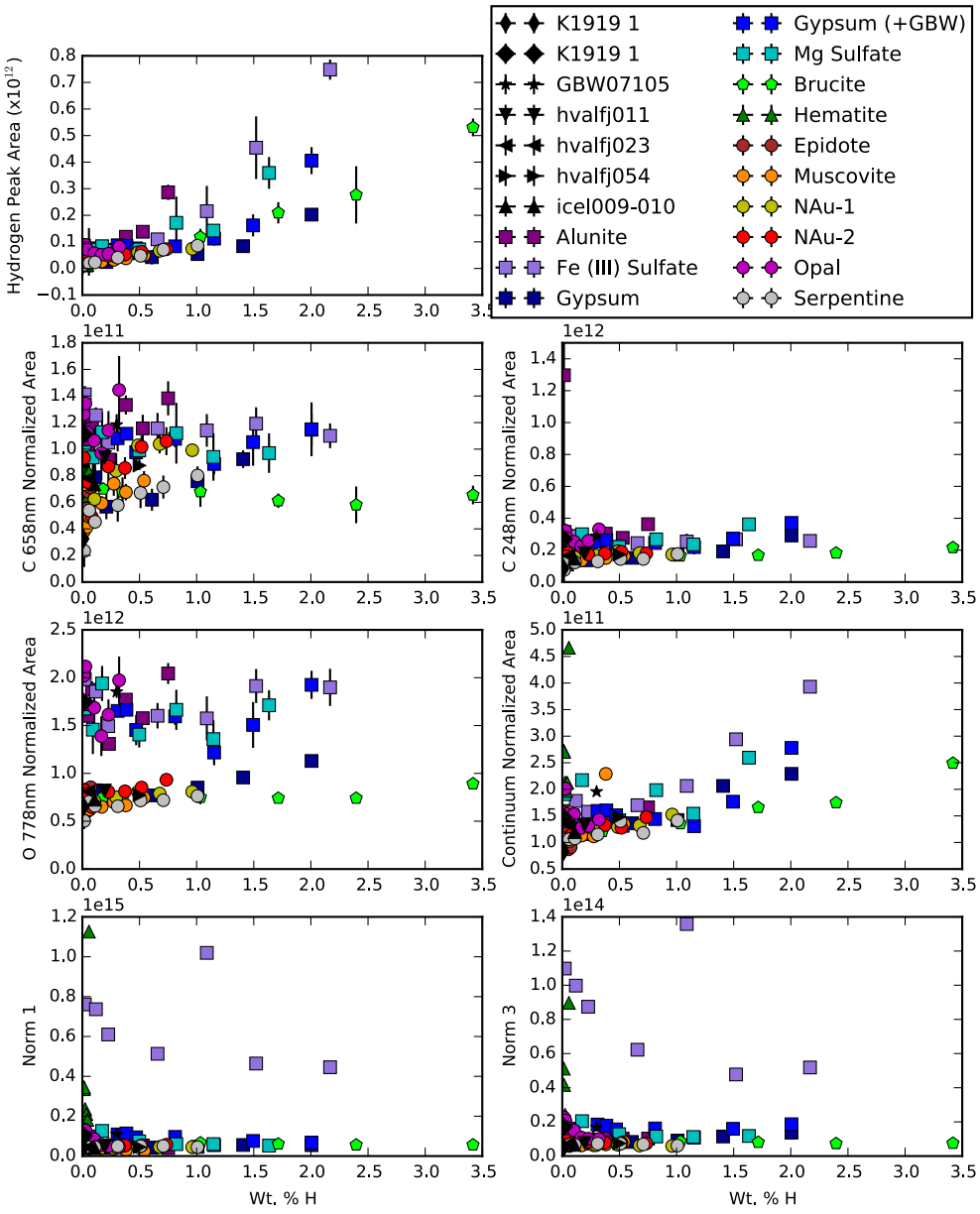

Figure A3. Hydrogen emission peak area versus weight percent H as shown in Table 2 for all samples. For all normalizations in Figure 4, we plot the denominator values that represent the value we are normalizing the first plot by.

References

Anderson, D. E., Ehlmann, B. L., Forni, O., Clegg, S. M., Cousin, A., Thomas, N. H., et al. (2017). Characterization of LIBS emission lines for the identification of chlorides, carbonates, and sulfates in salt/basalt mixtures for the application to MSL ChemCam data. Journal of Geophysical Research: Planets, 122, 744–770. https://doi.org/10.1002/2016JE005164

Blake, D., Vaniman, D., Achilles, C., Anderson, R., Bish, D., Bristow, T., et al. (2012). Characterization and calibration of the CheMin mineralogical instrument on Mars Science Laboratory. Space Science Reviews, 170(1–4), 341–399. https://doi.org/10.1007/s11214-012-9905-1

Campbell, J. L., Perrett, G. M., Gellert, R., Andrushenko, S. M., Boyd, N. I., Maxwell, J. A., et al. (2012). Calibration of the Mars Science Laboratory Alpha Particle X-ray Spectrometer. Space Science Reviews, 170(1–4), 319–340. https://doi.org/10.1007/s11214-012-9873-5

Clegg, S. M., Sklute, E., Dyar, M. D., Barefield, J. E., & Wiens, R. C. (2009). Multivariate analysis of remote laser-induced breakdown spectroscopy spectra using partial least squares, principal component analysis, and related techniques. Spectrochimica Acta Part B: Atomic Spectroscopy, 64(1), 79–88. https://doi.org/10.1016/j.sab.2008.10.045

Clegg, S. M., Wiens, R. C., Anderson, R., Forni, O., Frydenvang, J., Lasue, J., et al. (2017). Recalibration of the Mars Science Laboratory ChemCam instrument with an expanded geochemical database. Spectrochimica Acta Part B: Atomic Spectroscopy, 129, 64–85. https://doi.org/ 10.1016/j.sab.2016.12.003

Ding, Z., & Frost, R. L. (2002). Controlled rate thermal analysis of nontronite. Thermochimica Acta, 389(1-2), 185–193. https://doi.org/10.1016/ S0040-6031(02)0059-X

Ehlmann, B. L., Bish, D. L., Ruff, S. W., & Mustard, J. F. (2012). Mineralogy and chemistry of altered Icelandic basalts: Application to clay mineral detection and understanding aqueous environments on Mars. Journal of Geophysical Research, 117, E00J16. https://doi.org/10.1029/ 2012JE004156

Ehlmann, B. L., & Edwards, C. S. (2014). Mineralogy of the Martian surface. Annual Review of Earth and Planetary Sciences, 42(1), 291–315. https://doi.org/10.1146/annurev-earth-060313-055024

Földvári, M. (2011). Handbook of thermogravimetric system of minerals and its use in geological practice (p. 213). Budapest: Occasional Papers of the Geological Institute of Hungary.

Gasnault, O., Mazoyer, J., Cousin, A., Meslin, P.-Y., Lasue, J., Lacour, J. L., et al. (2012). Deciphering sample and atmospheric oxygen contents with ChemCam on Mars. In Lunar and Planetary Science Conference (p. 2888). https://doi.org/10.1007/ s00216-011-4747-3.

Hadnott, B. A., Ehlmann, B. L., & Jolliff, B. L. (2017). Mineralogy and chemistry of San Carlos high-alkali basalts: Analyses of alteration with application for Mars exploration. American Mineralogist, 102(2), 284–301. https://doi.org/10.2138/am-2017-5608

Kandel, Y. P. (2009). An experimental study of H Balmer Lines in pulsed laser plasma. Middletown, CT: Wesleyan University.

Keeling, J. L., Raven, M. D., & Gates, W. P. (2000). Geology and Characterization of Two Hydrothermal Nontronites from Weathered Metamorphic Rocks at the Uley Graphite Mine, South Australia. Clays and Clay Minerals, 48(5), 537–548. https://doi.og/10.1346/ CCMN.2000.0480506

Kurniawan, K. H., Tjia, M. O., & Kagawa, K. (2014). Review of laser-induced plasma, its mechanism, and application to quantitative analysis of hydrogen and deuterium. Applied Spectroscopy Reviews, 49(5), 323–434. https://doi.org/10.1080/05704928.2013.825267

Lazic, V., & De Ninno, A. (2017). Calibration approach for extremely variable laser induced plasmas and a strategy to reduce the matrix effects n general. Spectrochimica Acta Part B: Atomic Spectroscopy, 137, 28–38. https://doi.org/10.1016/jsab.2017.09.001

Mahaffy, P. R., Webster, C. R., Cabane, M., Conrad, P. G., Coll, P., Atreya, S. K., et al. (2012). The sample analysis at Mars investigation and instrument suite. Space Science Reviews, 170(1–4), 401–478. https://doi.org/10.1007/s11214-012-9879-z

Maurice, S., Clegg, S. M., Wiens, R. C., Gasnault, O., Rapin, W., Forni, O., et al. (2016). ChemCam activities and discoveries during the nominal mission of the Mars Science Laboratory in Gale crater, Mars. Journal of Analytical Atomic Spectrometry, 31(4), 863–889. https://doi.org/ 10.1039/C5JA00417A

Maurice, S., Wiens, R. C., Saccoccio, M., Barraclough, B., Gasnault, O., Forni, O., et al. (2012). The ChemCam instrument suite on the Mars Science Laboratory (MSL) rover: Science objectives and mast unit description. Space Science Reviews, 170(1–4), 95–166. https://doi.org/ 10.1007/s11214-012-9912-2

Meslin, P.-Y., Gasnault, O., Forni, O., Schröder, S., Cousin, A., Berger, G., et al. (2013). Soil diversity and hydration as observed by ChemCam at Gale crater, Mars. Science, 341(6153), 1,238670–1,238,670. https://doi.org/10.1126/science.1238670

Milliken, R. E., & Mustard, J. F. (2005). Quantifying absolute water content of minerals using near-infrared reflectance spectroscopy. Journal of Geophysical Research, 110, E12001. https://doi.org/10.1029/2005JE002534

Mitrofanov, I. G. and Litvak, M. L. (2015). Water and chlorine abundance along the traverse of curiosity according to DAN measurements. In Lunar and Planetary Science Conference (p. 1423).

Mitrofanov, I. G., Litvak, M. L., Varenikov, A. B., Barmakov, Y. N., Behar, A., Bobrovnitsky, Y. I., et al. (2012). Dynamic Albedo of Neutrons (DAN) experiment onboard NASA's Mars Science Laboratory. Space Science Reviews, 170(1–4), 559–582. https://doi.org/10.1007/s11214-012- 9924-y

Morris, R. V., Vaniman, D. T., Blake, D. F., Gellert, R., Chipera, S. J., Rampe, E. B., et al. (2016). Silicic volcanism on Mars evidenced by tridymite in high-SiO2 sedimentary rock at Gale crater. Proceedings of the National Academy of Sciences, 113(26), 7071–7076. https://doi.org/10.1073/ pnas.1607098113

Nachon, M., Clegg, S. M., Mangold, N., Schröder, S., Kah, L. C., Dromart, G., et al. (2014). Calcium sulfate veins characterized by ChemCam/Curiosity at Gale crater, Mars. Journal of Geophysical Research: Planets, 119, 1991–2016. https://doi.org/10.1002/2013JE004588

Rampe, E. B., Ming, D. W., Blake, D. F., Bristow, T. F., Chipera, S. J., Grotzinger, J. P., et al. (2017). Mineralogy of an ancient lacustrine mudstone succession from the Murray formation, Gale crater, Mars. Earth and Planetary Science Letters, 471, 172–185. https://doi.org/10.1016/j.epsl.2017.04.021

Rapin, W., Meslin, P.-Y., Maurice, S., Vaniman, D., Nachon, M., Mangold, N., et al. (2016). Hydration state of calcium sulfates in Gale crater, Mars: Identification of bassanite veins. Earth and Planetary Science Letters, 452, 197–205. https://doi.org/10.1016/j.epsl.2016.07.045

Rapin, W., Meslin, P.-Y., Maurice, S., Wiens, R. C., Laporte, D., Chauviré, B., et al. (2017a). Quantification of water content by laser induced breakdown spectroscopy on

Mars. Spectrochimica Acta Part B: Atomic Spectroscopy, 130, 82–100. https://doi.org/10.1016/j.sab.2017.02.007

Rapin, W., Bousquet, B., Lasue, J., Meslin, P.-Y., Lacour, J.-L., Fabre, C., et al. (2017b). Roughness effects on the hydrogen signal in laser-induced breakdown spectroscopy. Spectrochimica Acta Part B: Atomic Spectroscopy, 137, 13–22. https://doi.org/10.1016/j.sab.2017.09.003

Rauschenbach, I., Lazic, V., Pavlov, S. G., Hubers, H.-W., & Jessberger, E. K. (2008). Laser induced breakdown spectroscopy on soils and rocks: Influence of the sample temperature, moisture and roughness. Spectrochimica Acta Part B: Atomic Spectroscopy, 63(10), 1205–1215.https://doi.org/10.1016/j.sab.2008.08.006

Schröder, S., Meslin, P.-Y., Cousin, A., Gasnault, O., Rapin, W., Blank, J., et al. (2014). Chemcam hydrogen detection in soils and dust along Curiosity's traverse. In 8th International Conference on Mars (P. 1214).

Schröder, S., Meslin, P.-Y., Gasnault, O., Maurice, S., Cousin, A., Wiens, R. C., et al. (2015). Hydrogen detection with ChemCam at Gale crater. Icarus, 249, 43–61. https://doi.org/10.1016/j.icarus.2014.08.029

Schröder, S., Rammelkamp, K., Vogt, D. S., Frohmann, S., Cousin, A., Gasnault, O., and Jubers, H.-W. (2018). Improving minor and trace element detection in Martian targets with time-resolved LIBS. In Lunar and Planetary Science Conference (p. 1962).

Sobron, P., Wang, A., & Sobron, F. (2012). Extraction of compositional and hydration information of sulfates from laser-induced plasma spectra recorded under Mars atmospheric conditions—Implications for ChemCam investigations on Curiosity rover. Spectrochimica Acta Part B: Atomic Spectroscopy, 68 (Supplement C), 1–16. https://doi.org/10.1016/j.sab.2012.01.002

Sutter, B., McAdam, A. C., Mahaffy, P. R., Ming, D. W., Edgett, K. S., Rampe, E. B., et al. (2017). Evolved gas analyses of sedimentary rocks and eolian sediment in Gale crater, Mars: Results of the Curiosity rover's sample analysis at Mars instrument from Yellowknife Bay to the Namib Dune. Journal of Geophysical Research: Planets, 122, 2574–2609. https://doi.org/10.1002/2016JE005225

Vaniman, D., Blake, D., Bristow, T., Marais, D. D., Achilles, C., Anderson, R., et al. (2013). Data from the Mars Science Laboratory CheMin XRD/XRF instrument. In EGU General Assembly (Vol. 15, p. 6272).

Vaniman, D. T., & Chipera, S. J. (2006). Transformations of Mg- and Ca-sulfate hydrates in Mars regolith. American Mineralogist, 91(10), 1628–1642. https://doi.org/10.2138/am.2006.2092

Wiens, R. C., Maurice, S., Barraclough, B., Saccoccio, M., Barkley, W. C., Bell, J. F., et al. (2012). The ChemCam instrument suite on the Mars Science Laboratory (MSL) rover: Body unit and combined system tests. Space Science Reviews, 170(1–4), 167–227. https://doi.org/10.1007/s11214-012-9902-4

Wiens, R. C., Maurice, S., Lasue, J., Forni, O., Anderson, R. B., Clegg, S., et al. (2013). Pre-flight calibration and initial data processing for the ChemCam laser-induced breakdown spectroscopy instrument on the Mars Science Laboratory rover. Spectrochimica Acta Part B: Atomic Spectroscopy, 82, 1–27. https://doi.org/10.1016/j.sab.2013.02.003

Wiens, R. C., Maurice, S., & Rull Perez, F. (2017). The SuperCam remote sensing instrument suite for the Mars 2020 rover mission: A preview. Spectroscopy, 32(5), 50–55.

Chapter 3

HYDROGEN VARIABILITY IN THE MURRAY FORMATION, GALE CRATER, MARS

N. H. Thomas[1], B. L. Ehlmann[1,2], W. Rapin[1], F. Rivera-Hernández[3], N. T. Stein[1], and R. C. Wiens[4]

[1] Division of Geological and Planetary Sciences, California Institute of Technology, Pasadena, California, USA.

[2] Jet Propulsion Laboratory, California Institute of Technology, Pasadena, California, USA.

[3] Dartmouth College, Hanover, NH,

[4] Los Alamos National Laboratory, Los Alamos, New Mexico, USA.

Abstract

The Murray formation, a smectite clay-bearing sequence of heterolithic mudstones and sandstones recording fluvial deltaic and lake deposits, comprises the lowest exposed strata of the 5-km tall sedimentary mound at the center of Gale crater known as Mt. Sharp. The ChemCam instrument onboard the Mars Science Laboratory (MSL) Curiosity rover has measured the chemical composition of >4500 Murray formation bedrock points, allowing statistical measurement of changes in composition with stratigraphy. Recent laboratory calibrations have improved ChemCam measurements of H, an important element for identifying syndepositional and later diagenetic water-rock interactions. Here, we report 2.3-3.1 wt. % H_2O in most Murray formation bedrock targets, similar to previous measurements using the DAN and SAM instruments. Additionally, we identify specific stratigraphic intervals with high H phases that contain opal, hydrated Mg-sulfates, Mn-enriched units, and akageneite and observe trends in the H signal with grain size. Variability in the ChemCam-observed hydrogen content of rocks points to a rich history of

water-rock interaction at Gale crater, including changes in water chemistry during Murray formation deposition and multiple later groundwater episodes.

1. Introduction

The Mars Science Laboratory (MSL) Curiosity rover is investigating the sedimentary stratigraphy of Gale crater's Mt. Sharp, which formed ~3.8-3.6 Ga ago and contains a sequence of clay-, hematite-, silica-, and sulfate-bearing units identified from orbit (Milliken et al., 2010; Fraeman et al., 2016). Mt. Sharp's lowermost strata are composed of fine-grained, thinly laminated mudstones, as well as heterolithic mudstones and sandstones, which are interpreted to record fluvial deltaic and lake deposits (Grotzinger et al., 2015; Hurowitz et al., 2017) and are collectively called the Murray formation; these are the focus of our study. Prior work has reported variation in the chemical index of alteration (CAI; Mangold et al., 2019), mineralogy (Rampe et al., 2017), and the crystal chemistry of clay minerals as the rover traversed the Murray formation. Changes in bulk hydrogen present as water or OH in basaltic sedimentary materials and specific hydrated phases aid the determination of the degree of water-rock interaction, the style of aqueous alteration of rock units, and markers of past environments.

Curiosity measures the H content of samples with four instruments: DAN, SAM, CheMin, and ChemCam. The Dynamic Albedo of Neutrons (DAN) instrument assesses hydrogen content in the near subsurface (decimeter scale) over a few meter-scale footprint beneath the rover (Mitrofanov et al., 2012). For mission sols 201-753, DAN measurements of water equivalent hydrogen (WEH) ranged from 0.0 wt. % to 15.3 wt. % (Tate et al., 2017). More recently, DAN measured on average 1.6 ± 1.1 WEH from sols 753-1292 (Tate et al., 2019). The Sample Analysis at Mars (SAM) instrument detects H_2O and H_2 released from solid samples upon heating (Mahaffy et al., 2012) and measured 0.9 ± 0.3 – 2.5 ± 1.6 wt % H_2O for the first two eolian and nine sedimentary rock samples measured by Curiosity. CheMin identified crystalline minerals that host hydrogen in their structure (Blake et al., 2012) and has quantified jarosite, gypsum, bassanite, opal, and phyllosilicate abundances (e.g.,

Rampe et al., 2017) including clay mineral abundances up to ~28 wt. % (Bristow et al., 2018).

The ChemCam instrument is sensitive to hydrogen content and characterizes sample geochemistry at submillimeter scale with a large dataset (> 19,000 locations measured to date). ChemCam has been previously used to detect hydrogen in dust, soils, and rocks in Gale crater (Meslin et al., 2013; Schröder et al., 2015). Schröder et al. (2015) made the first steps towards quantification of H with ChemCam and since then more quantitative work has been applied. After the initial detection of H in calcium sulfate veins (Nachon et al., 2014; Schröder et al., 2015), Rapin et al. (2016) determined the presence of bassanite. ChemCam studies have identified opal at Marias Pass (Rapin et al., 2018) and hydrated Mg-sulfates at Sutton Island (Rapin et al., 2019; submitted).

Here, we applied the recent improved laboratory calibrations of H by Rapin et al. (2017a) and Thomas et al. (2018) to quantify the bulk H content of the Murray formation bedrock. We searched for quantitative trends in bulk rock H with stratigraphic level, formation member, and grain size. We examined the relationship to units identified from orbit and detected with other instruments. We cataloged the specific instances of H-enriched units and identify the high-H phases present that indicate changes in depositional environment or style of diagenesis.

2. Methods

The ChemCam instrument uses Laser-Induced Breakdown Spectroscopy (LIBS) to measure the elemental composition of fine-scale (350-550 micron diameter) points < 7 m from the rover (Wiens et al., 2012; Maurice et al., 2012). While major element compositions are calculated for all points using multivariate techniques (Clegg et al., 2017; Anderson et al., 2017), volatile elements like H are detectable but difficult to quantify with this method given relatively few, weak emission lines and physical and chemical matrix effects. We apply standard ChemCam data processing techniques followed by the peak fitting and normalization techniques described in detail by Thomas et al. (2018) to report

the normalized H 656.5 nm peak area. We normalized by dividing by the O 778 nm peak area, an emission line also on the VNIR detector which has recently been shown to be less sensitive to sample matrix (Schröder et al., 2019).

To minimize the impact of physical matrix effects caused by varying surface properties, we limited our study to bedrock targets with no clear cracks or varying surface geometries which may cause artificial enhancement in the H signal from surface roughness (Rapin et al., 2017b). The first five shots were excluded from analysis due to potential dust and surface effects. We visually inspected accompanying co-located context Remote Micro-Imager (RMI) and MastCam images to classify all ChemCam data points as soil, bedrock, float rock, or diagenetic (vein or nodule).

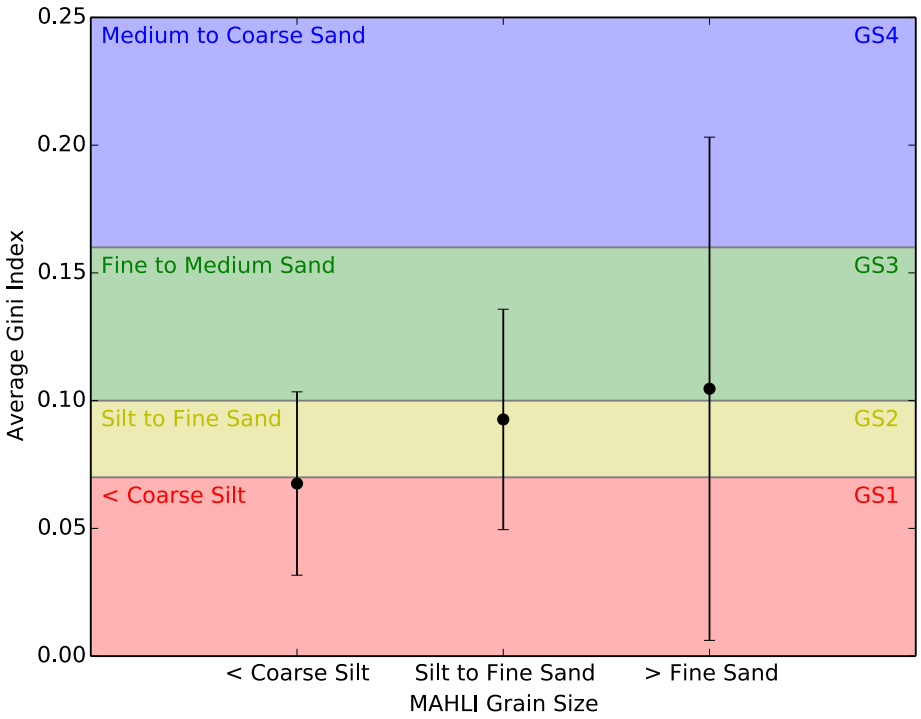

Figure 1. Comparison of MAHLI measured grain size to Gini index approximated grain size. For each MAHLI grain size category, the average Gini score is shown along with the standard deviation (error bar).

Target grain size may impact the LIBS H signal, so, for ChemCam targets up to sol 1816, we compare our measurements to the Gini index mean score, a composition-based grain-size proxy that uses point-to-point chemical variabilities in ChemCam data (Rivera-Hernández et al., 2019). Using the Gini index to approximate grain size is subject to errors inherent to the technique, such as incorrect, low Gini scores for coarse grained, homogeneous targets. We tested the accuracy of the Gini index by comparing grain size estimates made using the Gini index to measurements from MAHLI (Mars Hand Lens Imager) images for 24 targets located at the base of the Murray formation that have been studied with both methods (Figure 1). On average, the Gini index correctly predicted the MAHLI measured grain size range. There is significant variation in the Gini index mean score for coarser grained targets, likely due to differences in the techniques used, but the Gini index can be used as a rough proxy for target grain size.

3. Results

3.1 Statistics

From sol 766 to 2339 of the mission, ChemCam targeted Murray formation bedrock with 4758 observation points, or 627 targets. The median normalized H peak area observed is 0.05 (Figure 2), which corresponds to 2.2 wt. % H_2O using our laboratory calibration (Thomas et al., 2018). The middle 50% of the data, or the interquartile range, is 0.04-0.06 (2.3-3.1 wt. % H_2O). ChemCam observed 292 outlier points with normalized peak areas > 0.08 or > 5.9 wt. % H_2O, and anomalously high H signals up to 18 wt. % H_2O. 36 observation points (0.7%) have reported water contents less than 0 wt. % H_2O because our laboratory calibration did not require the y-intercept to be zero.

The median ChemCam H signal is similar, regardless of Murray formation member (Figure 2). However, the mean H signal varies significantly between some of the members of the Murray formation: Hartmann's Valley, Pettegrove Point, and Jura members (Table 1). Hartmann's Valley shows lower hydrogen (mean ± standard deviation: 1.9±1.5 wt. % H_2O), in spite of the fact it is coarser (Figure 3), which typically correlates with higher

hydrogen peaks for the same H content (Rapin et al., 2017b). The Vera Rubin ridge members of Pettegrove Point (2.2±1.5 wt. % H_2O) and Jura (2.9±2.3 wt. % H_2O) have higher hydrogen than units observed before the Vera Rubin ridge.

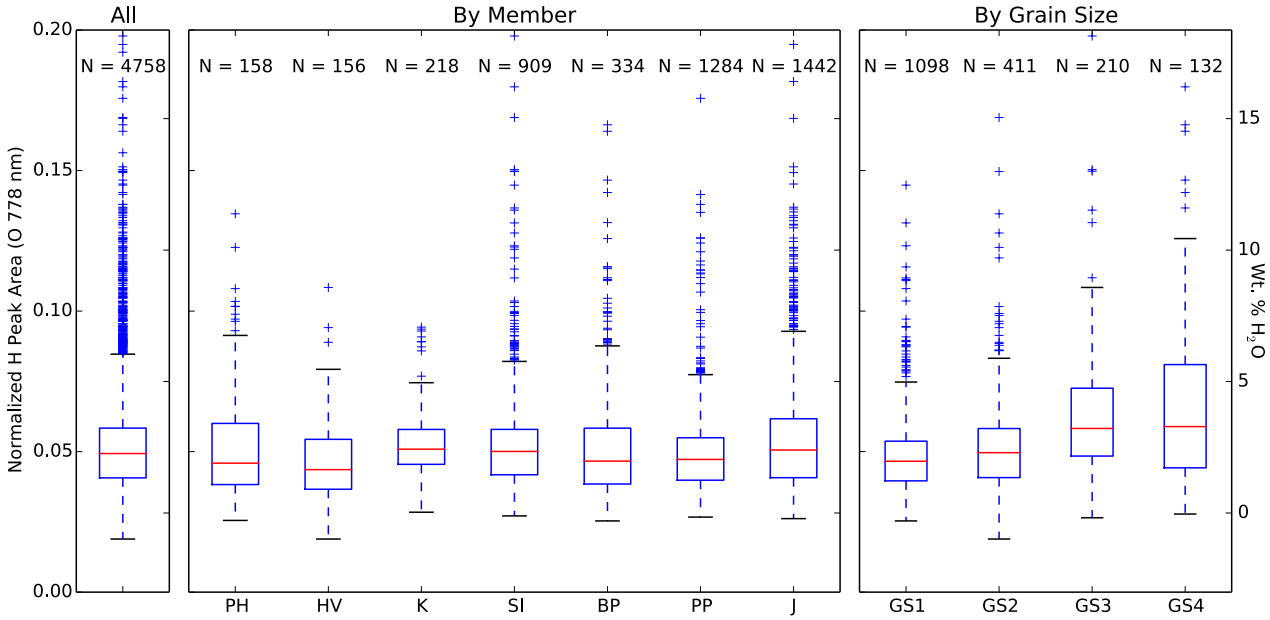

Figure 2. Boxplots showing the distribution of normalized H peak areas for (a) all Murray formation bedrock measurements, (b) each member of the Murray formation, and (c) each Gini index categorized grain size class. The members are: Pahrump Hills (PH), Hartmann's Valley (HV), Karasburg (K), Sutton Island (SI), Blunts Point (BP), Pettegrove Point (PP), and Jura (J). The grain size classes are: coarse silt and smaller (GS1), silt to fine sand (GS2), fine to medium sand (GS3), and medium to coarse sand (GS4). The box extends from the lower to upper quartile values of the data, with a line at the median. The whiskers extend from the box to show the range of the data. Outlier points are defined as above or below 1.5 times the interquartile range from the median.

	PH	HV	K	SI	BP	PP	J
PH		0.006	0.460	0.445	0.453	0.129	0.053
HV			1.12E-06	2.85E-07	3.30E-05	1.55E-02	4.48E-11
K				0.942	0.888	8.60E-06	0.035
SI					0.882	1.14E-07	0.016
BP						1.69E-03	0.179
PP							1.11E-16
J							

Table 1. A t-test was used to determine if there is a significant difference between the means of the normalized H peak areas for the different members of the Murray formation: Pahrump Hills (PH), Hartmann's Valley (HV), Karasburg (K), Sutton Island (SI), Blunts Point (BP), Pettegrove Point (PP), and Jura (J). Two-tailed p-values (testing the alternative hypothesis that $\mu_A \neq \mu_B$) are reported. P-values passing 95% confidence are highlighted.

	GS1	GS2	GS3	GS4
GS1		2.91E-05	4.44E-16	3.38E-11
GS2			8.06E-09	2.43E-07
GS3				0.2203
GS4				

Table 2. A t-test was used to determine if there is a significant difference between the means of the normalized H peak areas for the different grain size categories: coarse silt or smaller (GS1), silt to fine sand (GS2), fine to medium sand (GS3), and medium to coarse sand (GS4). Two-tailed p-values (testing the alternative hypothesis that $\mu_A \neq \mu_B$) are reported. P-values passing 95% confidence are highlighted.

Sutton Island, Blunts Point, Pettegrove Point, and Jura have the most outlier high H values. The number of outlier high H points likely contributes to the higher H means observed for the Pettegrove Point and Jura members. Most of the high H targets occur at the Sutton Island/Blunts Point transition as well as the top of the Jura member. Individual observation points skew to high H values in the Pahrump Hills and Pettegrove Point members but the bedrock targets' averaged H stays closer to the Murray formation average value (Figure 3).

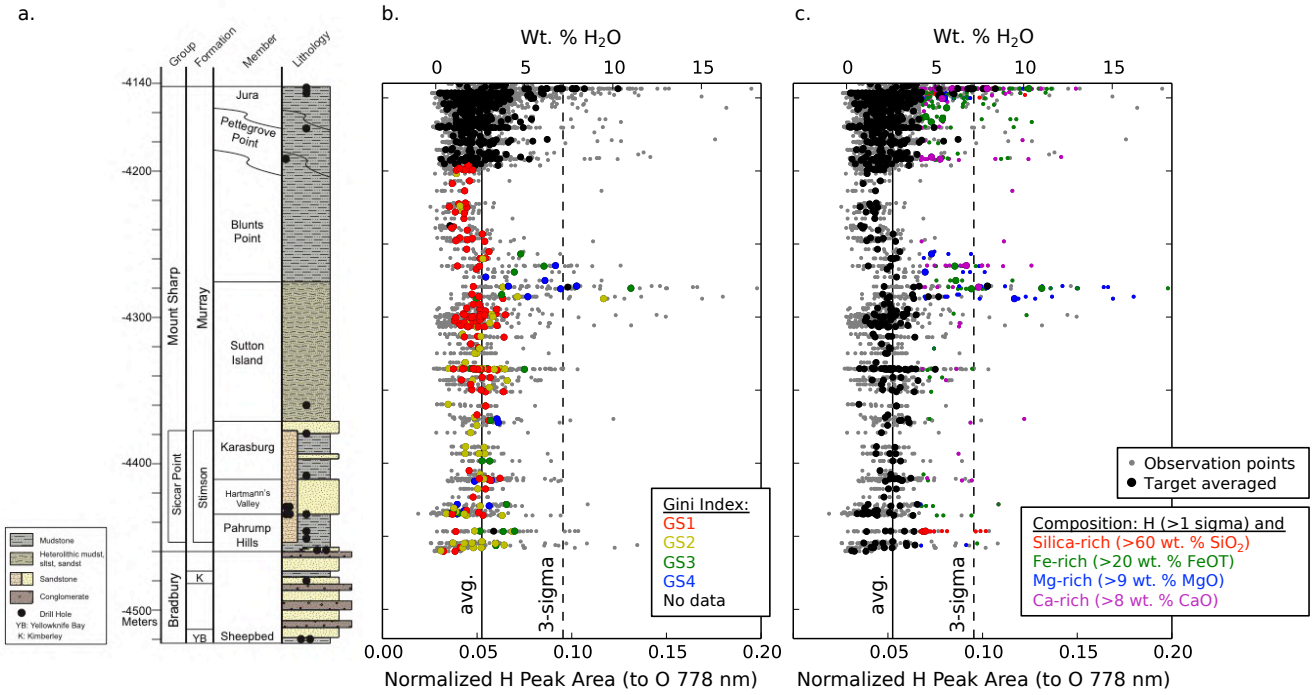

Figure 3. (a) The Gale crater stratigraphic column (MSL Sed-Strat Working Group) with drill sites marked as solid black points and (b-c) the normalized H peak area versus elevation for all ChemCam measured Murray formation bedrock targets. The smaller points are individual point observations and the larger points are target-averaged. Colors in (b) indicate Gini index approximated grain size classes, when available (from Rivera-Hernández et al., 2019). Colors in (c) indicate composition.

The ChemCam H signal varies significantly for bedrock of varying grain sizes as measured by the Gini index (Figure 2; Table 2). The finest grain size category measured, coarse silt or smaller, has a median normalized H peak area of 0.047 or 2.0 wt. % H_2O and the coarsest grain size category, medium to coarse sand, has a median normalized H peak area of 0.059 or 3.3 wt. % H_2O. Coarser grain size targets also have larger variance in normalized H peak area; the distributions for fine to medium sand and medium to coarse sand are skewed to

high H values. Because of the smaller number of targets measured in these larger grain size categories, there is not a significant statistical difference between them (Table 2).

3.2 Chemistry

The majority of bedrock points targeted by ChemCam have major oxide compositions within the standard compositional range of the Murray formation (Figure 4). Where chemical composition varies to higher SiO_2, MgO, FeO_T, and CaO, higher normalized H peak areas are sometimes observed. In particular, there is a clear correlation between H and MgO content, particularly in coarser grained targets. We also tested for correlation between ChemCam H signal and major oxide composition for high H (> 1 sigma) targets using Principal Components Analysis (PCA; Figure 5). The first two principal components show a correlation between H, MgO, and FeO_T. There is also a weak correlation between H and CaO as well as a potential correlation between H and TiO_2 in the third principal component. The H and TiO_2 correlation is suspect due to known ChemCam TiO_2 calibration issues (Frydenvang et al., 2017).

A number of Murray formation bedrock observations such as Wallace_ccam (Figure 6a) contain high SiO_2 (up to 70 wt. % SiO_2) and high H at the base of the Murray formation in Pahrump Hills (Figure 3). These targets are located at the contact between the Murray formation and the overlying Stimson formation in the Marias Pass region. The high SiO_2 targets contain on average 3.5 wt. % H_2O, or 0.06 normalized H peak area, and have grain sizes ranging from silt to medium sand.

Murray formation bedrock targets with high MgO are observed in the Sutton Island member at the transition with the Blunts Point member (Figure 3). ChemCam measurements of these targets show both high MgO (up to 19 wt. % MgO) and high H (normalized H peak area on average 0.11; 8.8 wt. % H_2O). Complementary ChemCam studies have identified S in these targets, suggestive of hydrated Mg-sulfates (Rapin et al.,

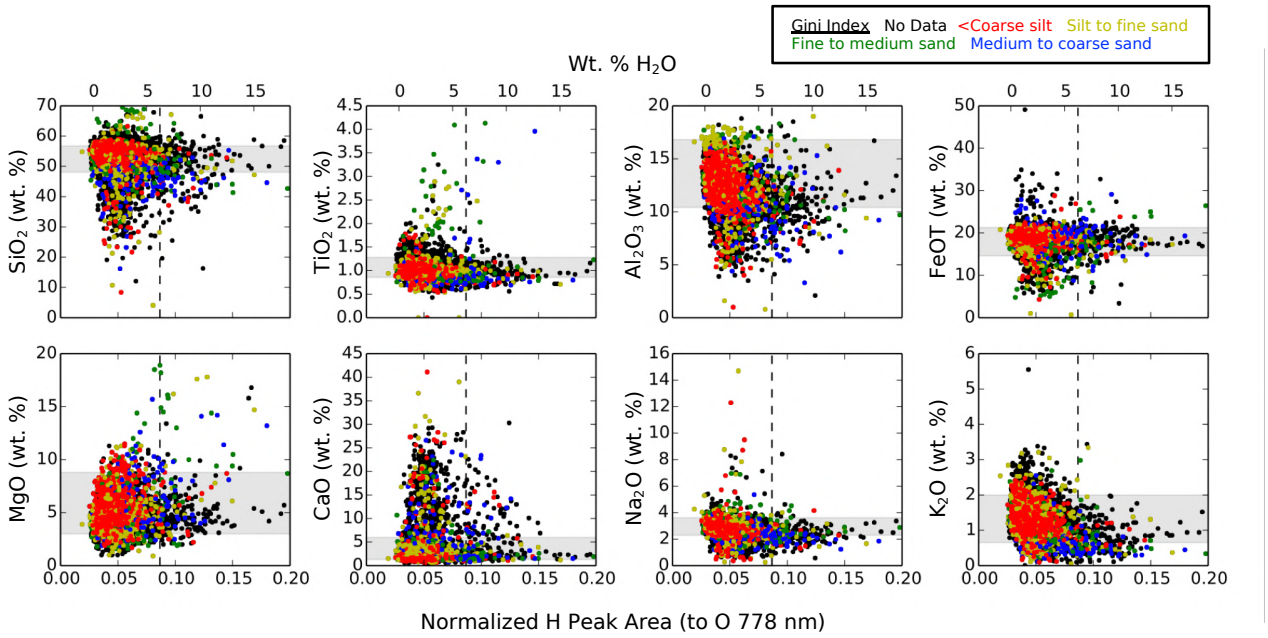

Figure 4. Normalized H peak area, or wt. % H_2O, versus ChemCam major oxides for all Murray formation bedrock observation points. Colors indicate grain size as measured by the Gini index when available. Vertical dashed line signifies 3-sigma high H outliers. Shaded regions are typical Murray bedrock compositions defined by the ChemCam team.

2019; submitted). These Mg and H enriched observation points are most commonly observed in planar exposures of eroded bedrock (Figure 6b). In addition to the hydrated Mg-sulfates, Mg enrichments occur in planar sandstones (Figure 6c) at the Sutton Island/Blunts Point transition in the Newport Ledge region associated with enriched FeO_T (Figure 3), Mn, and P (Meslin et al., 2018; Gasda et al., 2018; Gasda et al., 2019; Lanza et al., 2019). H is also enriched in these targets on average at 0.09 normalized H peak area or 6.5 wt. % H_2O.

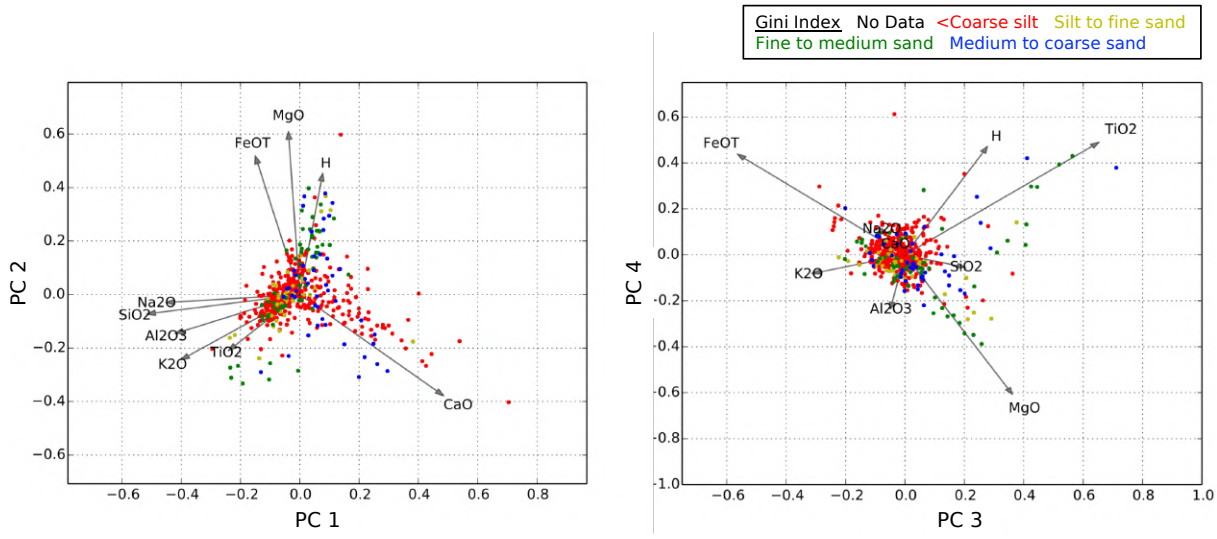

Figure 5. Principal Components Analysis of Murray formation bedrock observation points containing high H (> 1 sigma) chemical composition. Colors indicate grain size as measured by the Gini index. The arrows are the original major oxide and H data axes, projected into the eigenvector space. The arrow lengths represent amount of variance explained by each dimension.

The most frequently enriched major oxide in Murray formation bedrock is CaO (Figure 4). CaO- and H-rich points are scattered throughout the Murray in all members (Figure 3). Ca-sulfate veins, predominately bassanite in composition, are prevalent in the Murray formation (e.g., Rapin et al., 2016), but CaO is also enriched as a pore-filling cement (Newsom et al., 2017). Bedrock targets such as Spectacle Island (Figure 6d) showing no clear point-to-point physical heterogeneities can have CaO enrichments up to ~30 wt. % CaO. On average, CaO-enriched targets (>10 wt. % CaO) do not have highly enriched H (average normalized H peak area 0.06; 3.3 wt. % H_2O). A few Ca-sulfate cemented targets, such as Spectacle Island, have higher H up to ~10 wt. % H_2O, but most Ca-sulfate cemented targets have H signals similar to typical bedrock (Figure 4).

a. Marias Pass, elevation -4446 m

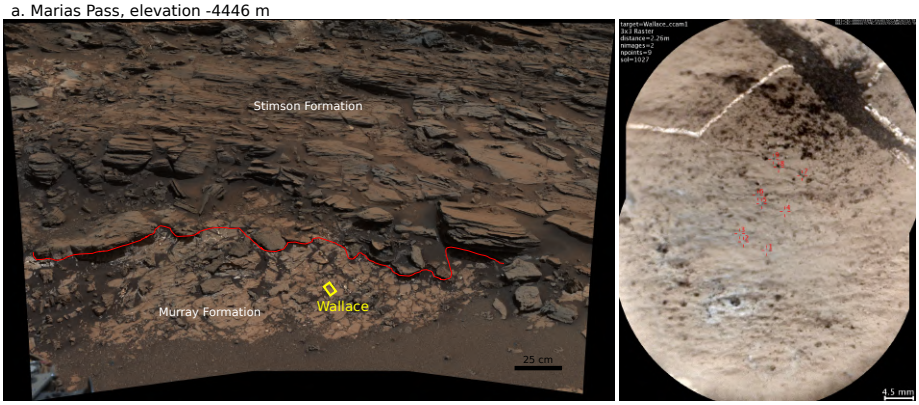

b. Norwood Cove, elevation -4287 m

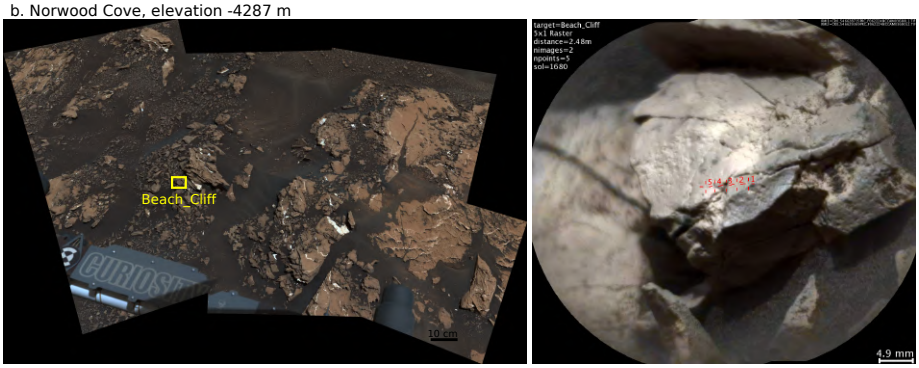

c. Newport Ledge, elevation -4279 m

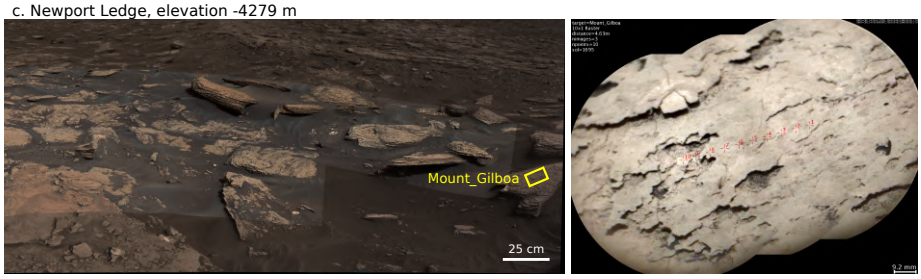

d. Heron Island, elevation -4264 m

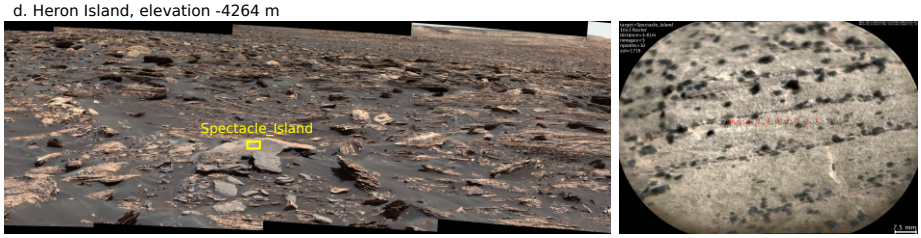

e. Rock Hall, elevation -4143 m

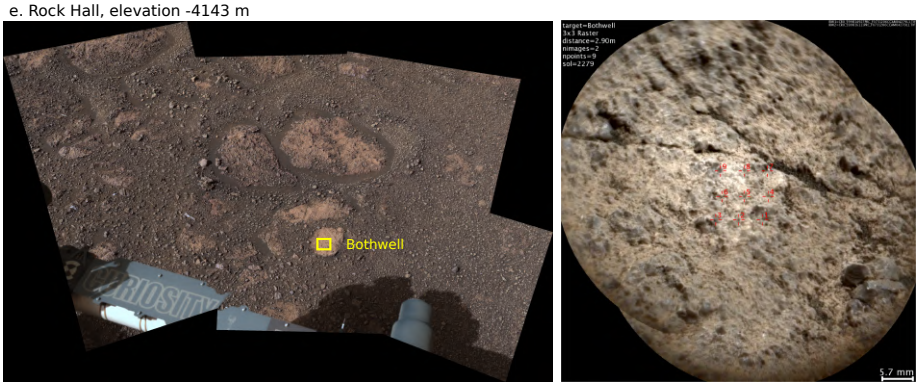

Figure 6. Mastcam mosaics and RMI images of high normalized H peak area targets: (a) opal measured at Marias Pass, (b) hydrated Mg-sulfates at Norwood Cove, (c) H-rich Mn-oxides at Newport Ledge, (d) hydrated Ca-sulfate cement at Heron Island, and (e) akageneite at Rock Hall.

At the highest elevation Vera Rubin ridge drill location in the Jura member, Rock Hall, both the target-averaged H signal increases (Figure 3) and the number of elevated H points increases. The bedrock also has a greater roughness at Rock Hall (Figure 6e), potentially increasing the H signal. Associated with elevated H at Rock Hall, ChemCam measures enriched FeO_T (Figure 3) and Cl is observed sporadically in a few observation points near the detection limit (~3 wt. % Cl; Thomas et al., in revision). H- and CaO-rich targets are common in this area (Figure 3).

4. Discussion

4.1 Uncertainties

ChemCam H peak area values have associated uncertainties from fitting the normalized spectra with an automated routine. In our laboratory characterization of H, we measured homogeneous powderized pellets at five different point locations, and found the standard deviation of the normalized (to O 778 nm) peak area was typically 0.01 (Thomas et al., 2018). In addition, we quantified the uncertainty in our ability to predict weight percent H from LIBS H peak areas by measuring the scatter from our fit linear trends. For the O 778 nm normalization and for samples with less than 1.25 wt. % H, we found uncertainties of ± 0.24 wt. % H or ± 2.1 wt. % H_2O (Thomas et al., 2018). This uncertainty in predicting water content is high, but averaging the prediction for multiple (5-10) observation points on a single ChemCam target in a typical raster, the uncertainty decreases to ± 0.8 wt. % H_2O.

Target roughness is known to artificially increase the measured LIBS H signal (Rapin et al., 2017). While our initial image classification of ChemCam targets was intended to

remove points potentially impacted by strange surface geometries (cracks, pits, etc.), over 19,000 points were individually classified by eye and some scatter in the H signal observed is likely due to roughness effects missed by the visual classification. H signals averaged by target are likely less influenced by roughness effects which might impact 1-2 random points, so overall H trends are more trustworthy than individual point observations. On a larger scale, all targets measured at Rock Hall have rough surfaces and the H signal may be artificially increased.

Grain size is suspected to similarly impact the LIBS H signal (Thomas et al., 2018) although laboratory studies have not yet confirmed this physical matrix effect. While the Gini index may not be a perfect measure of bedrock grain size (see discussion in §2), we can use it to perform a test for correlation between LIBS H signal and grain size. There is only a weak correlation ($R^2 = 0.23$) between the Gini index mean score and normalized H peak area, but the distributions of different grain size categories differ significantly (Figure 2, Table 2). Future laboratory studies of samples with controlled, varying grain sizes are necessary to quantify how grain size physical matrix effects impact measurement of H and other volatile elements.

4.2 Comparison to other instruments

The average water content of the Murray formation measured with ChemCam (average ± standard deviation: 2.6 ± 2.1 wt. % H_2O) is consistent with measurements by other MSL instruments. DAN has measured 4.2 ± 0.51 WEH (water equivalent hydrogen; Gabriel et al., 2018) in the Sebina region of the Murray formation (lower Sutton Island member) where ChemCam measures only 2.1 ± 1.2 wt. % H_2O. From sol 753-1292 of the mission, DAN measured on average 1.6 ± 1.1 WEH (Tate et al., 2019) and ChemCam measured 2.3 ± 2.0 wt. % H_2O. DAN and ChemCam sample very different depths; ChemCam samples the upper ~microns of the surface while DAN measures the upper ~0.5 m of material. The scales of the instruments are also very different - ~100s of microns versus ~few meters – so discrepancies in measured H content between DAN and ChemCam are expected. In particular, minerals like Ca-sulfates at the surface dehydrate under normal Gale crater

environmental conditions (Vaniman et al., 2018), so higher H measured at depth with DAN due to surface dehydration is likely. Additionally, ChemCam and DAN are not measuring the same exact targets or regions; H may vary within a region.

For Murray formation targets up to the Sutton Island member, the SAM instrument measured at minimum 1.1 ± 0.6 wt. % H_2O at Telegraph Peak and at maximum 2.5 ± 1.6 wt. % H_2O at Mojave (Sutter et al., 2017). Our ChemCam measurements fall within this range of values. Our survey covers the entire Murray formation to sol 2339 while SAM is limited by drill sampling, making comparison limited to only the 10 drill targets in the Murray formation.

4.3 Carriers of enrichment

ChemCam cannot measure mineralogy, so we are limited to inferences based on chemical composition and comparison to CheMin for drilled targets. Up to ~28 wt. % clay minerals have been detected in Murry formation drilled targets (Bristow et al., 2018). Phyllosilicate interlayer water (the lower temperature 100-300 C release observed by SAM) and bound OH (the higher temperature 650-800 C release observed by SAM) likely contribute to ChemCam measured H in the Murray formation (Sutter et al., 2017). Jarosite has been detected by CheMin in Confidence Hills, Mojave, and Telegraph Peak (Rampe et al., 2017). In addition, CheMin has measured X-ray amorphous phases in all drilled samples. Phases such as poorly crystalline aluminosilicate or amorphous silicate (opal-A) and nanophase oxyhydroxides (e.g., ferrihydrite) could contribute to our measured bulk H (Sutter et al., 2017).

ChemCam-detected differences in average H between different members of the Murray formation could be due to variation in physical properties for mudstones vs. sandstones such as roughness and grain size but also could represent changes in the chemistry of depositional waters or later diagenetic fluids. Here, we discuss potential carriers of enrichment for the ChemCam observed variability in H signal in stratigraphic order.

MSL Curiosity observed the contact between the Murray and Stimson formations at Marias Pass. In this region, clear alteration halos were observed crosscutting the Murray/Stimson contact (Frydenvang et al., 2017). The diagenetic halos are very SiO_2 rich (up to ~90 wt. % SiO_2) and contain elevated H consistent with opal (Rapin et al., 2018). Nearby Murray bedrock targets part of our survey are also silica and H enriched (Figure 6a). The opal likely formed from multiple diagenetic fluid events and possibly represents extensive late water-rock interaction (Frydenvang et al., 2017; Rapin et al., 2018). Leaching of Mg, Al, Mn, Fe, Ni, and Zn along with enrichment of Si and S are reported by APXS and are consistent with infiltration of subsurface fluids, initially acidic and later alkaline, propagating along fractures crosscutting the Stimson/Murray contact (Yen et al., 2017). The enrichment of Si and H even in visibly unaltered nearby bedrock observed by this study supports pervasive aqueous alteration in the area.

The transition from Sutton Island, composed of heterolithic mudstones and sandstones and interpreted as forming in a marginal lake setting, to Blunts Point, primarily finely-laminated mudstones interpreted as forming in a suspension/fall-out lacustrine setting, has both elevated bulk (target-averaged) H and outlier high H targets. In the Norwood Cove region, high H is associated with elevated Mg. Rapin et al. (2019; submitted) have reported S in these Mg- and H-rich targets in a relatively thin (<10 m) stratigraphic interval in planar exposures of erosion-resistant rocks. Early diagenetic precipitation from a concentrated, saline brine created by evaporation is the favored formation pathway for these hydrated Mg-sulfates (Rapin et al., 2019; submitted).

The entire Murray formation (Figure 3) is often variably enriched in Ca-sulfate in the bedrock. While the bedrock Ca-sulfate cement on average is not H-rich according to our measurements, a few targets such as Spectacle_Island have higher H more consistent with bassanite composition. Our observations of varying H signals in Ca-enriched targets are consistent with CheMin measurements of gypsum, bassanite, and anhydrite occurring together in Gale sedimentary rocks (Vaniman et al., 2018). The observed frequency of hydrated Ca-sulfate cements in the Murray implies extensive S-rich groundwater

alteration. The observed frequency of hydrated Ca-sulfate cements in the Murray implies extensive S-rich groundwater alteration and, in some instances, primary deposition (Rapin et al., 2019; submitted).

The Newport Ledge area is also at the transition from the Sutton Island to Blunts Point member. Newport Ledge sandstones have on average 4.6 wt. % MnO_T in dark-toned rocks and 1.5 wt. % MnO_T in light-toned rocks compared to 0.5 wt. % MnO_T on average in Sutton Island and Blunts Point (Gasda et al., 2019). FeO_T and MgO are also enriched in some targets (Figure 3). These targets, such as Mount_Gilboa (Figure 6c), are H-rich and contain on average 6.6 ± 3.8 wt. % H_2O. Variable P is detected in Newport Ledge targets (Meslin et al., 2018). The most likely carrier phase is hydrous Mn-oxides and Fe-oxides with adsorped phosphates (Kawashima et al., 1986). Hydrous Mn-oxides and Fe-oxides suggest oxidizing, aqueous conditions either during primary sediment deposition within the lake and/or in groundwaters post lithification (Lanza et al., 2019). The deposits at Newport Ledge may be due to changes in water depth or shifting shoreline locations (Lanza et al., 2019).

At the Rock Hall drill site, at the top of the Vera Rubin ridge in the Jura member, ChemCam observations indicate a substantial increase in bedrock H content (5.5 ± 3.4 wt. % H_2O) as well as many high H targets. Some of this increase may be artificial; targets at Rock Hall are rougher (on the ~mm to cm scale) than typical Murray bedrock. ChemCam observes enriched FeO_T correlated with high H at Rock Hall (Figure 3). CheMin has detected ~7 wt. % akageneite, a chlorine bearing iron hydroxide, and ~1 wt. % jarosite, an Fe-containing sulfate (Morris et al., 2019). This CheMin analysis along with our observed FeO_T/H correlation suggest akageneite and jarosite may be the H carrier phases. Rock Hall is quite different from other Vera Rubin ridge drill targets; akaganeite is present at levels higher than hematite and more jarosite is present. SAM also observes nitrates and oxychlorine (Rampe et al., 2019 MSL team meeting) suggesting the Rock Hall area experienced interaction with later saline fluids. While our measurements of H at Rock Hall are subject to higher uncertainty due to physical matrix effects, SAM and CheMin observations

confirm Rock Hall is different from other Vera Rubin ridge areas and some of the observed H increase is likely real.

Variability in the average H content of the Murray formation as well as observations of specific H-enriched phases in intervals of the Murray formation suggest an history of multiple episodes of water-rock interaction. Disentangling changes in lakewater fluid chemistry from later diagenetic fluid events is difficult, but large-scale variation in bedrock H such as enrichment at the Sutton Island/Blunts Point transition may point to changes in the Gale crater paleoenvironment which produced more saline, oxidized lakewaters which precipitated hydrated sulfates and hydrous Mn-oxides. In the Sutton Island/Blunts Point transition case, this may be due to changing water depth or shoreline location (Lanza et al., 2019). Both the Marias Pass and Rock Hall H variability is likely due to later groundwater episodes enriching H and silica or the oxidative dissolution of Fe (II) minerals.

5. Conclusions

We have quantified the ChemCam normalized H peak area for all Murray formation bedrock targets up to mission sol 2339 and found the Murray formation contains on average 2.6 ± 2.1 wt. % H_2O. While our measurement uncertainty of H in individual ChemCam observation points is high (± 2.1 wt. % H_2O), the target-averaged uncertainty is lower (~ ± 0.8 wt. % H_2O). Roughness effects may artificially increase the H signal of some observation points, and future laboratory studies will measure the dependence of target grain size on the H signal. Many rough targets are measured at Rock Hall, potentially artificially increasing the measured H signal.

ChemCam data reveal significant H enrichment in select intervals within the Murray formation that signify distinctive aqueous processes. While the target-averaged H signal remains constant for most of the Murray formation, the Hartmann's Valley, Pettegrove Point, and Jura members show significant variation in H signal from the other members. Carriers of H enrichment in the Murray formation include clays, amorphous materials, and Ca-sulfates throughout. Enrichment in H at the Sutton Island/Blunts Point transition and

the presence of hydrated Mg-sulfates and Mn-oxides suggests changing lakewaters including increased salinity and changes in lakewater depth or shoreline location. Opal likely formed from extensive late-stage alteration at the Stimson/Murray contact at Marias Pass. Akaganeite and jarosite are potential carrier phases of the high H observed at Rock Hall, and complementary SAM and CheMin observations suggest Rock Hall bedrock experienced alteration by later saline fluids. Variability in the H signal may be evidence of changes in the depositional lakewaters or later diagenetic fluid events, which are difficult to disentangle.

References

Anderson, R. B., Morris, R. V., Clegg, S. M., Bell, J. F., Wiens, R. C., Humphries, S. D., … McInroy, R. (2011). The influence of multivariate analysis methods and target grain size on the accuracy of remote quantitative chemical analysis of rocks using laser induced breakdown spectroscopy. *Icarus, 215*(2), 608–627. http://doi.org/10.1016/j.icarus.2011.07.034

Blake, D., Vaniman, D., Achilles, C., Anderson, R., Bish, D., Bristow, T., … Yen, A. (2012). Characterization and Calibration of the CheMin Mineralogical Instrument on Mars Science Laboratory. *Space Science Reviews, 170*(1–4), 341–399. http://doi.org/10.1007/s11214-012-9905-1

Bristow, T. F., Rampe, E. B., Achilles, C. N., Blake, D. F., Chipera, S. J., Craig, P., … Yen, A. S. (2018). Clay mineral diversity and abundance in sedimentary rocks of Gale crater, Mars. *Science Advances, 4*(6), eaar3330. http://doi.org/10.1126/sciadv.aar3330

Clegg, S. M., Sklute, E., Dyar, M. D., Barefield, J. E., & Wiens, R. C. (2009). Multivariate analysis of remote laser-induced breakdown spectroscopy spectra using partial least squares, principal component analysis, and related techniques.

Spectrochimica Acta Part B: Atomic Spectroscopy, *64*(1), 79–88. http://doi.org/10.1016/j.sab.2008.10.045

Fraeman, A. A., Ehlmann, B. L., Arvidson, R. E., Edwards, C. S., Grotzinger, J. P., Milliken, R. E., … Rice, M. S. (2016). The stratigraphy and evolution of lower Mount Sharp from spectral, morphological, and thermophysical orbital data sets. *Journal of Geophysical Research: Planets*, *121*(9), 1713–1736. http://doi.org/10.1002/2016JE005095

Frydenvang, J., Gasda, P. J., Hurowitz, J. A., Grotzinger, J. P., Wiens, R. C., Newsom, H. E., … Vasavada, A. R. (2017). Diagenetic silica enrichment and late-stage groundwater activity in Gale crater, Mars. *Geophysical Research Letters*, *44*(10), 4716–4724. http://doi.org/10.1002/2017GL073323

Gabriel, T. S. J., Hardgrove, C., Czarnecki, S., Rampe, E. B., Rapin, W., Achilles, C. N., … Downs, R. T. (2018). Water Abundance of Dunes in Gale Crater, Mars From Active Neutron Experiments and Implications for Amorphous Phases. *Geophysical Research Letters*, *45*(23), 12,766-12,775. http://doi.org/10.1029/2018GL079045

Gasda, P. J., Lanza, N. L., Lamm, S. N., L'Haridon, J., Meslin, P.-Y., Forni, O., … Maurice, S. (2018). Evidence of Redox Sensitive Elements Associated with Possible Shoreline Deposits in Gale Crater. Paper presented at 49th Lunar and Planetary Science Conference, The Woodlands, TX (p. 2483).

Gasda, P. J., Lanza, N. L., Meslin, P.-Y., Forni, O., L'Haridon, J., Fischer, W. W., … Maurice, S. (2019). High-Mn Sandstone as Evidence for Oxidized Conditions in Gale Crater Lake. Paper presented at 50th Lunar and Planetary Science Conference, The Woodlands, TX (p. 1620).

Grotzinger, J. P., Gupta, S., Malin, M. C., Rubin, D. M., Schieber, J., Siebach, K., … Mcbride, M. J. (2015). Deposition, exhumation, and paleoclimate of an ancient lake deposit, Gale crater, Mars, *350*(6257). http://doi.org/10.1126/science.aac7575

Hurowitz, J. A., Grotzinger, J. P., Fischer, W. W., McLennan, S. M., Milliken, R. E., Stein, N., … Wiens, R. C. (2017). Redox stratification of an ancient lake in Gale crater, Mars. *Science*, *356*(6341), eaah6849. http://doi.org/10.1126/science.aah6849

Lanza, N. L., Fischer, W. W., Lamm, S. N., Gasda, P. J., Meslin, P.-Y., Ollila, A. M., … Wiens, R. C. (2019). Variable Redox Conditions in Gale Crater as Indicated by Manganese Abundance Along the Curiosity Traverse. Paper presented at 50th Lunar and Planetary Science Conference, The Woodlands, TX (p. 3146).

Mahaffy, P. R., Webster, C. R., Cabane, M., Conrad, P. G., Coll, P., Atreya, S. K., … Mumm, E. (2012). The Sample Analysis at Mars Investigation and Instrument Suite. *Space Science Reviews*, *170*(1–4), 401–478. http://doi.org/10.1007/s11214-012-9879-z

Mangold, N., Dehouck, E., Fedo, C., Forni, O., Achilles, C., Bristow, T., … Wiens, R. C. (2019). Chemical alteration of fine-grained sedimentary rocks at Gale crater. *Icarus*, *321*(March 2018), 619–631. http://doi.org/10.1016/j.icarus.2018.11.004

Maurice, S., Wiens, R. C., Saccoccio, M., Barraclough, B., Gasnault, O., Forni, O., … Vaniman, D. (2012). The ChemCam Instrument Suite on the Mars Science Laboratory (MSL) Rover: Science Objectives and Mast Unit Description. *Space Science Reviews*, *170*(1–4), 95–166. http://doi.org/10.1007/s11214-012-9912-2

Meslin, P.-Y., Gasnault, O., Forni, O., Schröder, S., Cousin, A., Berger, G., … Berger, J. (2013). Soil Diversity and Hydration as Observed by ChemCam at Gale Crater, Mars. *Science*, *341*(6153), 1238670–1238670. http://doi.org/10.1126/science.1238670

Meslin, P.-Y., Gasda, P., L'Haridon, J., Forni, O., Lanza, N., Lamm, S., … Lasue, J. (2018). Detection of Hydrous Manganese and Iron Oxides with Variable Phosphorous and Magnesium Contents in the Lacustrine Sediments of the Murray

Formation, Gale, Mars. Paper presented at 49th Lunar and Planetary Science Conference, The Woodlands, TX (p. 1447).

Milliken, R. E., Grotzinger, J. P., & Thomson, B. J. (2010). Paleoclimate of Mars as captured by the stratigraphic record in Gale Crater. *Geophysical Research Letters*, *37*(4), 1–6. http://doi.org/10.1029/2009GL041870

Mitrofanov, I. G., Litvak, M. L., Varenikov, A. B., Barmakov, Y. N., Behar, A., Bobrovnitsky, Y. I., … Vostrukhin, A. A. (2012). Dynamic Albedo of Neutrons (DAN) Experiment Onboard NASA's Mars Science Laboratory. *Space Science Reviews*, *170*(1–4), 559–582. http://doi.org/10.1007/s11214-0129924-y

Morris, R. V., Bristow, T. F., Rampe, E. B., Yen, A. S., Vaniman, D. T., Tu, V., … Achilles, C. N. (2019). Mineralogy and Formation Processes for the Vera Rubin Ridge at Gale Crater, Mars from CheMin XRD Analyses. Paper presented at 50th Lunar and Planetary Science Conference, The Woodlands, TX (p. 1127).

Nachon, M., Clegg, S. M., Mangold, N., Schröder, S., Kah, L. C., Dromart, G., … Wellington, D. (2014). Calcium sulfate veins characterized by ChemCam/Curiosity at Gale crater, Mars. *Journal of Geophysical Research: Planets*, *119*(9), 1991–2016. http://doi.org/10.1002/2013JE004588

Newsom, H. E., Jackson, R., Wiens, R. C., Frydenvang, J., Gasda, P., Lanza, N., … Bridges, J. (2017). Increasing Occurrences of Sandstone Cemented with Calcium Sulfate on Mount Sharp, Gale Crater, Mars. Paper presented at 48th Lunar and Planetary Science Conference, The Woodlands, TX (p. 2495).

O'Connell-Cooper, C. D., Spray, J. G., Thompson, L. M., Gellert, R., Berger, J. A., Boyd, N. I., … VanBommel, S. J. (2017). APXS-derived chemistry of the Bagnold dune sands: Comparisons with Gale Crater soils and the global Martian average. *Journal of Geophysical Research: Planets*, *122*(12), 2623–2643. http://doi.org/10.1002/2017JE005268

Rampe, E. B., Ming, D. W., Blake, D. F., Bristow, T. F., Chipera, S. J., Grotzinger, J. P., … Thompson, L. M. (2017). Mineralogy of an ancient lacustrine mudstone succession from the Murray formation, Gale crater, Mars. *Earth and Planetary Science Letters*, *471*, 172–185. http://doi.org/10.1016/j.epsl.2017.04.021

Rapin, W., Meslin, P.-Y., Maurice, S., Vaniman, D., Nachon, M., Mangold, N., … Archer, D. (2016). Hydration state of calcium sulfates in Gale crater, Mars: Identification of bassanite veins. *Earth and Planetary Science Letters*, *452*, 197–205. http://doi.org/10.1016/j.epsl.2016.07.045

Rapin, W., Bousquet, B., Lasue, J., Meslin, P.-Y., Lacour, J.-L., Fabre, C., … Cousin, A. (2017). Roughness effects on the hydrogen signal in laser-induced breakdown spectroscopy. *Spectrochimica Acta Part B: Atomic Spectroscopy*, *137*, 13–22. http://doi.org/10.1016/j.sab.2017.09.003

Rapin, W., Chauviré, B., Gabriel, T. S. J., McAdam, A. C., Ehlmann, B. L., Hardgrove, C., … Schröder, S. (2018). In Situ Analysis of Opal in Gale Crater, Mars. *Journal of Geophysical Research: Planets*, *123*(8), 1955–1972. http://doi.org/10.1029/2017JE005483

Rapin, W., Meslin, P.-Y., Maurice, S., Wiens, R. C., Laporte, D., Chauviré, B., … Thomas, N. H. (2017). Quantification of water content by laser induced breakdown spectroscopy on Mars. *Spectrochimica Acta Part B: Atomic Spectroscopy*, *130*, 82–100. http://doi.org/10.1016/j.sab.2017.02.007

Rapin, W., Ehlmann, B. L., Dromart, G., Schieber, J., Thomas, N., Fischer, W. W., … Vasavada, A. (2019). High Salinity Recorded by Bedrock Sulfate Enrichments at Gale Crater. Paper presented at 50th Lunar and Planetary Science Conference, The Woodlands, TX (p. 2147).

Rivera-Hernández, F., Sumner, D. Y., Mangold, N., Stack, K. M., Forni, O., Newsom, H., … Maurice, S. (2019). Using ChemCam LIBS data to constrain grain size in

rocks on Mars: Proof of concept and application to rocks at Yellowknife Bay and Pahrump Hills, Gale crater. *Icarus*, *321*(October 2018), 82–98. http://doi.org/10.1016/j.icarus.2018.10.023

Schröder, S., Meslin, P.-Y., Gasnault, O., Maurice, S., Cousin, A., Wiens, R. C., … Vaniman, D. (2015). Hydrogen detection with ChemCam at Gale crater. *Icarus*, *249*, 43–61. http://doi.org/10.1016/j.icarus.2014.08.029

Schröder, S., Rammelkamp, K., Vogt, D. S., Gasnault, O., & Hübers, H.-W. (2019). Contribution of a martian atmosphere to laser-induced breakdown spectroscopy (LIBS) data and testing its emission characteristics for normalization applications. *Icarus*, *325*(December 2018), 1–15. http://doi.org/10.1016/j.icarus.2019.02.017

Sutter, B., McAdam, A. C., Mahaffy, P. R., Ming, D. W., Edgett, K. S., Rampe, E. B., … Yen, A. S. (2017). Evolved gas analyses of sedimentary rocks and eolian sediment in Gale Crater, Mars: Results of the Curiosity rover's sample analysis at Mars instrument from Yellowknife Bay to the Namib Dune. *Journal of Geophysical Research: Planets*, *122*(12), 2574–2609. http://doi.org/10.1002/2016JE005225

Tate, C. G., Moersch, J., Ehresmann, B., Jun, I., Hardgrove, C., Litvak, M., … Vostrukhn, A. (2017). Refined Water Equivalent Hydrogen Estimates Using Passive Data from the MSL Dynamic Albedo of Neutrons Experiment: Sols 0-753. Paper presented at 48th Lunar and Planetary Science Conference, The Woodlands, TX (p. 1455).

Tate, C. G., Moersch, J. E., Mitrofanov, I., Litvak, M., Bellutta, P., Boynton, W. V., … Zeitlin, C. (2019). Mars Science Laboratory Dynamic Albedo of Neutrons Passive Mode Data and Results from Sols 753 to 1292: Pahrump Hills to Naukluft Plateau. Paper presented in 50th Lunar and Planetary Science Conference, The Woodlands, TX (p. 2132).

Thomas, N. H., Ehlmann, B. L., Anderson, D. E., Clegg, S. M., Forni, O., Schröder, S., … Maurice, S. (2018). Characterization of Hydrogen in Basaltic Materials With Laser-Induced Breakdown Spectroscopy (LIBS) for Application to MSL ChemCam Data. *Journal of Geophysical Research: Planets*, *123*(8), 1996–2021. http://doi.org/10.1029/2017JE005467

Vaniman, D. T., Martínez, G. M., Rampe, E. B., Bristow, T. F., Blake, D. F., Yen, A. S., … Sumner, D. Y. (2018). Gypsum, bassanite, and anhydrite at Gale crater, Mars. *American Mineralogist*, *103*(7), 1011–1020. http://doi.org/10.2138/am-2018-6346

Wiens, R. C., Maurice, S., Barraclough, B., Saccoccio, M., Barkley, W. C., Bell, J. F., … Wong-Swanson, B. (2012). The ChemCam Instrument Suite on the Mars Science Laboratory (MSL) Rover: Body Unit and Combined System Tests. *Space Science Reviews*, *170*(1–4), 167–227. http://doi.org/10.1007/s11214-012-9902-4

Chapter 4

MARS SCIENCE LABORATORY OBSERVATIONS OF CHLORIDE SALTS IN GALE CRATER, MARS

N. H. Thomas[1], B. L. Ehlmann[1,2], P.-Y. Meslin[3], W. Rapin[1], D. E. Anderson[1], F. Rivera- Hernández[4], O. Forni[3], S. Schröder[5], A. Cousin[3], N. Mangold[6], R. Gellert[7], O. Gasnault[3], and R. C. Wiens[8]

[1] Division of Geological and Planetary Sciences, California Institute of Technology, Pasadena, California, USA.

[2] Jet Propulsion Laboratory, California Institute of Technology, Pasadena, California, USA.

[3] Institut de Recherche en Astrophysique et Planétologie, Université de Toulouse, CNRS, UPS, CNES, Toulouse, France.

[4] Dartmouth College, Hanover, NH,

[5] German Aerospace Center (DLR), Berlin, Germany.

[6] Laboratoire de Planétologie et Géodynamique, UMR6112, CNRS, Université de Nantes, Nantes, France.

[7] Department of Physics, University of Guleph, Guleph, Ontario, Canada,

[8] Los Alamos National Laboratory, Los Alamos, New Mexico, USA.

Corresponding author: Nancy H. Thomas (nhthomas@caltech.edu)

Key Points:

- Isolated Cl enrichments in bedrock, in nodular textures, and at calcium sulfate vein margins, correlated with Na, indicate halite
- Mapping of Cl along the *Curiosity* traverse in Gale Crater indicates Cl enrichments are more common in select Murray formation members
- The scattered, isolated occurrences of chlorides are consistent with late groundwater reworking and remobilization of original deposits

Thomas, N. H., et al. (2019). Mars Science Laboratory Observations of Chloride Salts in Gale Crater, Mars. *Geophysical Research Letters.* Under review.

Abstract

The Mars Science Laboratory *Curiosity* rover is traversing a sequence of stratified sedimentary rocks in Gale crater that contain varied aeolian, fluviodeltaic, and lake deposits, with phyllosilicates, iron oxides, and sulfate salts. Here, we report the chloride salt distribution along the rover traverse. Chlorine is detected at low levels (<3 wt.%) in soil and rock targets with multiple MSL instruments. Isolated fine-scale observations of high chlorine (up to ≥ 15 wt.% Cl), detected using the ChemCam instrument, are associated with elevated Na_2O and interpreted as halite grains or cements in bedrock. Halite is also interpreted at the margins of veins and in nodular, altered textures. We have not detected halite in obvious evaporitic layers. Instead, its scattered distribution suggests that chlorides emplaced earlier in particular members of the Murray formation were remobilized and reprecipitated by later groundwaters within Murray formation mudstones and in diagenetic veins and nodules.

1. Introduction

Evaporite mineral assemblages record the physical and chemical characteristics of past environments and allow us to place constraints on the chemistry of surface and subsurface fluids. In terrestrial environments, soluble chloride salts are typically among the last minerals to precipitate out of saline brines, preceded by various carbonates and sulfates, and are predicted to precipitate from fluids derived from basaltic weathering on Mars (Tosca and McLennan, 2006).

The Mars Odyssey Gamma Ray Spectrometer has mapped the global distribution of chlorine (Diez et al., 2009), and specific chloride-enriched deposits were discovered in hundreds of irregular depressions in ancient terrains of the southern martian highlands using the Mars Odyssey Thermal Emission Imaging System (Osterloo et al., 2010). These chlorides likely precipitated by evaporation from a ponded brine derived from groundwater upwelling and/or surface runoff. Chlorides can also form via efflorescence, the migration of saline fluids to the surface whereupon salts crystallize within sediment grains as thin crusts, as is thought to explain Cl-enriched veneers and surface rinds at Meridiani Planum (Knoll et al., 2008) and

Cl-enriched soils and rock rinds at Gusev crater (Gellert et al., 2004; Haskin et al., 2005; Ming et al., 2006) detected by the Alpha Particle X-ray Spectrometer (APXS) instruments on *Opportunity* and *Spirit*. Chlorine has been found in all martian soils and dust at ~0.5-1 wt.% Cl (Yen et al., 2005; Berger et al., 2016; Cousin et al., 2017; Lasue et al., 2018). In situ soil studies have measured perchlorates (Hecht et al., 2009), and halite specifically has been detected in evaporitic mineral assemblages in the nakhlite meteorites (Bridges & Grady, 2000).

The Mars Science Laboratory (MSL) *Curiosity* rover is investigating the stratigraphy of Mt. Sharp, the mound of sedimentary rocks filling the center of 155-km Gale crater, which formed ~3.8-3.6 Ga ago. Most of Gale's sedimentary rocks examined so far formed in a fluvio-lacustrine environment, including both fluvial/alluvial deposits and laminated mudstones from subaqueous deposition (Grotzinger et al., 2015; Hurowitz et al., 2017; Rivera-Hernández et al., 2019). Ca-sulfates containing boron (Gasda et al., 2017), Mg-sulfates (Rapin et al., 2019; submitted), desiccation features (Stein et al., 2018), and clay chemistries (Bristow et al., 2018) reported in Gale suggest past episodes of lake drying or lake level drop. Orbital surveys have not detected chlorides within Gale, but they are found in the nearby watershed of Sharp crater (Ehlmann and Buz, 2015). The Dynamic Albedo of Neutrons instrument is sensitive to Cl (Litvak et al., 2016), and APXS observations have found on average 1.0-1.4 wt.% Cl and up to 3.3 wt. % Cl in Gale's sedimentary rocks (O'Connell-Cooper et al., 2017). Localized Cl enrichments have been reported in association with diagenetic raised ridges at Yellowknife Bay (McLennan et al., 2014; Léveillé et al., 2014) and halite has been reported in association with Ca-sulfate veins (Nachon et al., 2014; Forni et al., 2015) but chlorine has not previously been systematically mapped in Gale crater sediments nor has a model for the origin, genesis, and distribution of these compounds been discussed.

In this paper we report the chlorine distribution in rocks and soils along Curiosity's traverse, using multiple instruments, in particular focusing on observations that indicate small-scale enrichments in chloride salts, in order to inform our understanding of the depositional and

groundwater environments at Gale crater. We report on their ChemCam detections as a function of stratigraphic level and target type and draw on supporting information from CheMin and SAM to identify the type of chloride salt present and determine its formation mechanism.

2. Methodology

APXS data from the arm-mounted instrument, placed on or just above the surface of Mars, were used to determine bulk soil and rock Cl values over a spot size of 1.7-3 cm for 687 observations (up to sol 2168), using the APXS standard calibration (Gellert, 2006).

ChemCam Laser-Induced Breakdown Spectroscopy (LIBS) data from the mast-mounted remote sensing instrument provided chemical analyses of >19,000 locations at fine-scale (350-550 µm diameter; Maurice et al., 2012) of targets typically 2-4 m away with Remote Micro-Imager (RMI) data for co-located context images (Wiens et al., 2012; Maurice et al., 2012). Major element compositions are calculated using multivariate techniques (Clegg et al., 2017; R. Anderson et al., 2017) but the detection and quantification of minor elements like Cl is complicated by relatively few, weak emission lines, interference with emission lines from other elements, and physical and chemical matrix effects. Neither APXS or ChemCam can directly measure mineralogy and directly differentiate chlorides from perchlorates or chlorates, but can infer mineralogy using correlations between elements.

Univariate analysis has been successfully applied to detect and quantify minor elements with ChemCam, e.g., Li, Mn, and H (e.g., Ollila et al., 2014; Lanza et al., 2014; Rapin et al., 2017a; Payré et al., 2017; Thomas et al., 2018). We extended previous LIBS analyses of Cl in the laboratory (e.g., D. Anderson et al., 2017; Vogt et al., 2018) for analysis of ChemCam data. We apply standard ChemCam data pre-processing, removing the first five laser shots, which are contaminated by dust and subject to surface effects (as detailed in Wiens et al., 2013). We use the Cl emission line at 837.8 nm that increases monotonically with Cl content regardless of cation (D. Anderson et al., 2017) rather than the molecular emission from CaCl which is complex and not easily used for direct quantification (Vogt et al., 2018). To quantify

Cl, we fit the local region (831-841 nm) using methods described by Thomas et al. (2018) and report the fit Cl peak area. Before fitting, we normalize the shot-averaged spectrum using the standard ChemCam Norm 3 method which divides the spectra by the total detector intensity (in the case of Cl 838 nm, the VNIR detector – one of three in the instrument). While Rapin et al. (2017) and Thomas et al. (2018) found normalization using C and O emission lines to work best in H quantification, D. Anderson et al. (2017) and additional lab measurement analyses done for this work indicate that Norm 3 provides the most linear calibrations with Cl concentration (see also Discussion §4.2).

We constrained the ChemCam threshold of detection of Cl by three approaches. First, the threshold must be >0.03 wt.% Cl because no Cl peak is observed for the ChemCam calibration targets. The KGa-2 calibration target contains 0.03 wt.% Cl and the others have <0.01 wt.% Cl (Vaniman et al., 2012). Second, the threshold for loosely consolidated materials like soils must be <~1 wt.% Cl because a small Cl peak (peak area 0.83×10^{-4}) is seen in the dust, measured by the first shot of ChemCam analyses (Lasue et al., 2018). APXS measures 0.79-1.35 wt.% Cl in the Gale dust (Berger et al., 2016). Because of potential physical matrix effects, this same threshold may not apply to bedrock observations (e.g., Rapin et al., 2017b; Thomas et al., 2018; and references therein). Third, the highest APXS Cl measurement in Gale is the bedrock target Stephen with 3.3 wt.% Cl, where ChemCam observes a small Cl peak (average Cl peak area 0.5×10^{-4}) indicating a threshold <3.3 wt.% Cl in rock. This performance on Mars is similar to laboratory studies that estimate a detection threshold of 3-6 wt.% Cl (D. Anderson et al., 2017) and >3 wt.% Cl (Gaft et al., 2014).

Through mission sol 2127, we examined all APXS data and all ChemCam spectra to identify targets containing Cl using the normalized Cl peak area. Then, using visual analysis of RMI and Mastcam images, we classified the targets as rock, soil, or diagenetic (veins or nodules) and localized them along the traverse and within Mt. Sharp geologic units (Figure 1). To estimate the grain size of ChemCam bedrock targets, we used the Gini index mean score, a composition-based grain-size proxy that uses point-to-point chemical variabilities in

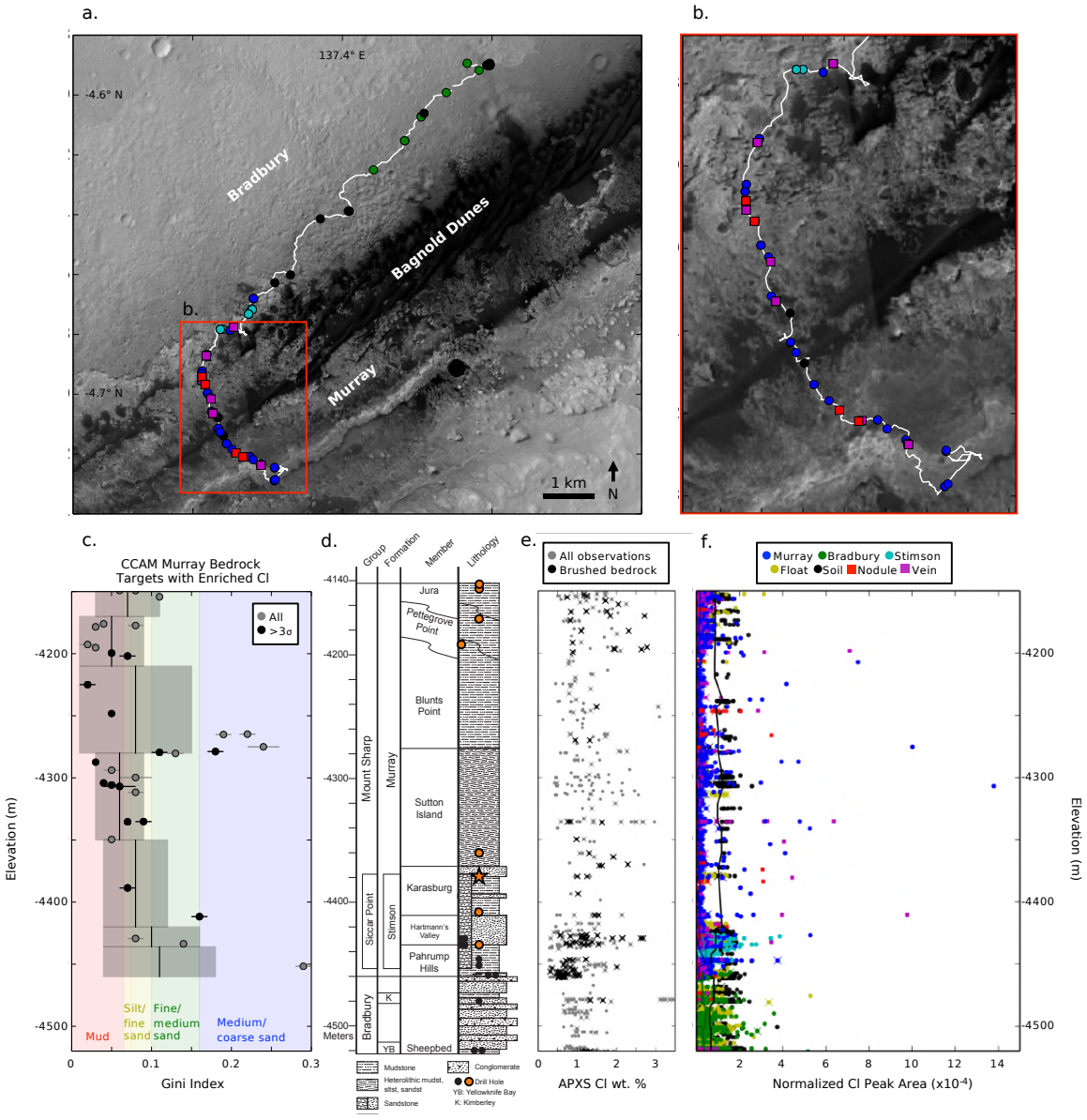

Figure 1. (a-b) MSL traverse map showing the locations of ChemCam targets defined as Cl detections (Cl ≥ 2×10^{-4} normalized peak area; or ≥ three-sigma above the mean peak area) color-coded by target type. (c) Gini index values for bedrock three-sigma Cl detections (black) and weaker Cl peaks (gray), which represent different grain size categories. Gini index mean (central line) and standard deviation (shaded bars) are reported for each member of Murray formation. (d) Gale crater stratigraphic column (Fedo et al., 2017) with drill sites,

colored orange where no perchlorates are detected using SAM (Archer et al., 2019). CheMin detects halite at the Quela drill target (orange star) (Achilles, 2018). (e) APXS-measured Cl wt. % for all targets (gray) and brushed (relatively dust-free) bedrock targets (black). (f) ChemCam normalized Cl peak area measurements. The lines show the moving average for the Murray bedrock (blue), Bradbury bedrock (green), and soil (black) points. Crosses indicate targets in common between APXS (e) and ChemCam (f).

ChemCam data (Rivera-Hernández et al., 2019), excluding points on or near diagenetic features.

3. Results

We observe Cl in all target types – soils, float rocks, bedrock, and diagenetic features (Figure 1). In soils the ChemCam Cl peak area varies little along the traverse, consistent with data from APXS showing ~1 wt.% Cl (Figure 1d) (see also O'Connell-Cooper et al., 2017). Most soils have normalized Cl peak areas of ~1-2×10^{-4} (Figure 1e). Direct comparison of soil and rock Cl peak areas is complicated by physical matrix effects (e.g., Rapin et al., 2017b; Thomas et al., 2018; and references therein), so it is unlikely they represent the same wt.% Cl, but characterizing relative variation is a useful benchmark. The Cl peak area moving average of soils is roughly constant with elevation along the traverse and 3× higher than the average bedrock, regardless of formation. Most rock, vein, and nodule points do not have Cl peaks significantly above zero, indicating <~3 wt.% Cl. APXS results show brushed bedrocks on average have 0.4 wt. % more Cl than soils.

Bedrock ChemCam Cl peak areas show much greater variability than soils. Average Cl peak area is higher (50%) in the Bradbury and Stimson formations than the Murray formation (Figure 1e), but in the Murray we observe more high Cl peak areas, three-sigma above the bedrock mean (≥ 2×10^{-4}). Stimson and Bradbury points have Cl peak areas up to 4×10^{-4};

whereas Murray points have values up to 14×10^{-4}. These very high Cl peak values occur in the Hartmann's Valley, Sutton Island, and Blunts Point members.

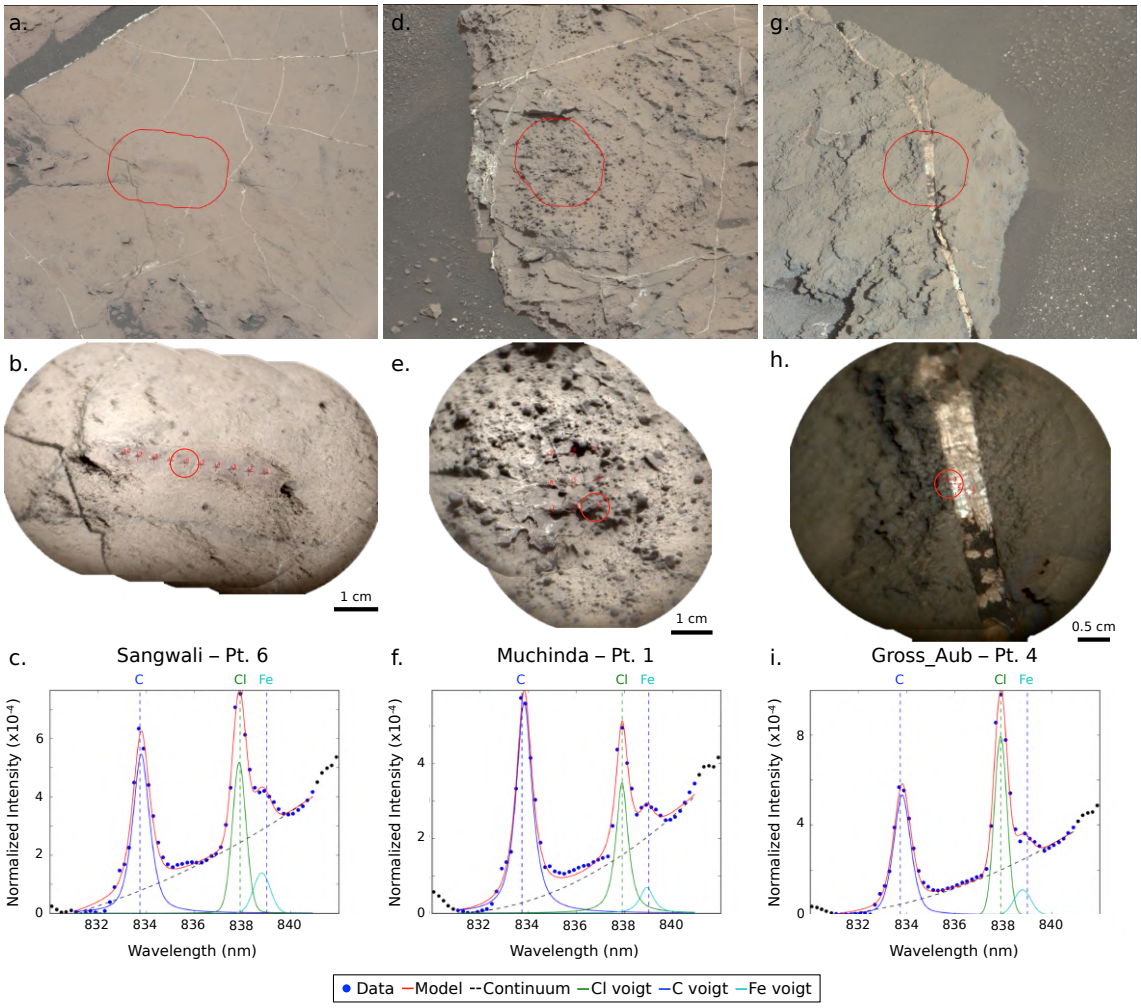

Figure 2. Mastcam (a, d, g) and RMI images (b, e, h) where Cl is detected including ChemCam spectra of the fit Cl peak at 838 nm (c, f, i). Circles indicate the raster point where Cl is observed. Example targets shown include: Sangwali, an isolated bedrock detection (a-c); Muchinda, a nodular detection (d-f); and Gross_Aub, a vein-related detection (g-i). (Mastcam images: mcam07482, mcam07156, and mcam05881).

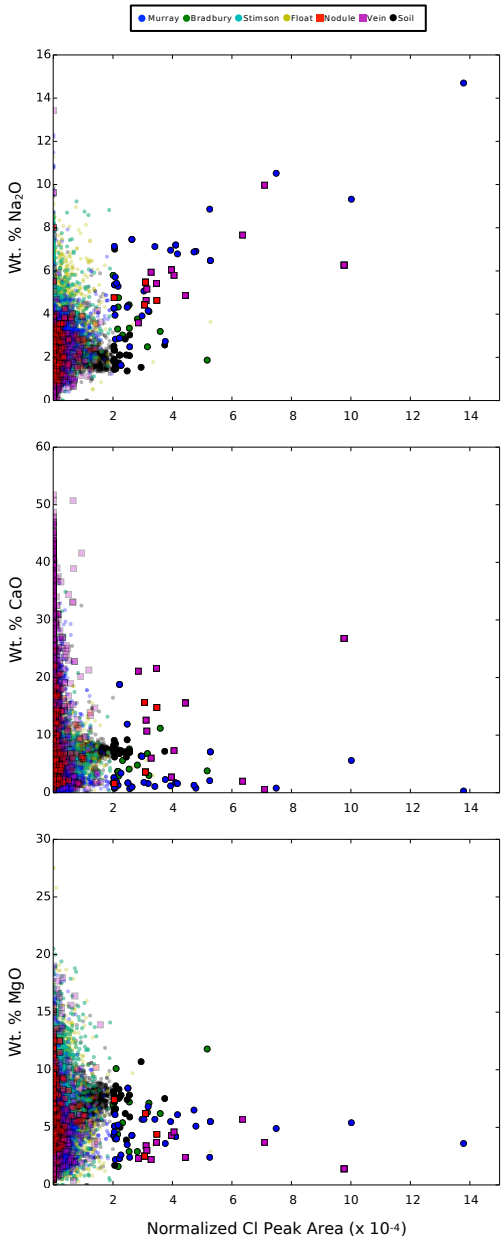

Figure 3. Normalized Cl peak area versus wt.% Na_2O, CaO, and MgO from ChemCam MOC. The opacity indicates the significance of the Cl observation. Fully opaque data points are three-sigma Cl detections ($\geq 2x10^{-4}$ Cl peak area). No correlation is seen for CaO and MgO.

The high ChemCam Cl observations (110 points) most frequently occur in isolated bedrock points (Figure 1e); i.e., a single point within a raster (covering ~3cm) contains a clear Cl peak (Figure 2c), but does not show textural or color differences compared to the nearby bedrock points without Cl (Figure 2ab). Other detections are vein-related, where Cl is most often detected at the edge of the Ca-sulfate vein and the nearby bedrock (Figure 2gh). In three cases Cl is seen in dark-toned inclusions in veins (L'Haridon et al., 2018), and in one case Cl is seen within a vein (target Third_White_Ash). We have also detected Cl in targets with nodular, resistant textures (Figure 2de). For the majority of targets (~50%), the Cl peak in shot-to-shot profiles stays constant, but for 10 Murray points, the Cl peak increased to a maximum in the middle of the shot profile indicating that an isolated Cl-rich grain or cement was measured.

Comparing the Murray bedrock targets containing high Cl with the Gini index mean score (Rivera-Hernández et al., 2019) for each member of the Murray formation, we find that Cl detections occur more commonly in mudstones, siltstones, and fine sandstones relative to coarser grained rocks (Figure 1c). Cl detections in coarser sandstone occur at the Sutton Island and Blunts Point boundary. There are more rocks with high Cl higher stratigraphically, with units from the Sutton Point member onward having a greater number of high Cl points.

We observe a positive correlation between normalized Cl peak area and wt.% Na_2O (Figure 3) and no apparent correlations between Cl peak area and wt.% CaO or MgO except for vein-related targets where CaO enrichment is expected from mixing with the Ca-sulfate vein (Figure 3). The Na wt.%-Cl peak area correlation is most apparent for the Murray formation bedrock and vein-related detections. The correlation suggests sodium chloride (NaCl), chlorate ($NaClO_3$), or perchlorate ($NaClO_4$) composition. We do not observe a correlation between O and Cl, so Na-chlorate or -perchlorate may be less likely, although LIBS data may not be very sensitive to variation in target O content (e.g., Schröder et al., 2019).

4. Discussion

4.1 Mineralogy

In bedrock, Cl peak areas are typically lower than the ChemCam detection threshold of ~3 wt.%, consistent with APXS brushed bedrock measurements showing on average 1.2 wt.% Cl (Figure 1d; O'Connell-Cooper et al, 2017). ChemCam observes considerable Cl variation to higher values in the Murray formation bedrock (Figure 1e). We interpret the bedrock high Cl to be due to sporadic occurrences of chloride grains and/or cements within the bedrock. There is not an obvious correlation with texture or morphology in bedrock; detections are scattered.

The chloride is most likely NaCl, halite, based on the correlation between Cl and Na observed by ChemCam, and supporting data from CheMin and SAM. For the Quela drill target (star, Figure 1), where ChemCam measures a Cl peak in one point of the drill tailings (peak area 8×10^{-4}), CheMin reports 0.3 ± 0.1 wt.% bulk halite (Achilles, 2018). The Sample Analysis at Mars Evolved Gas Analyzer (SAM-EGA) measured O_2 release below 600º C has been interpreted as perchlorate (Sutter et al., 2017). Starting at the Oudam drill target (sol 1364, elevation -4435 m), Cl observed by APXS is no longer interpreted as perchlorate/chlorate because the <600º C O_2 release disappears (Figure 1c; Archer et al., 2019). Therefore, in the upper Murray, the Cl present measured by APXS is in the form of chlorides.

4.2 Quantification of chlorine and halite

ChemCam Cl peak area values have associated uncertainty from fitting the normalized spectra with an automated routine. The fit quadratic continuum sometimes cuts into the Cl peak which could cause underestimation of the area. Additionally, a nearby minor Ti emission line (838.5 nm) that we do not fit could occasionally cause Cl peak area overestimation. Based on the outputs from the Levenberg-Marquardt fit, the error in the fit Cl peak area, calculated by taking the square root of the diagonal elements of the covariance matrix, is <8%.

To constrain how much Cl high ChemCam peak areas represent, we applied the data processing methodologies described in §2 to ChemCam lab model instrument measurements of Cl-bearing samples (described in D. Anderson et al., 2017; Thomas et al., 2018). We tested

normalization to the detector intensity and to C 248 nm, C 834 nm, and O 778 nm peak areas. Due to differences in experimental conditions, translating the laboratory calibrations to Mars requires an Earth-to-Mars correction (Clegg et al., 2017). Because of large, wavelength-dependent variability in the correction factor in the Cl wavelength region (831-841 nm), multiplying the lab data by this correction produced considerable variability in spectral shape and a more complicated continuum. Therefore, we multiplied the fit normalized Cl peak area by the average Earth-to-Mars correction in the Cl wavelength region. All normalizations were tested and calibration curve fits were varied (linear, quadratic), resulting in a large range of 14.9-42.3 wt. % Cl for point 4 of the bedrock target named aegis_post_1612a, which has the highest fit Cl peak area. Given qualitative examination of the spectra in comparison to laboratory mixtures of halite and basalt and the reported wt.% total of major oxides from partial least squares (81.3 wt.% total) for this observation point, high Cl values, i.e., much greater than >20 wt.% Cl, are likely unrealistic. Future studies may refine the Cl quantification approach for Mars. As an additional constraint, assuming halite stoichiometry, using the ChemCam measured wt.% Na_2O (14.7 +/ 1.5 wt.%), and subtracting an assumed Murray bedrock component (2.3-3.1 wt.% Na_2O), we predict 13.8 ± 2.2 wt.% Cl. This is on the lower end of the laboratory prediction. Thus, overall, the highest Cl point is estimated to result from ~15 wt. Cl or ~25 wt. % halite, possibly with additional Cl associated with other phases.

4.3 Emplacement models and implications

Because our highest Cl observation corresponds to ~25 wt.% halite in bedrock, we are not observing pure halite at the LIBS scale of 350-550 µm. Instead we are observing a mixture of bedrock and salt. For bedrock with chloride-filled pores, ~25 wt.% chloride at ChemCam LIBS scale might be expected. Porosities of 20-40% are typical for fine-grained sediments, though up to 80% porosity is possible for very fine, poorly consolidated mudstones (Fleury and Brosse, 2019). Because bedrock Cl detections are mostly in rocks with grainsizes less than the LIBS spot size, this implies either: (1) there are large grains of halite (diameter >~

150 μm; larger than typical bedrock grainsize) that fill up >~ 25 area % of the LIBS spot or (2) halite is a cement that in certain portions of the rock occupies all or part of the pore space.

The Sutton Island member of the Murray formation, where many potential chloride observations occur, is a package of heterolithic mudstones and sandstones likely deposited in lake and lake-margin environments dominated by suspension fallout with less common traction deposits (Fedo et al., 2018). Bedrock enrichments of >30 wt.% Ca and Mg sulfates in Sutton Island and Blunts Point suggest some of the beds may have formed in salty waters concentrated by evaporation (Rapin et al., 2019; submitted). Concretions and vertical and cross-cutting Ca-sulfate veins are common in the Sutton Island member and suggest late diagenesis (Fedo et al., 2018; Rapin et al., 2019; submitted). We find Cl associated with high Na_2O at the boundaries of some of the Ca-sulfate veins observed in the Murray.

Fluids on Mars produced by basaltic weathering are typically Cl-bearing and precipitate chloride salts during evaporation (Tosca and McLennan, 2006). In Gale crater, halite may have been emplaced initially as evaporitic salt layers, as mixed siliciclastic-salt beds from evapo-concentration of near-surface waters, or during later diagenetic processes. Gasda et al. (2017) suggests that successive layers of chloride, sulfate, and borate salts were emplaced occasionally during the deposition of Mt. Sharp. Large-scale and small-scale continuous beds of primary evaporite sequences have not been observed thus far by *Curiosity*, but sulfate layers remain to be explored (Milliken et al., 2010). As Mars transitioned to a drier climate, the Gale crater basin could have been analogous to a saline playa lake where acidic surface waters and alkaline groundwaters interacted to deposit clays and sulfates (Baldridge et al., 2009). Alternatively, Gale could represent a perennial lake system, which experienced multiple wet-dry cycles where evaporite-enriched deposits formed between mudstone deposits at the surface or in the shallow subsurface (Eugster and Hardie, 1978). Another alternative is that the chlorides precipitated from Cl-rich brines during diagenetic processes with Cl derived from evaporation of fluids from thin layers now completely dissolved or layers yet-to-be encountered higher in the strata (e.g., Handford, 1991).

While it is difficult to determine the original halite emplacement mechanism with the available data, the occurrence of halite in particular fine-grained members of the Murray suggests Cl-rich brines were associated with these units specifically. Complementary lines of evidence such as desiccation features in the Murray (Stein et al., 2018), scattered thin beds enriched in sulfates (Rapin et al., 2019; submitted), as well as the heterolithic mudstones and sandstones observed in the Sutton Island member, suggest evaporation in a near-shore environment may have been the initial halite source. The concentration of initial small-scale primary deposits of chlorides to the Sutton Island and Blunts Point members of the Murray formations suggests a transition in the Gale crater paleoenvironment and constrains later Gale lake waters to be episodically saline.

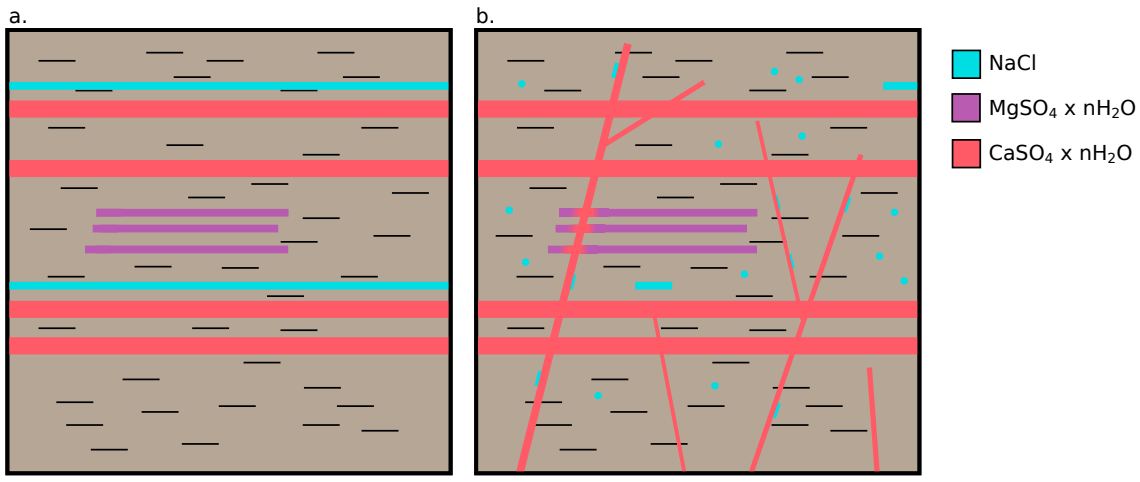

Figure 4. Potential emplacement scenario for chloride salts in the Murray formation. First, (a) halite (blue), Mg-sulfates (purple), and Ca-sulfates (red) enrichments form via evaporation of lake waters within siliclastics. Then, (b) sulfate-bearing groundwaters precipitate additional Ca-sulfates and mostly dissolve the halite, which reprecipitates as isolated grains or cements in the bedrock, in altered, nodular textures in the bedrock, and at the boundaries of Ca-sulfate veins (red).

Halite is highly soluble and one of the easiest salts to later mobilize. We see a small number of halite detections most often as isolated enrichment points in bedrock targets, associated with Ca-sulfate veins, or in nodular textures. Together, these observations are most consistent with reworking and remobilization by later groundwater (Figure 5). Following compaction and lithification of the Murray formation, late diagenetic fluids mobilized highly soluble salts like halite. The diagenetic fluids were likely SO_4 rich as they readily mobilized halite, mobilized Mg-sulfate only to a limited degree (Rapin et al., 2019; submitted), and precipitated many Ca-sulfate veins. These late-stage fluids deposited Ca-sulfates within fractures as well as chloride salts at vein margins. If the pressure from Ca-sulfate precipitation forced fractures open as suggested by other analyses (Caswell and Milliken, 2017), halite would have precipitated last. Alternatively, the location on the edges of the fractures could also be consistent with a second fluid event after further fracturing between the bedrock and Ca-sulfate vein. The nodular textures containing halite clearly represent diagenetic emplacement but the scattered, isolated bedrock detections are either remnants of where halite was emplaced initially or pore space where salts precipitated from later diagenetic fluids.

5. Conclusions

We present the first systematic study of chlorine and models for its emplacement in Gale crater using MSL instruments. APXS measures Cl in bedrock and soils at 0.28-3.44 wt.% Cl. Cl is detected with the 838 nm peak in ChemCam targets. Cl peaks are found in most soils. Most bedrock, vein, and nodule targets have no Cl at the ChemCam detection limit of ~3 wt.%, but sporadic occurrences of Cl are occasionally present in all these target types. For bedrock, the average Cl peak is higher in the Bradbury and Stimson formations than the Murray formation; however, the Murray contains isolated detections of high Cl ($\geq$ 15 wt.% Cl). These correlate with high wt.% Na_2O (~15 wt.%) and likely represent ~25 wt.% halite salt. CheMin detection of halite and SAM analyses, which indicate the presence of chlorides, corroborate halite. In addition to bedrock, halite is also detected in the Murray in nodular textures as well as at the outer boundaries of Ca-sulfate veins. Halite bedrock detections

occur in all stratigraphic intervals but the highest values are in the Sutton Island, Blunts Point, Pettegrove Point, and Jura members. Given the solubility of halite and sporadic nature of its detection, we are likely observing halite emplaced by later groundwater reworking and remobilization of initial deposits. The restriction of high Cl to specific members of the Murray formation may suggest initial small-scale primary deposits of chlorides, specific to these units, were locally remobilized by the fluids that precipitated Ca-sulfates. Primary evaporitic chloride layers have not been observed thus far, but the concentration of deposits in particular members suggests an interval of more saline depositional waters and changes in the Gale crater paleoenvironment.

References

Achilles, C. N. (2018). Analyses of crystalline and X-ray amorphous materials in Gale crater rocks and soils, (Doctoral dissertation). University of Arizona Open Repository.

Anderson, D. E., Ehlmann, B. L., Forni, O., Clegg, S. M., Cousin, A., Thomas, N. H., et al. (2017). Characterization of LIBS emission lines for the identification of chlorides, carbonates, and sulfates in salt/basalt mixtures for the application to MSL ChemCam data. *Journal of Geophysical Research: Planets, 122*(4), 744–770. http://doi.org/10.1002/2016JE005164

Anderson, R. B., Clegg, S. M., Frydenvang, J., Wiens, R. C., McLennan, S., Morris, R. V., et al. (2017). Improved accuracy in quantitative laser-induced breakdown spectroscopy using sub-models. *Spectrochimica Acta Part B, 129*, 49-57. http://doi.org/10.1016/j.sab.2016.12.002

Archer, P. D., Ming, D. W., Sutter, B., Hogancamp, J. V., Morris, R. V., Clark, B. C., et al. (2019). *Oxychlorine Detection in Gale Crater, Mars and Implications for Past Environmental Conditions*. Paper presented at 50th Lunar and Planetary Science Conference, The Woodlands, TX (p. 3041).

Baldridge, A. M., Hook, S. J., Crowley, J. K., Marion, G. M., Kargel, J. S., Michalski, J. L., et al. (2009). Contemporaneous deposition of phyllosilicates and sulfates: Using Australian acidic saline lake deposits to describe geochemical variability on Mars. *Geophysical Research Letters, 36*(19), L19201. http://doi.org/10.1029/2009GL040069

Berger, J. A., Schmidt, M. E., Gellert, R., Campbell, J. L., King, P. L., Flemming, R. L., et al. (2016). A global Mars dust composition refined by the Alpha-Particle X-ray Spectrometer in Gale Crater. *Geophysical Research Letters, 43*(1), 67–75. http://doi.org/10.1002/2015GL066675

Bridges, J. C., & Grady, M. M. (2000). Evaporite mineral assemblages in the nakhlite (martian) meteorites. *Earth and Planetary Science Letters, 176*(3–4), 267–279. http://doi.org/https://doi.org/10.1016/S0012-821X(00)00019-4

Bristow, T. F., Rampe, E. B., Achilles, C. N., Blake, D. F., Chipera, S. J., Craig, P., et al. (2018). Clay mineral diversity and abundance in sedimentary rocks of Gale crater, Mars. *Science Advances, 4*(6), eaar3330. http://doi.org/10.1126/sciadv.aar3330

Caswell, T. E., & Milliken, R. E. (2017). Evidence for hydraulic fracturing at Gale crater, Mars: Implications for burial depth of the Yellowknife Bay formation. *Earth and Planetary Science, 468,* 72-84. http://doi.org/10.1016/j.epsl.2017.03.033

Clark, B. C., Morris, R. V., McLennan, S. M., Gellert, R., Jolliff, B., Knoll, A. H., et al. (2005). Chemistry and mineralogy of outcrops at Meridiani Planum. *Earth and Planetary Science Letters, 240*(1), 73–94. http://doi.org/10.1016/j.epsl.2005.09.040

Clegg, S. M., Wiens, R. C., Anderson, R., Forni, O., Frydenvang, J., Lasue, J., et al. (2017). Recalibration of the Mars Science Laboratory ChemCam instrument with an expanded geochemical database. *Spectrochimica Acta Part B: Atomic Spectroscopy, 129,* 64–85. http://doi.org/10.1016/j.sab.2016.12.003

Cousin, A., Dehouck, E., Meslin, P.-Y., Forni, O., Williams, A. J., Stein, N., et al. (2017). Geochemistry of the Bagnold dune field as observed by ChemCam and comparison with other aeolian deposits at Gale Crater. *Journal of Geophysical Research: Planets*, *122*(10), 2144–2162. http://doi.org/10.1002/2017JE005261

Diez, B., Feldman, W. C., Mangold, N., Baratoux, D., Maurice, S., Gasnault, O., et al. (2009). Contribution of Mars Odyssey GRS at Central Elysium Planitia. *Icarus*, *200*(1), 19–29. http://doi.org/10.1016/j.icarus.2008.11.011

Ehlmann, B. L., Edgett, K. S., Sutter, B., Achilles, C. N., Litvak, M. L., Lapotre, M. G. A., et al. (2017). Chemistry, mineralogy, and grain properties at Namib and High dunes, Bagnold dune field, Gale crater, Mars: A synthesis of Curiosity rover observations. *Journal of Geophysical Research: Planets*, *122*(12), 2510–2543. http://doi.org/10.1002/2017JE005267

Ehlmann, B. L., & Buz, J. (2015). Mineralogy and fluvial history of the watersheds of Gale, Knobel, and Sharp craters: A regional context for the Mars Science Laboratory Curiosity's exploration. *Geophysical Research Letters*, *42*(2), 264–273. http://doi.org/10.1002/2014GL062553

Eugster, H. P., & Hardie, L. A. (1978). Saline Lakes. In *Lakes*. Springer, New York, NY, pp. 273-293.

Fedo, C. M., Grotzinger, J. P., Gupta, S., Fraeman, A. A., Edgar, L., Edgett, K., et al. (2018). *Sedimentology and Stratigraphy of the Murray Formation, Gale Crater, Mars.* Paper presented at 49th Lunar and Planetary Science Conference, The Woodlands, TX (p. 2083).

Fleury, M., & Brosse, E. (2019). Transport in Tight Rocks. In Geological Carbon Storage: Subsurface Seals and Caprock Integrity, Geophysical Monograph, 238, pp. 31-43.

Forni, O., Gaft, M., Toplis, M. J., Clegg, S. M., Maurice, S., Wiens, R. C., et al. (2015). First detection of fluorine on Mars: Implications for Gale Crater's geochemistry. *Geophysical Research Letters*, *42*(4), 1020–1028. http://doi.org/10.1002/2014GL062742

Gaft, M., Nagli, L., Eliezer, N., Groisman, Y., & Forni, O. (2014). Elemental analysis of halogens using molecular emission by laser-induced breakdown spectroscopy in air. *Spectrochimica Acta Part B: Atomic Spectroscopy*, *98*, 39–47. http://doi.org/10.1016/j.sab.2014.05.011

Gasda, P. J., Haldeman, E. B., Wiens, R. C., Rapin, W., Bristow, T. F., Bridges, J. C., et al. (2017). In situ detection of boron by ChemCam on Mars. *Geophysical Research Letters*, *44*(17), 8739–8748. http://doi.org/10.1002/2017GL074480

Gellert, R., Rieder, R., Anderson, R. C., Bruckner, J., Clark, B. C., Dreibus, G., et al. (2004). Chemistry of Rocks and Soils in Gusev Crater from the Alpha Particle X-ray Spectrometer. *Science*, 305(5685), 829-833. http://doi.org/10.1126/science.1099913

Gellert, R., Rieder, R., Bruckner, J., Clark, B. C., Dreibus, G., Klingelhofer, G., et al. (2006). Alpha Particle X-Ray Spectrometer (APXS): Results from Gusev crater and calibration report. *Journal of Geophysical Research: Planets*, 111(E2), E02S05, http://doi.org/10.1029/2005JE002555

Grotzinger, J. P., Gupta, S., Malin, M. C., Rubin, D. M., Schieber, J., Siebach, K., et al. (2015). Deposition, exhumation, and paleoclimate of an ancient lake deposit, Gale crater, Mars. *Science*, *350*(6257), aac7575-aac7575. http://doi.org/10.1126/science.aac7575

Handford, C. R. (1991). Marginal Marine Halite: Sabkhas and Salinas. *Developments in Sedimentology*, 50, 1-66.

Haskin, L. A., Wang, A., Jolliff, B. L., McSween, H. Y., Clark, B. C., Des Marais, D. J., et al. (2005). Water alteration of rocks and soils on Mars at the Spirit rover site in Gusev crater. *Nature*, *436*(7047), 66–69. http://doi.org/10.1038/nature03640

Hecht, M. H., Kounaves, S. P., Quinn, R. C., West, S. J., Young, S. M. M., Ming, D. W., et al. (2009). Detection of Perchlorate and the Soluble Chemistry of Martian Soil at the Phoenix Lander Site. *Science*, *325*(5936), 64–67. http://doi.org/10.1126/science.1172466

Hurowitz, J. A., Grotzinger, J. P., Fischer, W. W., McLennan, S. M., Milliken, R. E., Stein, N., et al. (2017). Redox stratification of an ancient lake in Gale crater, Mars. *Science*, *356*(6341), eaah6849. http://doi.org/10.1126/science.aah6849

Knoll, A. H., Jolliff, B. L., Farrand, W. H., Bell III, J. F., Clark, B. C., Gellert, R., et al. (2008). Veneers, rinds, and fracture fills: Relatively late alteration of sedimentary rocks at Meridiani Planum, Mars. *Journal of Geophysical Research*, *113*(E6), E06S16. http://doi.org/10.1029/2007JE002949

L'Haridon, J., Mangold, N., Meslin, P.-Y., Johnson, J. R., Rapin, W., Forni, O., et al. (2018). Chemical variability in mineralized veins observed by ChemCam on the lower slopes of Mount Sharp in Gale crater, Mars. *Icarus*, *311*, 69–86. http://doi.org/10.1016/j.icarus.2018.01.028

Lanza, N. L., Fischer, W. W., Wiens, R. C., Grotzinger, J., Ollila, A. M., Cousin, A., et al. (2014). High manganese concentrations in rocks at Gale crater, Mars. *Geophysical Research Letters*, *41*(16), 5755–5763. http://doi.org/10.1002/2014GL060329

Lasue, J., Cousin, A., Meslin, P.-Y., Mangold, N., Wiens, R. C., Berger, G., et al. (2018). Martian Eolian Dust Probed by ChemCam. *Geophysical Research Letters*, *45*(20), 10,968-10,977. http://doi.org/10.1029/2018GL079210

Léveillé, R. J., Bridges, J., Wiens, R. C., Mangold, N., Cousin, A., Lanza, N., et al. (2014). Chemistry of fracture-filling raised ridges in Yellowknife Bay, Gale Crater: Window into past aqueous activity and habitability on Mars. *Journal of Geophysical Research: Planets*, *119*(11), 2398–2415. http://doi.org/10.1002/2014JE004620

Lisov, D. I., Litvak, M. L., Kozyrev, A. S., Mitrofanov, I. G., & Sanin, A. B. (2018). Data Processing Results for the Active Neutron Measurements by the DAN Instrument on the Curiosity Mars Rover. *Astronomy Letters*, *44*(7), 482–489. http://doi.org/10.1134/S1063773718070034

Litvak, M. L., Mitrofanov, I. G., Hardgrove, C., Stack, K. M., Sanin, A. B., Lisov, D., et al. (2016). Hydrogen and chlorine abundances in the Kimberley formation of Gale crater measured by the DAN instrument on board the Mars Science Laboratory Curiosity rover. *Journal of Geophysical Research: Planets*, *121*(5), 836–845. http://doi.org/10.1002/2015JE004960

Maurice, S., Wiens, R. C., Saccoccio, M., Barraclough, B., Gasnault, O., Forni, O., et al. (2012). The ChemCam Instrument Suite on the Mars Science Laboratory (MSL) Rover: Science Objectives and Mast Unit Description. *Space Science Reviews*, *170*(1–4), 95–166. http://doi.org/10.1007/s11214-012-9912-2

Milliken, R. E., Grotzinger, J. P., & Thomson, B. J. (2010). Paleoclimate of Mars as captured by the stratigraphic record in Gale Crater. *Geophysical Research Letters*, *37*(4), 1–6. http://doi.org/10.1029/2009GL041870

Ming, D. W., Mittlefehldt, D. W., Morris, R. V., Golden, D. C., Gellert, R., Yen, A., et al. (2006). Geochemical and mineralogical indicators for aqueous processes in the Columbia Hills of Gusev crater, Mars. *Journal of Geophysical Research: Planets*, *111*(E2), n/a-n/a. http://doi.org/10.1029/2005JE002560

Nachon, M., Clegg, S. M., Mangold, N., Schröder, S., Kah, L. C., Dromart, G., Ollila, A., et al. (2014). Calcium sulfate veins characterized by ChemCam/Curiosity at Gale

crater, Mars. *Journal of Geophysical Research: Planets,* 111(9), 1991-2016. http://doi.org/10.10002/2013JE004588.

O'Connell-Cooper, C. D., Spray, J. G., Thompson, L. M., Gellert, R., Berger, J. A., Boyd, N. I., et al. (2017). APXS-derived chemistry of the Bagnold dune sands: Comparisons with Gale Crater soils and the global Martian average. *Journal of Geophysical Research: Planets, 122*(12), 2623–2643. http://doi.org/10.1002/2017JE005268

Ollila, A. M., Newsom, H. E., Clark, B., Wiens, R. C., Cousin, A., Blank, J. G., et al. (2014). Trace element geochemistry (Li, Ba, Sr, and Rb) using Curiosity 's ChemCam: Early results for Gale crater from Bradbury Landing Site to Rocknest. *Journal of Geophysical Research: Planets, 119*(1), 255–285. http://doi.org/10.1002/2013JE004517

Osterloo, M. M., Anderson, F. S., Hamilton, V. E., & Hynek, B. M. (2010). Geologic context of proposed chloride-bearing materials on Mars. *Journal of Geophysical Research, 115*(E10), E10012. http://doi.org/10.1029/2010JE003613

Payré, V., Fabre, C., Cousin, A., Sautter, V., Wiens, R. C., Forni, O., et al. (2017). Alkali trace elements in Gale crater, Mars, with ChemCam: Calibration update and geological implications. *Journal of Geophysical Research: Planets, 122*(3), 650–679. http://doi.org/10.1002/2016JE005201

Rapin, W., Meslin, P.-Y., Maurice, S., Wiens, R. C., Laporte, D., Chauviré, B., et al. (2017a). Quantification of water content by laser induced breakdown spectroscopy on Mars. *Spectrochimica Acta Part B: Atomic Spectroscopy, 130*, 82–100. http://doi.org/10.1016/j.sab.2017.02.007

Rapin, W., Bousquet, B., Lasue, J., Meslin, P.-Y., Lacour, J.-L., Fabre, C., et al. (2017b). Roughness effects on the hydrogen signal in laser-induced breakdown spectroscopy. *Spectrochimica Acta Part B: Atomic Spectroscopy, 137*, 13-22. http://doi.org/10.1016/j.sab.2017.09.003

Rapin, W., Ehlmann, B. L., Dromart, G., Schieber, J., Thomas, N. H., Fischer, W. W., et al. (2019). *High Salinity Recorded by Bedrock Sulfate Enrichments at Gale Crater*. Paper presented at 50th Lunar and Planetary Science Conference, The Woodlands, TX (p. 2147).

Rivera-Hernández, F., Sumner, D. Y., Mangold, N., Stack, K. M., Forni, O., Newsom, H., et al. (2019). Using ChemCam LIBS data to constrain grain size in rocks on Mars: Proof of concept and application to rocks at Yellowknife Bay and Pahrump Hills, Gale crater. *Icarus*, *321*(October 2018), 82–98. http://doi.org/10.1016/j.icarus.2018.10.023

Schröder, S., Rammelkamp, K., Vogt, D. S., Gasnault, O., & Hubers, H.-W. (2019). Contribution of a martian atmosphere to laser-induced breakdown spectroscopy (LIBS) data and testing its emission characteristics for normalization applications. Icarus, 325, 1-15. http://doi.org/10.1016/j.icarus.2019.02.017

Stein, N., Grotzinger, J. P., Schieber, J., Mangold, N., Hallet, B., Newsom, H., et al. (2018). Desiccation cracks provide evidence of lake drying on Mars, Sutton Island member, Murray formation, Gale Crater. *Geology*, *46*(6), 515–518. http://doi.org/10.1130/G40005.1

Sutter, B., McAdam, A. C., Mahaffy, P. R., Ming, D. W., Edgett, K. S., Rampe, E. B., et al. (2017). Evolved gas analyses of sedimentary rocks and eolian sediment in Gale Crater, Mars: Results of the Curiosity rover's sample analysis at Mars instrument from Yellowknife Bay to the Namib Dune. *Journal of Geophysical Research: Planets*, *122*(12), 2574–2609. http://doi.org/10.1002/2016JE005225

Thomas, N. H., Ehlmann, B. L., Anderson, D. E., Clegg, S. M., Forni, O., Schröder, S., et al. (2018). Characterization of Hydrogen in Basaltic Materials with Laser-Induced Breakdown Spectroscopy (LIBS) for Application to MSL ChemCam Data. *Journal of*

Geophysical Research: Planets, *123*(8), 1996–2021. http://doi.org/10.1029/2017JE005467

Tosca, N. J., & McLennan, S. M. (2006). Chemical divides and evaporite assemblages on Mars. *Earth and Planetary Science Letters*, *241*(1–2), 21–31. http://doi.org/10.1016/j.epsl.2005.10.021

Vaniman, D., Dyar, M. D., Wiens, R., Ollila, A., Lanza, N., Lasue, J., et al. (2012). Ceramic ChemCam calibration targets on Mars Science Laboratory. *Space Science Reviews*, *170*(1–4), 229–255. http://doi.org/10.1007/s11214-012-9886-0

Vogt, D. S., Rammelkamp, K., Schröder, S., & Hübers, H. W. (2018). Molecular emission in laser-induced breakdown spectroscopy: An investigation of its suitability for chlorine quantification on Mars. *Icarus*, *302*(2018), 470–482. http://doi.org/10.1016/j.icarus.2017.12.006

Wiens, R. C., Maurice, S., Lasue, J., Forni, O., Anderson, R. B., Clegg, S., … Vaniman, D. (2013). Pre-flight calibration and initial data processing for the ChemCam laser-induced breakdown spectroscopy instrument on the Mars Science Laboratory rover. *Spectrochimica Acta Part B: Atomic Spectroscopy*, *82*, 1–27. http://doi.org/10.1016/j.sab.2013.02.003

Wiens, R. C., Maurice, S., Barraclough, B., Saccoccio, M., Barkley, W. C., Bell, J. F., … Wong-Swanson, B. (2012). The ChemCam Instrument Suite on the Mars Science Laboratory (MSL) Rover: Body Unit and Combined System Tests. *Space Science Reviews*, *170*(1–4), 167–227. http://doi.org/10.1007/s11214-012-9902-4

Chapter 5

A SEARCH FOR SEDIMENTARY IRON FORMATIONS ON MARS USING CRISM FACTOR ANALYSIS AND TARGET TRANSFORMATION TECHNIQUES

N. H. Thomas[1], A. A. Fraeman[2], E. S. Amador[1,2], B. L. Ehlmann[1,2], J. L. Bandfield[3], and K. Stack Morgan[2]

[1] Division of Geological and Planetary Sciences, California Institute of Technology, Pasadena, California, USA.

[2] Jet Propulsion Laboratory, California Institute of Technology, Pasadena, California, USA.

[3] Space Science Institute, Boulder, Colorado, USA.

Abstract

Analogs to terrestrial iron formations are hypothesized to have formed at the martian surface by directly precipitating from the water column. Although previous studies have not found good analogs, a systematic survey of the higher resolution visible CRISM (Compact Reconnaissance Imaging Spectrometer for Mars) dataset has not yet been completed. We adapted and applied factor analysis and target transformation, a semi-automated technique, to search for hematite in Noachian- and Hesperian-aged stratified, candidate sedimentary outcrops previously identified. Only 3% of the images with stratified outcrops that we surveyed contain hematite. We confirm the presence of hematite in Mawrth Vallis, Iani Chaos and Meridiani Planum and report the detection of hematite in Nili Fossae. Given the geologic settings and mineral assemblages observed, all detections more likely precipitated from upwelling groundwaters or surface alteration fluids rather than in the water column. Therefore, analogs to terrestrial iron formations are not found on Mars, possibly due to differences between Earth and Mars in aqueous chemistry and availability. Future studies

using our methods can search for other Fe-phyllosilicates and Fe-sulfates and search for hematite in other geologic settings and locations.

1. Introduction

Iron phases in the sedimentary record, including oxides, oxyhydroxides, phyllosilicates, and sulfates, are useful for studying redox changes in aqueous geochemistry and atmospheric composition. On Earth, iron formations (> 15 wt. % Fe), iron-rich sedimentary rocks that formed primarily during the Archean Eon (~2.5-4 Ga), provide evidence for iron mobilization in a reducing atmosphere. The martian crust has a higher abundance of iron (~14 wt. %) than the Earth's crust (~8 wt. %) (Taylor and McLennan, 2009), and it has been hypothesized that analogs for Precambrian terrestrial iron formations could have formed on early Mars if a CO_2-rich, reducing atmosphere was present (Catling and Moore, 2003; King et al., 2004; King and McSween, 2005; Righter et al., 2008) and permitted transport of reduced iron, which subsequently oxidized (e.g., Bridges et al., 2008; Burns et al., 1993; Fallacaro and Calvin, 2006; Schaefer, 1996).

Previously, iron oxides have been observed on Mars in sedimentary outcrops by orbital and landed missions; however, these are not analogous to primary iron oxides in terrestrial iron formations. Gray, specular hematite has been detected in Meridiani Planum, Aureum Chaos, Iani Chaos, Aram Chaos, and at other locations associated with the interior layered deposits throughout Valles Marineris using the Thermal Emission Spectrometer (TES) (Christensen et al., 2000; Christensen et al., 2001; Glotch and Christensen, 2005; Glotch and Rogers, 2007; Weitz et al., 2008; Weitz et al., 2012). Finer grained red hematite has been detected by CRISM (Compact Reconnaissance Imaging Spectrometer for Mars) and OMEGA (Observatoire pour la Minéralogie, l'Eau, les Glaces et l'Activité) in the Valles Marineris interior layered deposits, chaos regions, and areas around Meridiani Planum (Bibring et al., 2007). Both of these types of deposits are associated with sulfates and are hypothesized to have formed through secondary diagenetic processes associated with regional groundwater upwelling (e.g., McLennan et al., 2005; Tosca and McLennan., 2006; Roach et al., 2010). In addition, hematite has been detected at Mawrth Vallis in association with Al-rich and

sometimes Fe/Mg phyllosilicate layers (Bishop et al., 2013; Wray et al., 2008) and may have formed from intense leaching processes. Gale crater provides an example where hematite detected in Mt. Sharp by orbital (Milliken et al., 2010; Fraeman et al., 2013) and in situ (Rampe et al., 2017) studies is hypothesized to be either a primary authigenic phase that precipitated from a redox stratified lake, a product of in situ oxidative weathering, or a secondary diagenetic product (Fraeman et al., 2013; 2016; Hurowitz et al., 2017; Rampe et al., 2017). Recent observations suggest that post-depositional processes, such as diagenesis and differential cementation were important in creating the topographic ridge and localizing the observed deep spectral absorptions.

The paucity of primary iron oxide sedimentary deposit candidates on Mars could mean that the hypothesized iron formations (Burns et al., 1993) did not form on early Mars, and/or that other Fe-bearing phases such as Fe-phyllosilicates or Fe-sulfates were favored. Alternatively, this could be an observational bias. On Earth, iron formations are uncommon. Limited, small deposits on Mars may be difficult to detect even with high resolution orbital data. High resolution CRISM data has been useful for determining the global distributions of secondary minerals such as phyllosilicates and carbonates using the ~1-2.5 μm wavelength range, but the shorter (~0.5-0.9 μm) wavelengths have been underutilized in comparison.

Here, we adapt and apply semi-automated survey methods in coordination with traditional CRISM analysis techniques to systematically search for the presence of hematite in a subset of stratified outcrops that are candidate sedimentary rocks (Stack, 2015). We identify hematite in 3% of the surveyed images in three regions of interest: Mawrth Vallis, Nili Fossae, and Iani Chaos and Meridiani Planum. We evaluate the performance of our methods, discuss potential emplacement mechanisms for the hematite discovered, and examine the implications for the lack of analogs to terrestrial iron formations.

2. Survey Methods

2.1 Compact Reconnaissance Imaging Spectrometer for Mars (CRISM)

CRISM is a hyperspectral visible and near-infrared imaging spectrometer with 544 spectral bands between ~0.4 and 4.0 μm (Murchie et al., 2007). CRISM observations are taken in several modes with different spectral and spatial resolutions. We used TRDR data products with reduced noise and striping characteristics (Seelos et al., 2011), taken in full-resolution targeted (FRT) and full-resolution short (FRS) sampling modes with a spatial sampling of 15-19 m/pixels for this project.

All CRISM data were atmospherically corrected using the "volcano scan" method as described by McGuire et al. (2009). The gas absorptions are removed using a scaled atmospheric transmission spectrum derived from an observation of Olympus Mons. Data are then converted to I/F, the ratio between the measured radiance and the solar irradiance divided by π steradians. Although the volcano scan correction greatly reduces the prominence of gas absorptions, residual absorptions may remain and the spectral effects of aerosols are not removed (Wiseman et al., 2010).

Ferric oxides have four characteristic absorptions in the visible portion of the spectrum caused by electronic ligand field transitions and charge transfers. Due to differences in absorption center caused by differences in the crystal structure, hematite is distinguishable from other iron oxides. Particularly, the absorption at 860 nm allows hematite to be identified using the CRISM dataset.

2.2 Factor Analysis and Target Transformation

Factor analysis and target transformation methods (Malinowski, 1991) enable semi-automated searches for a given spectral endmembers. These methods can be used to both identify the number of independent variable spectral components and test for the presence of individual endmembers from mixed spectral datasets. These methods have been extensively applied to laboratory and spacecraft thermal infrared (TIR) spectral data (Bandfield et al., 2000; Christensen et al., 2000; Bandfield et al., 2002; Hamilton and Ruff, 2012; Glotch and Bandfield, 2006; Glotch and Rogers, 2013; Geminale et al., 2015). Recently, Thomas and Bandfield (2017) adapted factor analysis and target transformation for near infrared (NIR)

CRISM data, and Amador et al. (2018) applied their methods to perform a global search for minerals associated with serpentinization.

We use mean-removed R-mode factor analysis, which uses a set of mixed spectra to derive a set of orthogonal eigenvectors and associated eigenvalues. The covariance-based data matrix factorization method used to transform the column-oriented data matrix (spectra) into eigenvectors and eigenvalues is described in depth by Malinowski (1991). The eigenvectors represent independent components present in the mixed data. These components do not individually or independently correspond to the data's physical components, such as endmember spectra. Eigenvalues indicate the variance of the data along the axis of the associated eigenvector. Because eigenvectors are defined by maximizing the variance along each axis in multidimensional data (as well as being orthogonal to the previous eigenvectors), each successive eigenvalue will be smaller than the previous one. The combined analysis of eigenvectors along with the associated eigenvalues provides a good indication of the number of independent components in a set of mixed spectra, and whether the eigenvectors represent real variation or spectral noise. Factor analysis differs from principal components analysis (PCA) as it is based on a generative model and focuses on the off-diagonal elements of the covariance matrix.

For this work, we apply factor analysis to data from the short wavelength (S) detector of CRISM (0.4-1.0 μm). Every 3rd pixel of every 3rd row was used to calculate 20 eigenvectors. Previous work (Thomas and Bandfield, 2017; Amador et al., 2018) has shown 10-12 eigenvectors are generally sufficient to represent all the independent components in a CRISM scene. Here, we choose a conservative number of eigenvectors (20) to capture all possible independent components which has the downside of potentially adding more spectral noise, present in higher eigenvectors.

In practice, target transformation is a linear least-squares fit of the significant eigenvectors to an endmember test spectrum. The spectral endmember can be a laboratory spectrum, a spectrum from another image, or a series of synthetic spectral shapes. If the test spectrum can be closely matched, then it is confirmed as a possible endmember present in the system.

We test goodness of fit by calculating the spectral angle distance (SAD) between our test and modeled spectra and by evaluating the quality of the fit by eye. Due to known artifacts in the CRISM radiometric calibration at VNIR wavelengths less than 410 nm, between 644 and 684 nm, and greater than 1023 nm (Murchie et al., 2009), these bands were removed from our SAD calculation. By visual inspection of the target transformation fits, we chose a cutoff of SAD < 0.045 as a threshold for detection. Modeled spectra with SAD values < 0.045 match the key hematite absorptions (Section 2.1) well with varying noise contributions, while none of the spectra with greater SAD values matched well enough visually to be considered hematite detections.

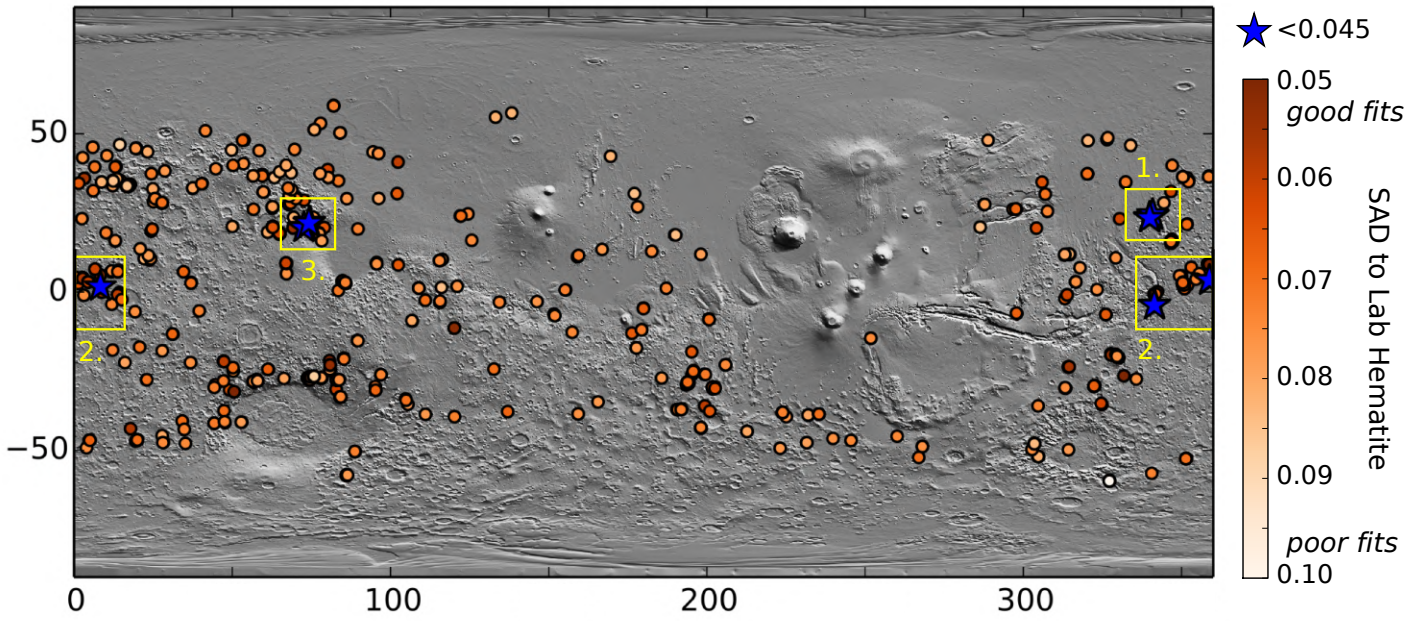

Figure 1. Global distribution of stratified, candidate sedimentary outcrops surveyed (points). The color bar indicates goodness of fit to a laboratory hematite endmember using target transformation. Lower SAD values are better fits, and SAD values below 0.045 (marked with stars) are considered candidate detections. Boxed areas are regions of interest shown in other figures: 1) Mawrth Vallis (Figure 3), 2) Iani Chaos and Meridiani Planum (Figure 4), and 3) Nili Fossae (Figure 5).

2.3 Candidate Sedimentary, Stratified Outcrops

Stack et al. (2015) examined over 17,000 images collected by the High Resolution Imaging Science Experiment (HiRISE) camera within ± 60° latitude of the martian equator, and identified 5,324 HiRISE images containing 5,781 unique stratified rock outcrops in four geomorphic settings: (1) impact craters, (2) canyons, (3) channels, and (4) plains. For this study, we focus on stratified basin fill deposits of presumed sedimentary origin. We selected 1,856 deposits because they appear to be topographically confined and include fills and mounds within craters, canyons, chasms, and channels. We do not include deposits categorized as viscous flow features (e.g., concentric crater fills, lobate debris aprons, or lineated valley fills) or stratified deposits associated with dissected mantle terrains that are likely periglacial in origin. We further narrow our search to only Noachian- and Hesperian-aged terrains (Tanaka et al., 2014) to coincide with when iron formations formed on early Earth and because this is the time period when Mars may have lost most of its atmosphere and experienced climate change. Ultimately, we are left with 653 HiRISE images covered by 726 CRIMS FRT and FRS images targeting candidate sedimentary, stratified outcrops to survey in this study (Figure 1).

3. Validation

We applied factor analysis and target transformation to CRISM images with known detections of hematite to test the effectiveness of our methods for identifying the characteristic broad absorptions in the visible S detector data. The CRISM type locality detection of hematite is located in Valles Marineris (Roach et al., 2010; Viviano-Beck et al., 2014). We found a good match to a laboratory hematite spectrum using target transformation (Figure 2). To test the sensitivity of our methods to the number of eigenvectors used in target transformation, we varied the number and found 10 eigenvectors were required to produce the fit shown. The technique confirms the presence of one of the previously identified broad exposures of hematite in Valles Marineris.

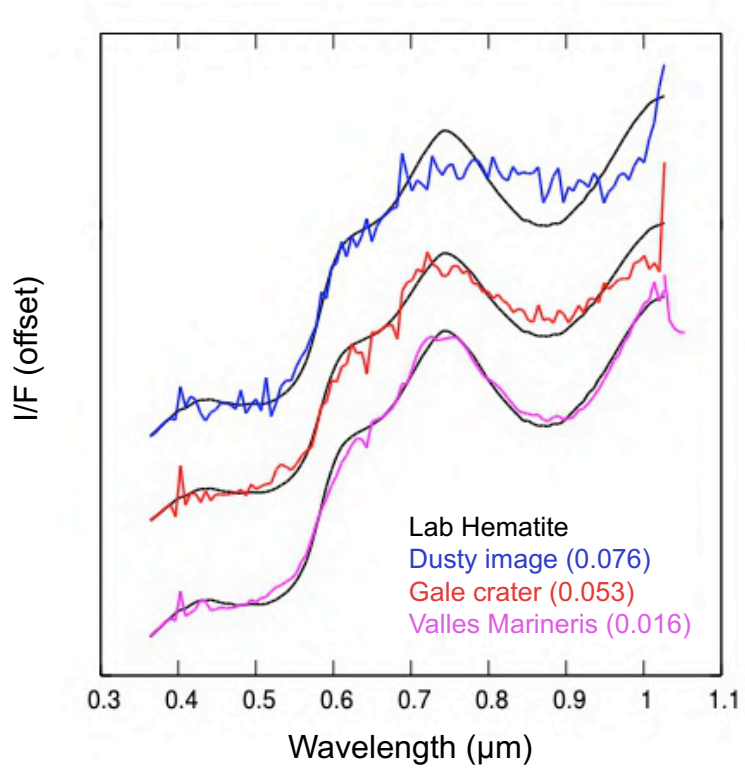

Figure 2. Target transformation modeled fits to a laboratory hematite endmember for a dusty image (FRT000069AF), an image of Gale crater's hematite ridge (FRT00021C92), and an image of Valles Marineris hematite, the type locality (FRT0000B385). SAD values are listed in parenthesis.

We also applied our methods to the previously identified exposures of hematite in Gale crater (Fraeman et al., 2013). We identified hematite, although more eigenvectors (20) are required than the previous example to produce a good fit (Figure 2). In both cases, there are some spikes, or noise, in the fit, but the characteristic absorptions, particularly the absorption at 0.86 μm is fit well. The SAD for the modeled fit to hematite in Gale does not meet our established detection threshold, indicating it may be conservative and miss small outcrops such as Vera Rubin Ridge.

Nanophase iron oxides in dust and crystalline iron oxides have similar spectral signatures. To test whether our methods were simply detecting the presence of martian dust, we applied

factor analysis to a CRISM image taken during a global dust storm. Target transformation returns a poor fit to the laboratory hematite endmember (Figure 2), indicating our technique is not sensitive to dust.

Previously, Roach et al. (2010) identified diagenetic hematite and sulfate assemblages in Valles Marineris. To test the effectiveness of our methods in comparison to previous techniques, we applied factor analysis to 65 of the images surveyed by Roach et al. (2010). Of the 40 images meeting our criteria for a good fit to hematite, only 2 were previously marked as not containing hematite. Our techniques may be more sensitive to weak spectral signatures and mixtures than the previous survey, potentially explaining the discrepancy in results for 2 images. 3 of the 25 images that did not meet our success criteria were marked by Roach et al. (2010) as containing hematite. These false negatives are likely due to differences in sampling – we apply our methods to 1 in every 3 pixels in every 3 rows, so small exposures may be missed. This can be tested by follow-up analysis measuring the size of hematite exposures in the 3 images.

4. Results

4.1 Global Distribution

For all 726 FRT and FRS CRISM images overlapping HiRISE images of candidate sedimentary, stratified outcrops (Figure 1), we quantified the goodness-of-fit to a laboratory hematite endmember spectrum using the SAD. Based on visual inspection of the target transformation fits, we chose a cutoff of SAD = 0.045. Modeled spectra with SAD < 0.045 fit the laboratory spectrum well, particularly at the 0.86 μm absorption. Of the 726 images surveyed, 19 (3%) met our fit criteria and are candidate hematite detections (Figure 1; Table 1). Below, we detail regions of interest which contain multiple candidate hematite detections. Because we find good modeled fits to hematite in multiple images within the same region, oftentimes overlapping, our detections are more confident.

Table 1. CRISM images surveyed with good modeled fits (SAD < 0.045) to laboratory hematite endmember.

Image ID	Region of Interest	Longitude	Latitude	Lab Hematite SAD
FRT0000C034	Iani Chaos	341.54	-4.03	0.0204
FRS0002FE20	Nili Fossae	72.61	20.44	0.0260
FRT0001C5D7	Iani Chaos	341.4	-4.16	0.0311
FRS00036F7A	Mawrth Vallis	339.97	23.66	0.0326
FRT00009971	Nili Fossae	74.49	22.14	0.0333
FRT00021696	Mawrth Vallis	339.93	23.4	0.0339
FRT0002105D	Mawrth Vallis	340.89	24.56	0.0347
FRS0002C8E9	Nili Fossae	72.62	20.39	0.0351
FRT0000A600	Mawrth Vallis	341.03	24.13	0.0360
FRT00021C5A	Nili Fossae	74.24	21.8	0.0362
FRT0001A3CE	Nili Fossae	72.61	20.31	0.0363
FRS000365B5	Mawrth Vallis	340.09	23.53	0.0370
FRT0001DF23	Mawrth Vallis	339.87	23.5	0.0373
FRT00017946	Meridiani Planum	358.92	3.68	0.0384
FRT0001E089	Mawrth Vallis	339.87	23.55	0.0407
FRT0002409A	Meridiani Planum	358.81	3.74	0.0420
FRS00031342	Meridiani Planum	8.31	1.73	0.0420
FRT0001903B	Mawrth Vallis	339.9	23.43	0.0424
FRT0000B710	Meridiani Planum	358.91	3.67	0.0431

4.2 Mawrth Vallis

The Mawrth Vallis region has the highest concentration of images with good target transformation identifications for hematite. In the region, 8 of the 13 CRISM images surveyed meet our detection threshold (Figure 3). Most are located in the layered floor deposits of Oyama crater. The target transformation matches confirm previous detections of iron oxides in the region. Based on analysis of index maps, hematite occurs within the Al-rich and sometimes the Fe/Mg rich phyllosilicate layers (Bishop et al., 2013; McKeown et

al., 2009; Wray et al., 2008). Modeled target transformation fits are good, particularly matching the 0.86 µm absorption center well (Figure 3).

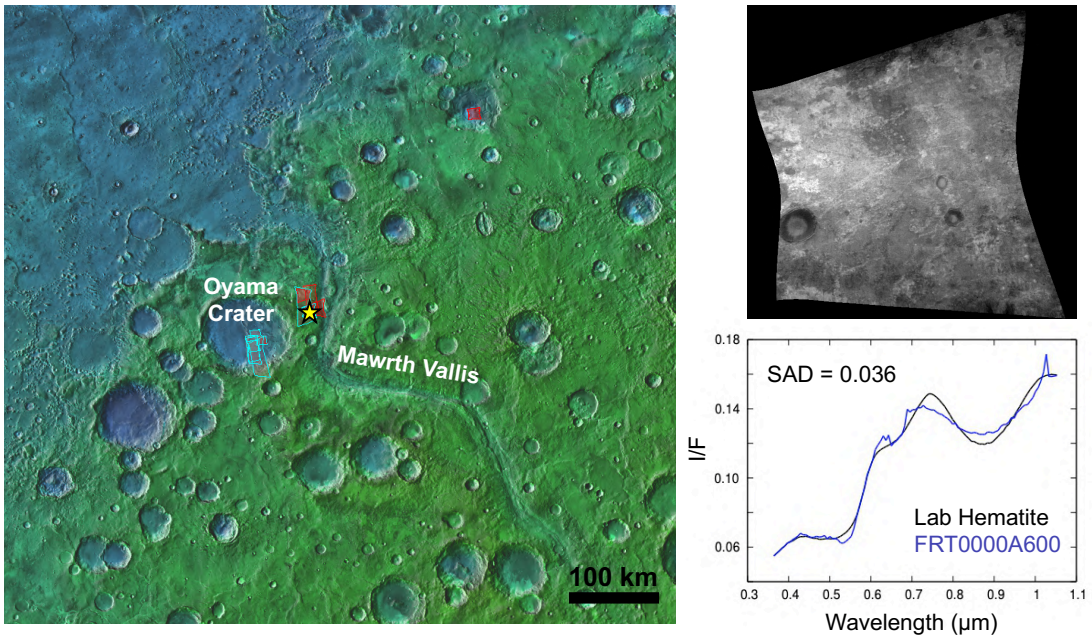

Figure 3. Mawrth Vallis region of interest with images searched shown in red and images meeting the detection threshold (SAD < 0.045) shown in blue. The base map is THEMIS Day IR with MOLA color. An example hematite target transformation fit from the region (indicated with the star) is plotted and an index map of the 0.53 µm band depth, sensitive to fine-grained crystalline hematite, is shown.

4.3 Iani Chaos and Meridiani Planum Adjacent

Many candidate sedimentary, stratified outcrops are located in and near craters surrounding Meridiani Planum, where coarse-grained (> ~5-10 µm diameter particles) gray (specular) hematite has been mapped previously using TES (Figure 4; Christensen et al., 2000). In addition, a few candidate outcrops are located in the nearby chaos terrains, particularly Iani Chaos. In comparison to the Mawrth Vallis region, few (7 out of 62) CRISM images are

identified as candidate hematite detections. The 7 potential hematite detections occur together in three locations where CRISM images overlap. Good modeled fits to hematite in overlapping CRISM images add confidence to the detection. In particular, the best hematite fits (Figure 4) globally of our survey (lowest SAD values of ~0.02) occur in the Iani Chaos region where hematite has been reported previously in a sulfate-bearing unit (Glotch and Rogers, 2007).

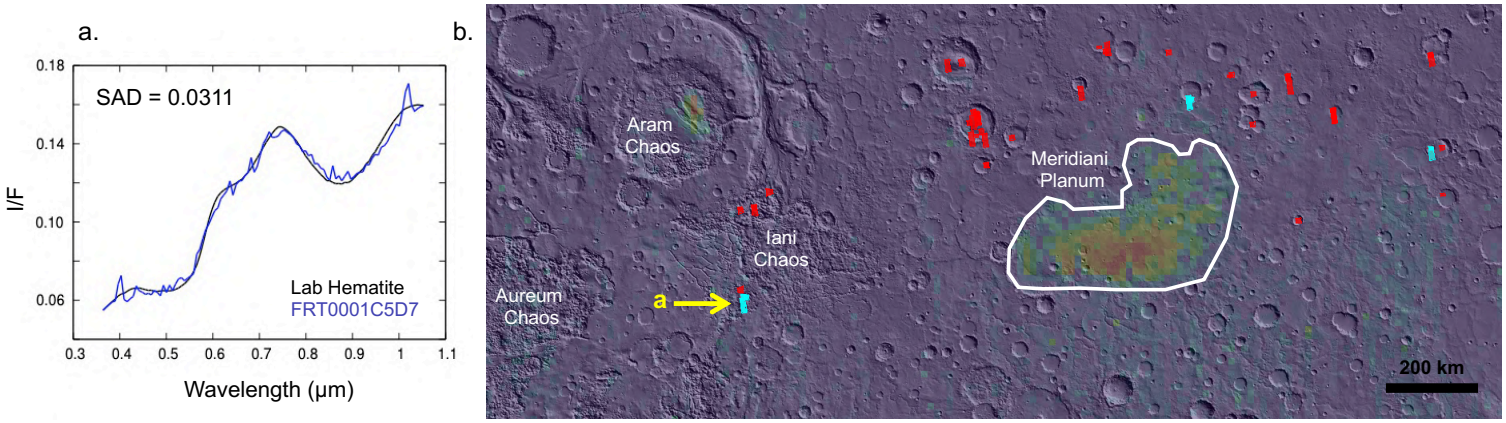

Figure 4. Iani Chaos and Meridiani Planum region of interest with images searched shown in red and images meeting the detection threshold (SAD < 0.045) shown in blue. The base map is MOLA shaded relief with TES hematite abundance (Bandfield, 2002) shown in color. The TES identified Meridiani Planum hematite is outlined. An example target transformation modeled fit to hematite from Iani Chaos is plotted.

4.4 Nili Fossae

In the Nili Fossae region (Figure 5), hematite has not been reported previously using CRISM/OMEGA or TES. We find good modeled fits to laboratory hematite in 5 of the 27 CRISM images we surveyed in the region. Hematite occurs in irregular patches in kaolinite layers above Fe/Mg-smectite layers (Figure 5; Ehlmann et al., 2009). We have confirmed our candidate hematite detections in Nili Fossae using traditional ratio methods (Figure 5).

Hematite does not occur extensively in Nili Fossae; rather it seems to be associated with regions where kaolinite has been previously identified (Ehlmann et al., 2009).

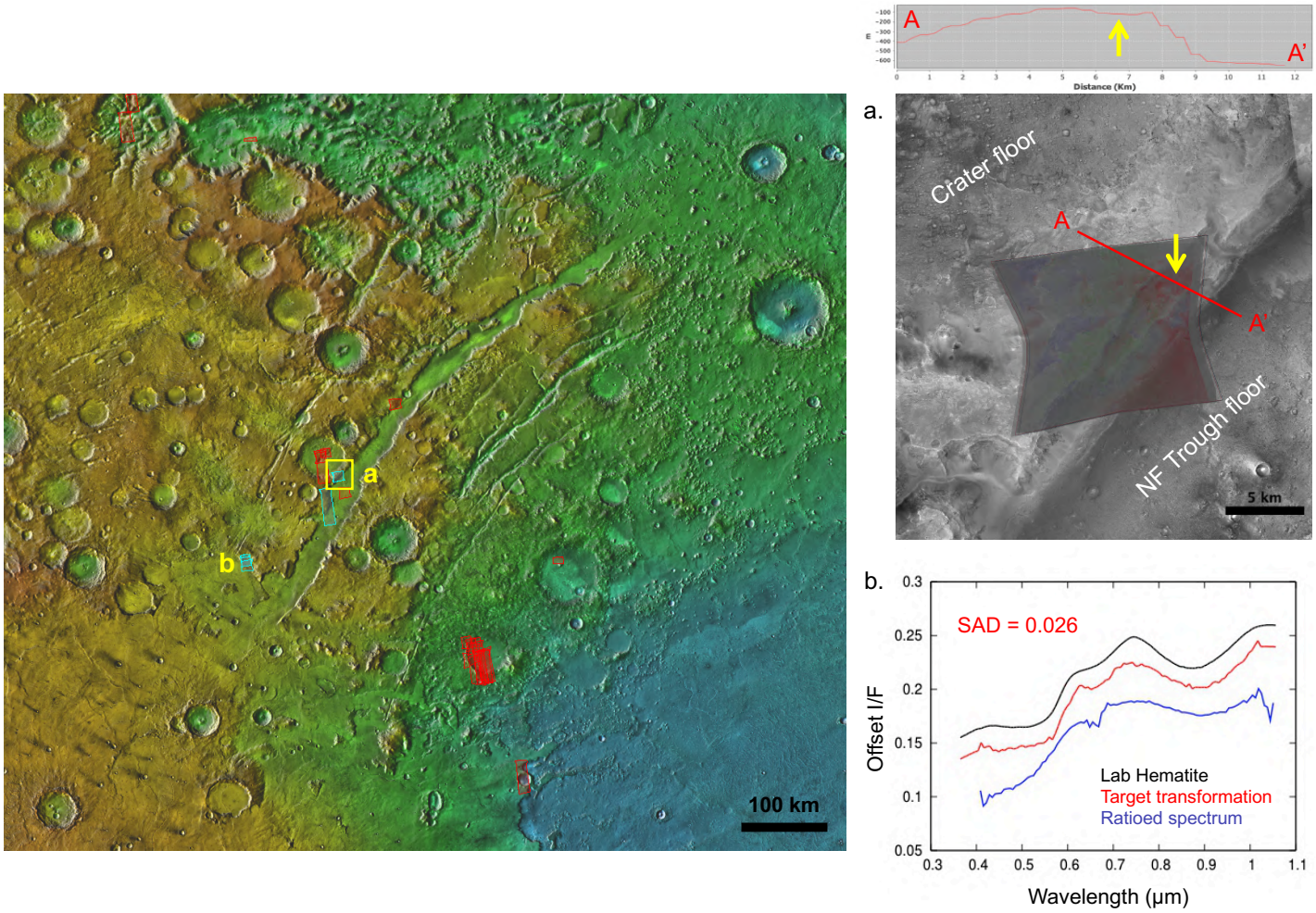

Figure 5. Nili Fossae region of interest with images searched shown in red and images meeting the detection threshold (SAD < 0.045) shown in blue. The base map is THEMIS Day IR with MOLA color. (a) Spectral index map for CRISM FRT0009971 with BD0860 in red showing hematite, BD2210 in green showing Al-rich phyllosilicates, and BD2290 in blue showing Fe/Mg phyllosilicates over CTX imagery. (b) Target transformation modeled fit to hematite for CRISM FRT0002FE20 and ratioed spectrum from the same image confirming the presence of hematite with an independent technique.

5. Discussion

5.1 Evaluation of Methods

We present the first application of factor analysis and target transformation techniques to the CRISM S dataset. The characteristic absorptions used to identify iron oxides in the visible wavelengths are broad, and were thought to be more difficult to fit using target transformation than the narrow absorptions typical of the near infrared (Thomas and Bandfield, 2017; Amador et al., 2018). We have found that the sensitivity of factor analysis and target transformation to the wavelength of the center of absorption outweighs the challenges associated with broader absorptions. Regardless of the endmember used as a "test spectrum" in target transformation, the modeled fit will have absorptions with wavelength centers true to the dataset (Amador et al., 2018). For our survey, this proved valuable for identifying hematite using the absorption centered at 860 nm, which is unique to hematite amongst the ferric oxides.

Our methods successfully confirmed the presence of hematite in locations found by previous studies using independent methods in most cases. Additionally, in Nili Fossae, where hematite was newly identified in this study, we are able to confirm the presence of hematite using traditional ratio techniques for CRISM analysis. Because we are able to identify hematite using traditional methods and map it using CRISM parameter maps, we do not face the challenge of being unable to identify the location of the phase in the CRISM image (e.g., Amador et al., 2018).

Based on our comparison to a subsample of the results of a survey of hematite in Valles Marineris (Roach et al., 2010), we find a small false negative rate (7%; 3/41) which is likely due to small exposures of hematite missed by our sampling approach of taking one in every three pixels in every three rows. This can be tested by follow-up analysis measuring the size of hematite exposures in the 3 images. Based on our comparison to Roach et al. (2010), we also find a small false positive rate (8%; 2/24). We believe that this discrepancy with previous

work may actually be due to the more quantitative rather than qualitative nature of our methods which may find deposits previously overlooked by traditional surveys.

5.2 Regions of Interest

We have identified hematite in candidate sedimentary, stratified outcrops in three regions of interest: nearby Meridiani Planum and Iani Chaos, Mawrth Vallis, and Nili Fossae. Orbital mapping using the TES instrument previously detected coarse-grained (> ~5-10 μm diameter particles) gray (specular) hematite in Meridiani Planum and Iani Chaos (Christensen et al., 2000; Glotch and Rogers, 2007). Later work using OMEGA and CRISM showed finer grained (~10 nm to ~5 μm) red hematite is also present in the chaos regions and areas around Meridiani (Bibring et al., 2007). Detailed studies of the geologic settings of the chaos regions, Meridiani, and Valles Marineris interior layered deposits led to the idea that hematite was deposited by secondary diagenetic processes associated with regional groundwater upwelling (e.g., Roach et al., 2010). In situ observations by Opportunity at Meridiani Planum provided evidence for the upwelling of near-neutral Fe^{2+}-rich, SO_4^{2-}-bearing groundwaters for which oxidation to Fe^{3+} at the surface provided excess H^+, reduced the pH, and precipitated hematite and jarosite (Squyres et al., 2004; McLennan et al., 2005; Tosca and McLennan, 2006; Hurowtiz et al., 2010). The hematite we observe in candidate sedimentary, stratified outcrops in Iani Chaos and nearby Meridiani Planum likely formed via the same groundwater upwelling mechanism.

Hematite has been previously detected using CRISM and OMEGA at Mawrth Vallis within Al-rich and sometimes the underlying Fe/Mg phyllosilicate layers (Wray et al., 2008; McKeown et al., 2009; Bishop et al., 2013). Mawrth Vallis experienced a complex aqueous history, and the hematite seen may record later diagenetic processes such as intense leaching (Greenberger et al., 2012). Hematite in terrestrial iron formations may also be the product of processes such as leaching of the Fe-rich rock. The Nili Fossae region also records a history of multiple aqueous events. In parts of the region (Figure 5), kaolinite-bearing materials are observed overlying Fe/Mg smectite-bearing materials. We observe hematite in irregular patches in kaolinite-rich layers with these outcrops, suggestive of a similar aqueous history

to Mawrth Vallis. Unlike Mawrth Vallis, hematite is not observed in the Fe/Mg phyllosilicate unit. We observe hematite in patchy deposits in the alunite-bearing layers rather than clear primary layers, so we hypothesize that the Nili Fossae hematite precipitated from weathering at or near the surface.

5.3 Global Distribution and Implications

Only 3% (19/726) of the stratified, candidate sedimentary outcrops we surveyed contain hematite. We identified hematite in three regions of interest: (1) Iani Chaos and nearby Meridiani Planum, (2) Mawrth Vallis, and (3) Nili Fossae, the only location newly reported by this work. It is difficult to distinguish emplacement mechanism from orbit. The hematite-containing outcrops identified by this survey do not correspond to sedimentary basins, and emplacement mechanisms such as groundwater upwelling and surface alteration or weathering seem more likely than direct precipitation from a water column at the surface, the sedimentary terrestrial iron formation analog. Therefore, our survey suggests the null result that analogs to iron formations either (1) did not form on early Mars, (2) remain undetectable with available data and methods, or (3) have been buried, altered, and/or destroyed. The third scenario is unlikely; hundreds of sedimentary outcrops on Mars were deposited during similar times as the terrestrial iron formations and burial and/or alteration of all of them is improbable. It is possible that analogs to terrestrial iron formations remain below our spatial resolution. At best, nominal CRISM resolution is 18 m/pixel, and a confident hematite detection using traditional methods or factor analysis and target transformation requires many (~tens) of pixels. If iron formation analogs are present only in a few thin layers of the stratified outcrop, they could be missed by the available data and methods.

If the first alternative is true, then despite the negative outcome, our survey provides a significant result refuting a previous hypothesis (Bridges et al., 2008; Burns et al., 1993; Fallacaro and Calvin, 2006; Schaefer, 1996) and implying an oxidized atmosphere on early Mars. In particular, the lack of martian iron formations, present on Earth, suggests differences in water chemistry and availability between Earth and Mars which should be explored

further. The presence of valley networks on Mars indicates atmosphere thick enough to support surficial liquid waters (Fassett and Head, 2011). The paucity of primary iron oxide sedimentary deposit could mean that other Fe-bearing phases such as Fe-phyllosilicates or Fe-sulfates were favored. Future semi-automated studies using our methods will test this theory. Additionally, we only searched for hematite in one specific geologic setting (stratified, candidate sedimentary outcrops). Future CRISM image surveys may find hematite elsewhere and help resolve outstanding questions related to iron formations on early Mars.

6. Conclusions

Terrestrial iron formations record a period when Earth's atmosphere was reducing and Fe (II) was precipitated directly out of the water column. Primary deposits of hematite, which may be oxidized analogs to terrestrial iron formations, are hypothesized to have formed on early Mars, were not observed by previous studies. We utilize the highest available resolution spectral dataset, CRISM, to systematically search stratified, candidate sedimentary outcrops for the presence of hematite. In this paper, we present the first application of factor analysis and target transformation techniques to the visible/near-infrared CRISM S detector dataset. Our methods work successfully to confirm previous detections of hematite and do not misidentify hematite where it is not present (e.g., dusty images, comparison to previous Valles Marineris survey results). We find hematite in 3% of the images searched, all within Mawrth Vallis, Meridiani Planum and Iani Chaos, and Nili Fossae. Hematite has been studied in Meridiani from orbit and in situ with Opportunity, and found to have been emplaced by upwelling groundwaters. Iani Chaos has also been previously studied and hematite in chaos terrains and Valles Marineris interior layered deposits are also thought to result from regional groundwater upwelling. In Mawrth Vallis and Nili Fossae, hematite is associated with Al-phyllosilicates overlying Fe/Mg smectites. Hematite found at both locations may have precipitated from diagenetic fluids and leaching processes.

Our survey has uncovered no obvious analogs to terrestrial iron formation in martian sedimentary, stratified outcrops. We may be missing exposures of hematite by focusing on

stratified, candidate sedimentary outcrops, so future work should map the distribution of hematite in all geologic settings globally. Our results point to differences in water availability and aqueous geochemistry between early Earth and Mars. Other phases such as Fe-sulfates and Fe-phyllosilicates may have been favored over Fe-oxides and can be searched for by future studies using factor analysis and target transformation.

References

Amador, E. S., Bandfield, J. L., & Thomas, N. H. (2018). A search for minerals associated with serpentinization across Mars using CRISM spectral data. *Icarus*, *311*, 113–134. https://doi.org/10.1016/j.icarus.2018.03.021

Bandfield, J. L., Christensen, P. R., & Smith, M. D. (2000). Spectral data set factor analysis and end-member recovery: Application to analysis of Martian atmospheric particulates. *Journal of Geophysical Research*, *105*(E4), 9573. https://doi.org/10.1029/1999JE001094

Bandfield, J. L. (2002). Spectroscopic study of the Moses Lake dune field, Washington: Determination of compositional distributions and source lithologies. *Journal of Geophysical Research*, *107*(E11), 1–15. https://doi.org/10.1029/2000JE001469

Bibring, J.-P., Arvidson, R. E., Gendrin, A., Gondet, B., Langevin, Y., Le Mouelic, S., … Sotin, C. (2007). Coupled Ferric Oxides and Sulfates on the Martian Surface. *Science*, *317*(5842), 1206–1210. https://doi.org/10.1126/science.1144174

Bishop, J. L., Loizeau, D., McKeown, N. K., Saper, L., Dyar, M. D., Des Marais, D. J., … Murchie, S. L. (2013). What the ancient phyllosilicates at Mawrth Vallis can tell us about possible habitability on early Mars. *Planetary and Space Science*, *86*, 130–149. https://doi.org/10.1016/j.pss.2013.05.006

Bridges, N. T., Hook, S. J., Thomson, B. J., Crowley, J. K., de Souza Filho, C. R., Macambira, J. B., & de Lima Pereira Silva, G. (2008). Brazilian Analog for Ancient

Marine Environments on Mars. *Eos, Transactions American Geophysical Union*, *89*(36), 329–330. https://doi.org/10.1029/2008EO360001

Burns, R. G. (1993). Rates and mechanisms of chemical weathering of ferromagnesian silicate minerals on Mars. *Geochimica et Cosmochimica Acta*, *57*(19), 4555–4574. https://doi.org/10.1016/0016-7037(93)90182-V

Catling, D. C., & Moore, J. M. (2003). The nature of coarse-grained crystalline hematite and its implications for the early environment of Mars. *Icarus*, *165*(2), 277–300. https://doi.org/10.1016/S0019-1035(03)00173-8

Christensen, P. R., Bandfield, J. L., Clark, R. N., Edgett, K. S., Hamilton, V. E., Hoefen, T., … Smith, M. D. (2000). Detection of crystalline hematite mineralization on Mars by the Thermal Emission Spectrometer: Evidence for near-surface water. *Journal of Geophysical Research: Planets*, *105*(E4), 9623–9642. https://doi.org/10.1029/1999JE001093

Christensen, P. R., Morris, R. V., Lane, M. D., Bandfield, J. L., & Malin, M. C. (2001). Global mapping of Martian hematite mineral deposits: Remnants of water-driven processes on early Mars. *Journal of Geophysical Research E: Planets*, *106*(E10), 23873–23885. https://doi.org/10.1029/2000JE001415

Ehlmann, B. L., Mustard, J. F., Swayze, G. A., Clark, R. N., Bishop, J. L., Poulet, F., … Murchie, S. L. (2009). Identification of hydrated silicate minerals on Mars using MRO-CRISM: Geologic context near Nili Fossae and implications for aqueous alteration. *Journal of Geophysical Research E: Planets*, *114*(10), 1–33. https://doi.org/10.1029/2009JE003339

Fallacaro, A., & Calvin, W. M. (2006). Spectral Properties of Lake Superior Banded Iron Formation: Application to Martian Hematite Deposits. *Astrobiology*, *6*(4), 563–580. https://doi.org/10.1089/ast.2006.6.563

Fassett, C. I., & Head, J. W. (2011). Sequence and timing of conditions on early Mars. *Icarus*, *211*(2), 1204–1214. https://doi.org/10.1016/j.icarus.2010.11.014

Fraeman, A. A., Arvidson, R. E., Catalano, J. G., Grotzinger, J. P., Morris, R. V., Murchie, S. L., … Viviano, C. E. (2013). A hematite-bearing layer in gale crater, mars: Mapping and implications for past aqueous conditions. *Geology*, *41*(10), 1103–1106. https://doi.org/10.1130/G34613.1

Fraeman, A. A., Ehlmann, B. L., Arvidson, R. E., Edwards, C. S., Grotzinger, J. P., Milliken, R. E., … Rice, M. S. (2016). The stratigraphy and evolution of lower Mount Sharp from spectral, morphological, and thermophysical orbital data sets. *Journal of Geophysical Research: Planets*, *121*(9), 1713–1736. https://doi.org/10.1002/2016JE005095

Geminale, A., Grassi, D., Altieri, F., Serventi, G., Carli, C., Carrozzo, F. G., … Frigeri, A. (2015). Removal of atmospheric features in near infrared spectra by means of principal component analysis and target transformation on Mars: I: Method. *Icarus*, *253*, 51–65. https://doi.org/10.1016/j.icarus.2015.02.012

Glotch, T. D., & Bandfield, J. L. (2006). Determination and interpretation of surface and atmospheric Miniature Thermal Emission Spectrometer spectral end-members at the Meridiani Planum landing site. *Journal of Geophysical Research E: Planets*, *111*(12), 1–12. https://doi.org/10.1029/2005JE002671

Glotch, T. D., & Christensen, P. R. (2005). Geologic and mineralogic mapping of Aram Chaos: Evidence for a water-rich history. *Journal of Geophysical Research E: Planets*, *110*(9), 1–21. https://doi.org/10.1029/2004JE002389

Glotch, T. D., & Rogers, A. D. (2007). Evidence for aqueous deposition of hematite- and sulfate-rich light-toned layered deposits in Aureum and Iani Chaos, Mars. *Journal of Geophysical Research E: Planets*, *112*(6), 1–11. https://doi.org/10.1029/2006JE002863

Glotch, T. D., & Rogers, A. D. (2013). Evidence for magma-carbonate interaction beneath Syrtis Major, Mars. *Journal of Geophysical Research E: Planets*, *118*(1), 126–137. https://doi.org/10.1029/2012JE004230

Hamilton, V. E., & Ruff, S. W. (2012). Distribution and characteristics of Adirondack-class basalt as observed by Mini-TES in Gusev crater, Mars and its possible volcanic source. *Icarus*, *218*(2), 917–949. https://doi.org/10.1016/j.icarus.2012.01.011

Hurowitz, J. A., Grotzinger, J. P., Fischer, W. W., McLennan, S. M., Milliken, R. E., Stein, N., … Wiens, R. C. (2017). Redox stratification of an ancient lake in Gale crater, Mars. *Science*, *356*(6341), eaah6849. https://doi.org/10.1126/science.aah6849

King, P. L., Lescinsky, D. T., & Nesbitt, H. W. (2004). The composition and evolution of primordial solutions on Mars, with application to other planetary bodies. *Geochimica et Cosmochimica Acta*, *68*(23), 4993–5008. https://doi.org/10.1016/j.gca.2004.05.036

King, P. L., & McSween, J. Y. (2005). Effects of H_2O, pH, and oxidation state on the stability of Fe minerals on Mars. *Journal of Geophysical Research E: Planets*, *110*(12), 1–15. https://doi.org/10.1029/2005JE002482

Malinowski, E.R., 1991. Factor Analysis in Chemistry, 2nd ed. John Wiley, New York.

McGuire, P. C., Bishop, J. L., Brown, A. J., Fraeman, A. A., Marzo, G. A., Frank Morgan, M., … Wolff, M. J. (2009). An improvement to the volcano-scan algorithm for atmospheric correction of CRISM and OMEGA spectral data. *Planetary and Space Science*, *57*(7), 809–815. https://doi.org/10.1016/j.pss.2009.03.007

McLennan, S. M., Bell, J. F., Calvin, W. M., Christensen, P. R., Clark, B. C., … Klingelhofer, G. (2005). Provenance and diagenesis of the evaporite-bearing Burns formation, Meridiani Planum, Mars. Earth and Planetary Science Letters, 240, 95-121. https://doi.org/10.1016/j.epsl.2005.09.041

McKeown, N. K., Bishop, J. L., Noe Dobrea, E. Z., Ehlmann, B. L., Parente, M., Mustard, J. F., … Silver, E. A. (2009). Characterization of phyllosilicates observed in the central Mawrth Vallis region, Mars, their potential formational processes, and implications for past climate. *Journal of Geophysical Research E: Planets, 114*(11), 1–20. https://doi.org/10.1029/2008JE003301

Murchie, S. L., Seelos, F. P., Hash, C. D., Humm, D. C., Malaret, E., McGovern, J. A., … Poulet, F. (2009). Compact Reconnaissance Imaging Spectrometer for Mars investigation and data set from the Mars Reconnaissance Orbiter's primary science phase. *Journal of Geophysical Research E: Planets*, *114*(10), 1–15. https://doi.org/10.1029/2009JE003344

Murchie, S., Arvidson, R., Bedini, P., Beisser, K., Bibring, J. P., Bishop, J., … Wolff, M. (2007). Compact Connaissance Imaging Spectrometer for Mars (CRISM) on Mars Reconnaissance Orbiter (MRO). *Journal of Geophysical Research E: Planets*, *112*(5), 1–57. https://doi.org/10.1029/2006JE002682

Rampe, E. B., Ming, D. W., Blake, D. F., Bristow, T. F., Chipera, S. J., Grotzinger, J. P., … Thompson, L. M. (2017). Mineralogy of an ancient lacustrine mudstone succession from the Murray formation, Gale crater, Mars. *Earth and Planetary Science Letters*, *471*, 172–185. https://doi.org/10.1016/j.epsl.2017.04.021

Righter, K., Yang, H., Costin, G., & Downs, R. T. (2008). Oxygen fugacity in the Martian mantle controlled by carbon: New constraints from the nakhlite MIL 03346. *Meteoritics and Planetary Science, 43*(10), 1709–1723. https://doi.org/10.1111/j.1945-5100.2008.tb00638.x

Roach, L. H., Mustard, J. F., Lane, M. D., Bishop, J. L., & Murchie, S. L. (2010). Diagenetic haematite and sulfate assemblages in Valles Marineris. *Icarus*, *207*(2), 659–674. https://doi.org/10.1016/j.icarus.2009.11.029

Schaefer, M. W. 1996. “Are there abiotically-precipitated iron-formations on Mars?” *Mineral Spectroscopy: A Tribute to Roger G. Burns*, Geochemical Society Special Publication No. 5.

Seelos, F. P., Murchie, S. L., Humm, D. C., Barnouin, O. S., Morgan, F., Taylor, H. W., … Team, C. (2011). CRISM Data Processing and Analysis Products Update — Calibration, Correction, and Visualization. *42nd Lunar and Planetary Science Conference, Held March 7-11, 2011 at The Woodlands, Texas*, 1438. https://doi.org/10.1016/0019-1035(85)90116-2

Squyres, S. W., Grotzinger, J. P., Arvidson, R. E., Bell, J. F., Calvin, W., Christensen, P. R., … Soderblom, L. A. (2004). In Situ Evidence for an Ancient Aqueous Environment at Meridiani Planum, Mars. *Science*, *306*(5702), 1709–1714. https://doi.org/10.1126/science.1104559

Stack, K. 2015. “Reconstructing Past Depositional and Diagenetic Processes through Quantitative Stratigraphic Analysis of the Martian Sedimentary Rock Record,” dissertation (Ph.D.), California Institute of Technology. doi:10.7907/Z9FN144M.

Taylor, S., and McLennan, S. 2009. “Planetary Crusts: Their Composition, Origin and Evolution,” *Cambridge University Press*, New York.

Tosca, N. J., & McLennan, S. M. (2006). Chemical divides and evaporite assemblages on Mars. *Earth and Planetary Science Letters*, *241*(1–2), 21–31. http://doi.org/10.1016/j.epsl.2005.10.021

Thomas, N. H., & Bandfield, J. L. (2017). Identification and refinement of martian surface mineralogy using factor analysis and target transformation of near-infrared spectroscopic data. *Icarus*, *291*, 124–135. https://doi.org/10.1016/j.icarus.2017.03.001

Viviano-Beck, C. E., Seelos, F. P., Murchie, S. L., Kahn, E. G., Seelos, K. D., & Morgan, M. F. (2014). Revised CRISM spectral parameters and summary products based on the currently detected mineral diversity on Mars. *Journal of Geophysical Research: Planets*, *119*(6), 1403–1431. https://doi.org/10.1002/2014JE004627.Received

Weitz, C. M., Lane, M. D., Staid, M., & Dobrea, E. N. (2008). Gray hematite distribution and formation in Ophir and Candor chasmata. *Journal of Geophysical Research E: Planets*, *113*(2), 1–30. https://doi.org/10.1029/2007JE002930

Weitz, C. M., Noe Dobrea, E. Z., Lane, M. D., & Knudson, A. T. (2012). Geologic relationships between gray hematite, sulfates, and clays in Capri Chasma. *Journal of Geophysical Research E: Planets*, *117*(7), 1–29. https://doi.org/10.1029/2012JE004092

Wiseman, S. M., Arvidson, R. E., Morgan, F., Wolff, M. J., Morris, R. V., McGuire, P. C., … Smith, M. D. (2010). Radiative Transfer Modeling of the Empirical "Volcano Scan" Atmospheric Correction: Discussion of Artifacts. *41st Lunar and Planetary Science Conference, Held March 1-5, 2010 in The Woodlands, Texas.*, 2461.

Wray, J. J., Ehlmann, B. L., Squyres, S. W., Mustard, J. F., & Kirk, R. L. (2008). Compositional stratigraphy of clay-bearing layered deposits at Mawrth Vallis, Mars. *Geophysical Research Letters*, *35*(12), n/a-n/a. https://doi.org/10.1029/2008GL034385

Chapter 6

SUMMARY, IMPLICATIONS, AND OUTSTANDING QUESTIONS

1. Methodologies for large spectral datasets

In this thesis, I developed new H LIBS analysis techniques for application to MSL ChemCam data. I also contributed to a laboratory study developing analytical methods for Cl, C, and S (Anderson et al., 2017). We measured the volatile content of powderized pellets containing mixtures of basalts and salts and hydrated minerals using LIBS and independent analysis techniques. Additionally, we studied aqueous alteration in a suite of samples from Iceland and San Carlos. Measuring H was not straightforward in the natural samples and foreshadowed future challenges with the martian ChemCam data. In particular physical matrix effects greatly impact measurement of volatile elements like H and Cl. Roughness, grain size, and sample cohesion all impact the expression of the H peak, including peak height, shape, and width. On Mars, soils contain much higher H and Cl peaks than bedrock targets, but we have shown this may not be due to large differences in sample volatile content; rather it is more likely due to the expression of the peaks in the LIBS data. The implication is that targets on Mars must be carefully sorted by physical properties (i.e., only comparing soil targets with other soil targets, etc.) before analysis. In the future, laboratory studies should measure and quantify the impact of physical matrix effects. How does target grain size impact the LIBS volatile peaks? This is an important question that can be answered in the lab. C remains a challenging element to measure with LIBS, but will be important for measuring carbonates at Jezero using Mars 2020 SuperCam. We characterized LIBS C and O peaks for normalization, and found disentangling C and O from the atmosphere and the sample to be challenging. Recent work by Schröder et al. (2019) has since worked more on this challenge, characterizing the emission properties of C and O for normalization applications, but more experiments are necessary to develop analytical methods to robustly quantify sample C and O content.

Additionally, I adapted and applied semi-automated statistical methods to search for specific minerals in the large, noisy CRISM dataset. Factor analysis and target transformation methods have previously worked well to fit narrow VNIR absorptions (Thomas and Bandfield, 2017), but it was uncertain whether the same methods would work for the broad absorptions of the visible. Our search for hematite shows these methods can be used to model broad absorptions. The CRISM S dataset is subject to less detector noise than the CRISM L dataset and is useful for mapping igneous minerals such as olivine and pyroxene as well as Fe-mineralogy such as hematite. Are any global, spectral trends present in the visible wavelengths? Can any new insight be gained from higher-resolution global mapping of igneous minerals? Future global studies enabled by factor analysis and target transformation methods may reveal new discoveries regarding the composition of Mars.

2. Gale crater's environmental history

I tested the robustness of the analytical methods developed in the laboratory by applying them to the martian ChemCam data to study H and Cl. I measured H in the Murray formation bedrock. This analysis required careful, visual inspection of every ChemCam target and observation point to eliminate points hitting soils, diagenetic features (veins, nodules, etc.), and "roughness" features (cracks, pits, etc.). Even with this screening, individual observation points with high H peaks not correlated with increases in any major or minor element are present, suggesting there is not a carrier phase and the H increase may be due to physical matrix effects. While individual ChemCam observation points may be skewed to artificially high values, the average water content of the Murray formation I measured is comparable to measurements using SAM and DAN. This result implies the "statistical" strength of ChemCam; individual point measurements are subject to high uncertainty, but ChemCam is useful for measuring bulk geochemistry. As such, we can track variability in the bulk H content of the Murray formation bedrock. H is significantly elevated in two intervals: the Sutton Island/Blunts Point transition and the top of the Jura (or the Vera Rubin Ridge) at Rock Hall. High H is correlated with elevated MgO, CaO, and FeO_T. At the Sutton Island/Blunts Point transition, there were no accompanying drill samples, so we cannot be

confident of the high-H phases present. Hydrated Mg-sulfates (Rapin et al., 2019; submitted) and hydrous Mn-oxides (Meslin et al., 2018; Kawashima et al., 1986) have been suggested as the H carriers. If these phases are primary, both imply Curiosity measured an interval characterized by increased salinity, potentially due to changes in water depth or shoreline location (Lanza et al., 2019). Bulk (target-averaged) H is anomalously high at the Rock Hall drill site. Akaganeite and jarosite are both measured by CheMin (Rampe et al., in prep) and are consistent with ChemCam measurements of elevated FeO_T and H. Here, saline fluids likely altered the bedrock.

I also applied analytic LIBS methods developed for measuring Cl to report the distribution of chloride salts at Gale crater. The scattered, isolated occurrences of chlorides are consistent with late groundwater reworking and remobilization of original deposits. The chlorides are constrained to a limited stratigraphic interval, implying increased salinity in depositional waters.

One of the motivating challenges I raised was disentangling primary from post depositional fluids to inform our understanding of past environments at Gale: as seen from our H and Cl studies, this is an ongoing challenge. Our work identifying multiple intervals of elevated H implies a rich history of water-rock interaction at Gale. We have not yet reached the sulfate-enriched unit, so a we have yet to characterize the potentially global transition from clay-enriched to sulfate-enriched units. What can we learn about the chemistry of past water(s)? What information will the transition record about past environments at Gale?

3. The fate of Fe and aqueous alteration on Mars

I have applied semi-automated statistical methods (Thomas and Bandfield, 2017) to the visible CRISM dataset to search for hematite in stratified, candidate sedimentary outcrops (Stack, 2015). Our survey returned very little evidence of hematite in these outcrops; only 3% of the images surveyed contain hematite and most occurrences are in previously mapped deposits. Our work implies that hematite has not been missed previously due to the underutilization of the CRISM visible wavelengths; rather, crystalline ferric oxides may be

rare on Mars. Where hematite occurs, it is associated with sulfates or alunite and Fe/Mg phyllosilicates. Secondary diagenetic processes associated with regional groundwater upwelling likely formed the hematite associated with sulfates at Meridiani Planum, in the Chaos terrains, and in the Valles Marineris interior layered deposits (e.g., Christensen et al., 2000; Roach et al., 2010; Hurowitz et al., 2010; McLennan et al., 2005; Tosca and McLennan, 2006). At Mawrth Vallis, hematite is dominantly associated with Al-rich and sometimes Fe/Mg-rich phyllosilicate layers (e.g., Bishop et al., 2013; Wray et al., 2008) and likely formed from intense leaching of the area. I reported a new detection of hematite in Nili Fossae. Hematite is variably expressed in outcrops containing kaolinite above Fe/Mg phyllosilicates. These assemblages resemble Mawrth Vallis and suggest a similar history of aqueous alteration. The paucity of primary iron oxide sedimentary deposits revealed by our survey could mean that other Fe-bearing phases such as Fe-phyllosilicates or Fe-sulfates were favored. Future semi-automated studies using our methods will test this theory. We searched for hematite only in candidate sedimentary, stratified outcrops (representing ~20% of the available CRISM images). In the future, a global search of all CRISM images may find hematite in other geologic settings and help resolve outstanding questions related to iron formations on early Mars.

4. Synthesis

The work presented in this thesis points to the prevalence of groundwater aqueous alteration on Mars. In Gale crater, as evidenced by the ChemCam-measured distribution of H and Cl, groundwater altered the Murray formation in multiple episodes of varying aqueous chemistries. Furthermore, deposits of hematite observed globally with CRISM were most likely emplaced by aqueous alteration events. The aqueous record of Mars remains difficult to interpret with the available datasets and due to the overprint of groundwater reworking. To decipher the evolution of Mars' climate and waters, orbital mineralogical data at even higher resolution is necessary to constrain the timing of aqueous mineral formation and its relationship to other geologic events. Additionally, detailed studies of micro-scale textures and mineralogy, provided by sample return, will better address ambiguities in the formation

of aqueous minerals and help separate primary from secondary phases. Future missions such as Mars 2020 including sample return may provide crucial fine-scale detail necessary to decipher the evolution of Mars' climate and aqueous history.

References

Anderson, D. E., Ehlmann, B. L., Forni, O., Clegg, S. M., Cousin, A., Thomas, N. H., … Wiens, R. C. (2017). Characterization of LIBS emission lines for the identification of chlorides, carbonates, and sulfates in salt/basalt mixtures for the application to MSL ChemCam data. *Journal of Geophysical Research: Planets*, *122*(4). https://doi.org/10.1002/2016JE005164

Bishop, J. L., Loizeau, D., McKeown, N. K., Saper, L., Dyar, M. D., Des Marais, D. J., … Murchie, S. L. (2013). What the ancient phyllosilicates at Mawrth Vallis can tell us about possible habitability on early Mars. *Planetary and Space Science*, *86*, 130–149. https://doi.org/10.1016/j.pss.2013.05.006

Christensen, P. R., Bandfield, J. L., Clark, R. N., Edgett, K. S., Hamilton, V. E., Hoefen, T., … Smith, M. D. (2000). Detection of crystalline hematite mineralization on Mars by the Thermal Emission Spectrometer: Evidence for near-surface water. *Journal of Geophysical Research: Planets*, *105*(E4), 9623–9642. https://doi.org/10.1029/1999JE001093

Hurowitz, J. A., Fischer, W. W., Tosca, N. J., & Milliken, R. E. (2010). Origin of acidic surface waters and the evolution of atmospheric chemistry on early Mars. *Nature Geoscience*, *3*(5), 323–326. https://doi.org/10.1038/ngeo831

Kawashima, M. (1986). Phosphate adsorption onto hydrous manganese(IV) oxide in the presence of divalent cations. *Water Research*, *20*(4), 471–475. https://doi.org/10.1016/0043-1354(86)90195-8

Lanza, N. L., Fischer, W. W., Lamm, S. N., Gasda, P. J., Meslin, P.-Y., Ollila, A. M., … Wiens, R. C. (2019). Variable Redox Conditions in Gale Crater as Indicated by Manganese Abundance Along the Curiosity Traverse. Paper presented at 50th Lunar and Planetary Science Conference, The Woodlands, TX (p. 3146).

Meslin, P.-Y., Gasda, P., L'Haridon, J., Forni, O., Lanza, N., Lamm, S., … Lasue, J. (2018). Detection of Hydrous Manganese and Iron Oxides with Variable Phosphorous and Magnesium Contents in the Lacustrine Sediments of the Murray Formation, Gale, Mars. Paper presented at 49th Lunar and Planetary Science Conference, The Woodlands, TX (p. 1447).

Rapin, W., Ehlmann, B. L., Dromart, G., Schieber, J., Thomas, N., Fischer, W. W., … Vasavada, A. (2019). High Salinity Recorded by Bedrock Sulfate Enrichments at Gale Crater. Paper presented

Roach, L. H., Mustard, J. F., Lane, M. D., Bishop, J. L., & Murchie, S. L. (2010). Diagenetic haematite and sulfate assemblages in Valles Marineris. *Icarus*, *207*(2), 659–674. https://doi.org/10.1016/j.icarus.2009.11.029

Schröder, S., Rammelkamp, K., Vogt, D. S., Gasnault, O., & Hübers, H.-W. (2019). Contribution of a martian atmosphere to laser-induced breakdown spectroscopy (LIBS) data and testing its emission characteristics for normalization applications. *Icarus*, *325*(December 2018), 1–15. https://doi.org/10.1016/j.icarus.2019.02.017

Thomas, N. H., & Bandfield, J. L. (2017). Identification and refinement of martian surface mineralogy using factor analysis and target transformation of near-infrared spectroscopic data. *Icarus*, *291*, 124–135. https://doi.org/10.1016/j.icarus.2017.03.001

Wray, J. J., Ehlmann, B. L., Squyres, S. W., Mustard, J. F., & Kirk, R. L. (2008). Compositional stratigraphy of clay-bearing layered deposits at Mawrth Vallis, Mars.

Geophysical Research Letters, 35(12), n/a-n/a.
https://doi.org/10.1029/2008GL034385